EXPERIMENTAL INVESTIGATION OF GAS-LIQUID INTERACTION IN HYDROPHOBIC NANO-ENVIRONMENT

By

Lijiang Xu

A DISSERTATION

Submitted to
Michigan State University
in partial fulfillment of the requirements
for the degree of

Civil Engineering — Doctor of Philosophy

2021

ABSTRACT

EXPERIMENTAL INVESTIGATION OF GAS-LIQUID INTERACTION IN HYDROPHOBIC NANO-ENVIRONMENT

By

Lijiang Xu

Gas and liquid interaction in hydrophobic nano-environment (GLIHNE) is ubiquitous in many natural and energy-related technologies, such as water and gas transportation in biological cells, shale gas exploitation, water management in proton exchange membrane fuel cells, and geological carbon dioxide sequestration. With the confinement effect of HNE, the gas-liquid interaction (GLI) is distinct from that in the bulk phase. However, both gas and liquid motions are difficult to be measured at the nanoscale, which has posed the primary challenge in revealing the GLIHNE experimentally.

In this dissertation, a liquid nanofoam (LN) system has been used as a platform to experimentally investigate the GLIHNE. The LN system composes of a hydrophobic nanoporous media with a non-wetting liquid phase. Due to the hydrophobic surface of the nanopores, liquid molecules cannot enter the nanopores spontaneously. With the aid of external pressure, the liquid molecules can infiltrate into the nanopores by overcoming the surface energy barrier. The GLI only has a secondary effect on the liquid infiltration behavior of the LN system. When the applied external pressure is removed, the spontaneous liquid outflow behavior of the infiltrated liquid molecules has been observed. The spontaneous liquid outflow is dominantly affected by the GLIHNE. More importantly, the nanoscale liquid outflow has been successfully quantified by the LN system performance at the macroscale. This dissertation presents the first systematic study on GLIHNE by illustrating the effects of nanopore size, ions, gas amount, and holding conditions.

First of all, it is known that the nanopore size can influence both SLI and GLI in HNE. However, the nanoporous material has a pore size distribution. By developing a consecutive-step compression mode, the pore size distribution has been subdivided into several narrow segments. It has been proven that the nanopore size is negatively correlated with the degree of liquid outflow and GLI is enhanced in smaller nanopores. Secondly, to better understand the GLIHNE, it is necessary to decouple GLI from SLI in the HNE. To this end, a set of LN systems have been specifically designed to have the same liquid infiltration behavior, i.e. the same SLI in the HNE. While the unloading process of these LN systems, the degree of liquid outflow varies, which is dominated by the ion effect on the GLIHNE. Results show that both cations and anions have a more profound effect on gas solubility in nano-confined liquid than that in the bulk liquid phase due to the gas oversolubility effect. In addition, the effect of anions is more pronounced than cations on GLIHNE, which breaks down the conventional theory in the bulk phase. Thirdly, a different amount of additional gas phase has been introduced into one particular LN system consisting of the same liquid-solid composition. A remarkable difference in the degree of liquid outflow has been observed, indicating the GLIHNE is highly sensitive to the amount of gas phase. As the gas amount increases, the degree of liquid outflow from hydrophobic nanochannels is considerably promoted. This is due to the bulk liquid being saturated by the additional gas and the earlier termination of the gas outflow process from the HNE. Lastly, the gas diffusion in the liquid phase confined in HNE has been studied by holding an LN system at different pressure levels for various time durations. It has been demonstrated that the gas diffusion progress exhibits an exponentially decaying rate. In addition, distinct from the bulk case, pressure poses a pronounced effect on the GLIHNE.

To my parents and grandparents, who always believe in me.

ACKNOWLEDGEMENTS

I would like to express my gratitude to a number of people, without their support this dissertation would not be possible to complete.

First and foremost, I would like to express my deepest gratitude and appreciation to my advisor, Dr. Weiyi Lu, for his guidance and support throughout the past five years. His enthusiasm for revealing the underlying science and optimism has inspired and encouraged me to overcome all the obstacles I have encountered in my research. I am deeply indebted for the training and resources he provided and his efforts in refining my manuscripts and presentations. I am truly grateful to have such a great advisor in pursuing my PhD degree.

I am also extremely grateful to my committee members Dr. Scott Calabrese Barton, Dr. Nizar Lajnef, and Dr. Volodymyr Tarabara for their generosity in providing experimental facilities and training, and constructive advice provided for this research.

I also would like to extend my sincere thanks to my colleagues and friends, Dr. Mingzhe Li, Mr. Alex Mirabal, Dr. Yuanchao Liu, Dr. Charifa Hejase, Ms. Cynthia Collings for providing detailed training and guidance. Special thanks to Dr. Mingzhe Li for all his critical instructions on experimental training and patient help through my PhD study. Besides, I also would like to thank the help and companion from my colleagues and friends, Chi Zhan, Fuming Yang, Bang He, Junfeng Li, Jun Guo, Mingmin Wang, Yifan Men, Wu Zhou, Ningyu Sha, Ruixue Li, Pan Wu, Yifeng Tian, Yang Chen, Xuyang Li, Xunhao Wang, Rundong Zhao, and Yian Chi.

Special thanks to the financial support from Michigan State University (start-up funds), and National Science Foundation (CBET-1803695). I am also grateful for the fellowships and

travel funds provided by the Department of Civil and Environmental Engineering, the College of Engineering and the Graduate School at Michigan State University.

Last but not least, I would like to thank my parents and grandparents for their caring, encouragement, and overwhelming support. To my parents, Mu Xu and Jinghui Jiang, and my grandparents, Zhiheng Xu, Sijun Dong, Fuxiang Jiang, Yong Yang, and my uncle and aunt, Sihua Luo and Wei Xu, thank you for your love, support and always believe in me. I would like to dedicate this dissertation to all of you.

TABLE OF CONTENTS

LIST OF TABLES

LIST OF FIGURES

Chapter 1. INTRODUCTION

1.1 Significance

With the growing demand for energy worldwide, the traditional fossil fuels (petroleum, natural gas, and coal) are being depleted and have caused many environmental problems, such as global warming, ozone layer depletion, biosphere and geosphere destruction, and ecological devastation[1–4]. It is significant to secure the future energy supply and reduce the global carbon footprints. Some strategies that are either currently undertaken or can potentially contribute to solving the energy issue in the future include (i) gradually replacing the traditional fossil fuels by unconventional shale gas[5,6] and sustainable alternative resources, such as proton exchange membrane (PEM) fuel cells using hydrogen[7,8] and (ii) reducing greenhouse gases by carbon dioxide sequestration[9,10]. Optimization of these technologies requires understanding of gas-liquid interaction in hydrophobic nano-environment (GLIHNE). For example, the specifically designed hydrophobic nanoporous gas diffusion layer (GDL) has been adopted to solve the water management issue caused by excessive water blocking the reaction sites on the catalyst layer[11,12] in the PEM fuel cell [13,14] as shown in Figure 1.1. In order to enhance proton conductivity of PEM, the gas and water transportation in the nanoporous GDL needs to be well controlled to maintain free movement of oxygen molecules while driving away excessive water at certain hydration level[15]. Therefore, at the hydrophobic nanoporous GDL, the GLI is an essential mechanism needed to be understood for better water management.

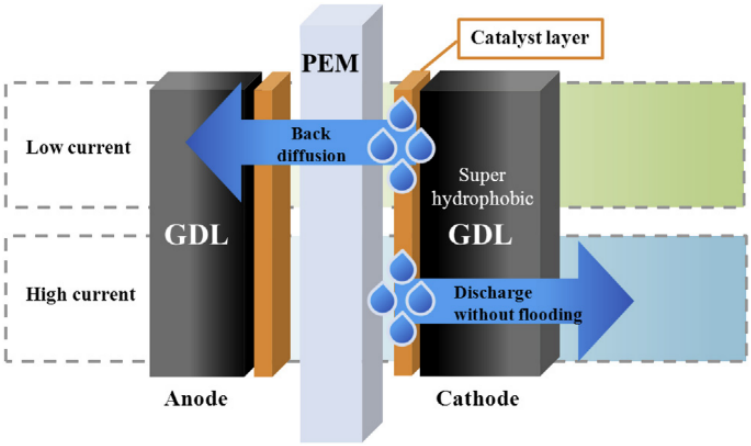

Figure 1.1. Water management in PEM fuel cell[14].

Besides, the GLIHNE plays an important role in the growing industry, shale gas formation and exploitation. The shale gas is stored mostly in nanometer-sized shale matrix in different forms, including compressed gas, adsorbed surface gas, and gas dissolved in the pore water during kerogen maturation[16] , as shown in Figure 1.2. A mechanistic understanding of gas-liquid interaction (GLI) in shale gas nanopores is essential in designing effective operational processes and development of shale reservoirs.

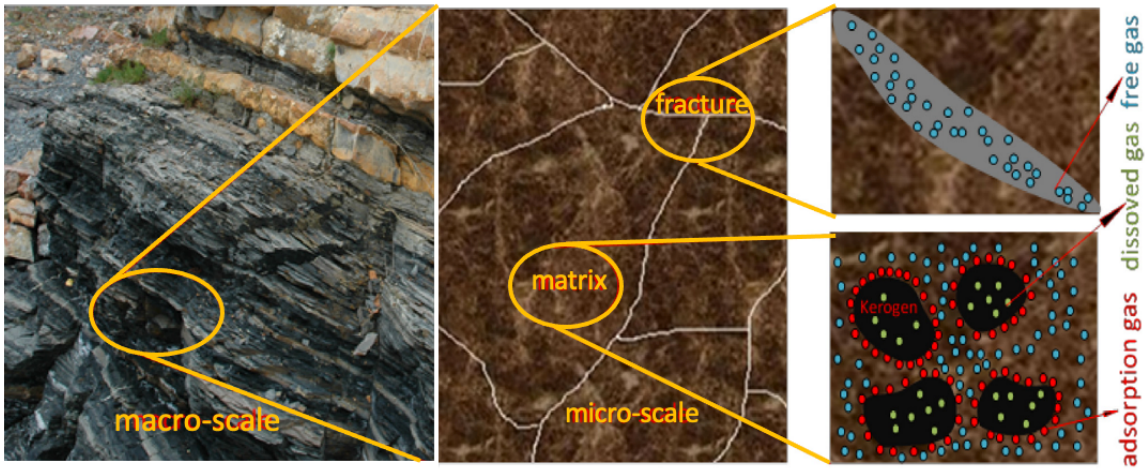

Figure 1.2. Shale gas reservoir[17].

Also, for the shale gas exploitation shown in Figure 1.3, the gas is released from the shale matrix and migrates to nearby fractures in the pressurized fracturing liquid and ultimately

reaches to a production well bore[18]. This movement of shale gas molecules in the liquid is directly related with the efficiency of shale gas production, therefore, the GLIHNE needs to be studied.

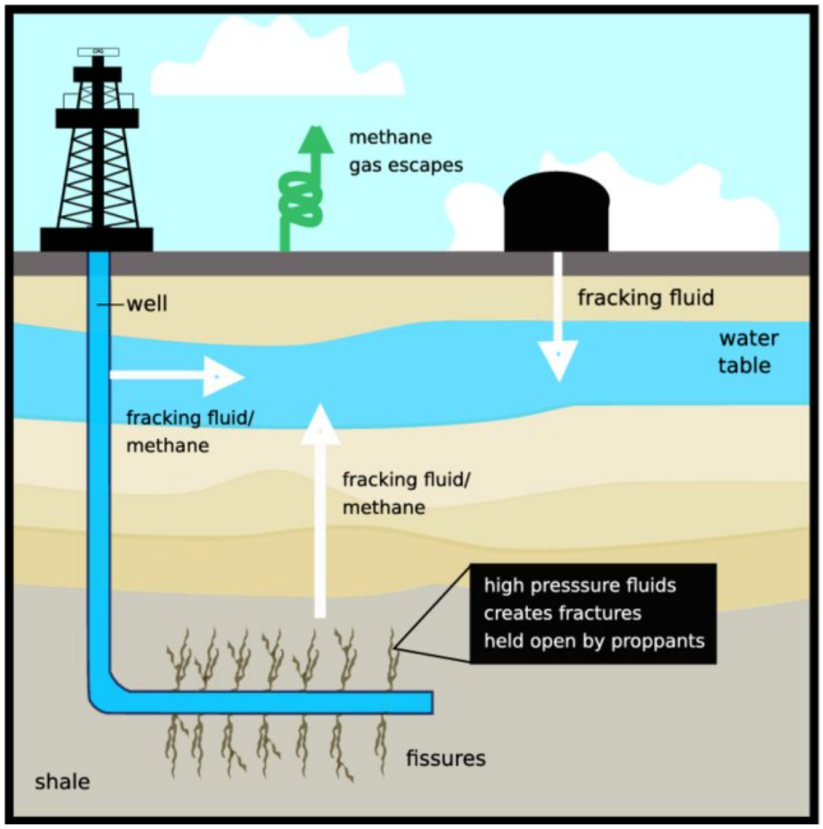

Figure 1.3. Hydrofracturing[19].

In addition, during the development of hydraulic fracturing, the strikingly high gas solubility in hydrophobic nano-environment (HNE) has been found[16]. The excessive green-house gases can be dissolved into the liquid filled nano-environment, such as naturally occurring clay minerals[20], depleted shale and tight formations[21–24], shown as Figure 1.4. This phenomenon has become a promising approach in carbon sequestration in tackling the growing greenhouse gases, which is a main cause of the global warming.

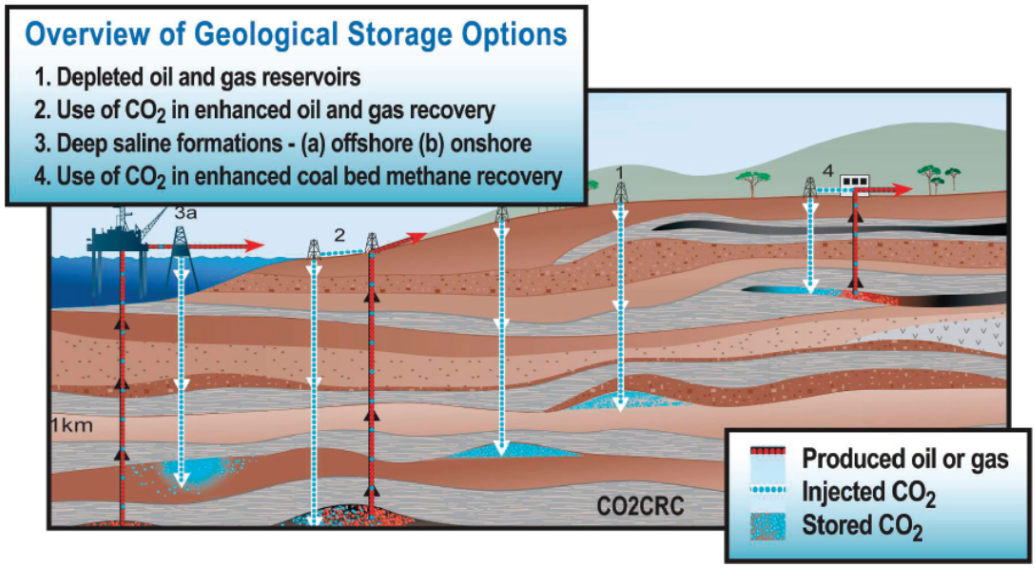

Figure 1.4. Geological carbon sequestration[25].

By exploring the GLIHNE, our understanding on liquid and gas flow behavior in hydrophobic nano-environment has been extended, which guides and inspires the development of novel nanotechnologies to tackle the growing threat of pollution, global warming, and energy crises nowadays.

1.2 Motivation

In bulk liquid, the influence of GLI on liquid properties are always treated as secondary due to low gas solubility[26]. As shown in Figure 1.5, the dissolved gas molecules are restrained by the densely packed liquid molecules[27,28], which change little with pressure[29,30]. Therefore, pressure effect is ignored in dissolved gas diffusion models[29,31–33], such as Wilke-Change equation[34].

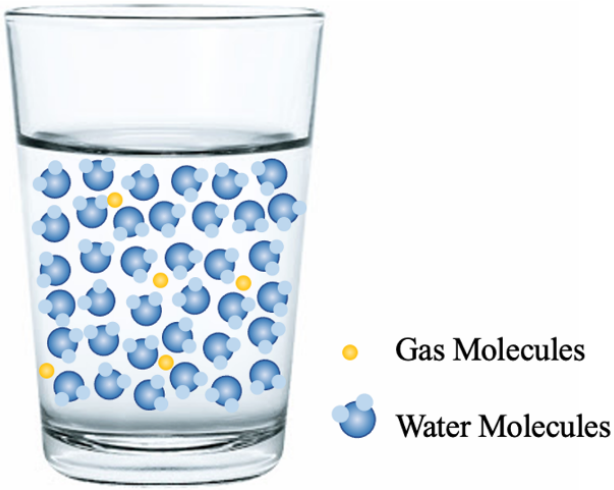

Figure 1.5. Schematic of gas dissolving in densely packed water molecules in bulk phase.

Moreover, the overall properties of dissolved gas and liquid is determined mainly by liquid molecules itself, such as liquid density[32] and gas diffusivity[34]. In addition, the gas solubility can be reduced by electrolytes due to "salting-out effect"[35,36] and elevated temperature due to promoted gas nucleation energy[37].

However, the influences of different electrolytes, pressure, temperature, gas species, and nanopore size on GLIHNE can be different than what is observed in the macroscopic levels. Based on previous studies, it has been demonstrated that in nano-environment, conventional theories are no longer valid[38–42]. For instance, in hydrophobic nano-confinement, the gas solubility in nanoconfined-liquid is much higher than that in bulk liquid, which is defined as the gas oversolubility[43,44]. This has been observed in various gas-liquid combinations, including CO_2, N_2, H_2, or CH_4 dissolved in water, n-hexane, or ethanol confined in nanoporous environment[43–48]. The oversolubility of N_2 and CO_2 in nano-confined water has been found to exceed the bulk value by a factor of 30 and 15, respectively[44,46]. Since the nanoconfinement prevents a regular 3D ordering of water molecules, the density of water has been reduced to 60 to 80% in nano-environmnet[49–51], such as CMK-3 carbon[52], Silicalite-1[53], LTAa, Faujasitea nanopores[54]. Li et al. have found that CO_2 density elevated significantly near the hydrophobic

nanopore walls by increasing pressure, leading to a pressure facilitated CO_2 diffusivity[45]. As the gas and liquid motions are unique in the hydrophobic nano-environment, a systematic investigation on GLIHNE is desired.

1.3 Scientific Gaps

Although the studies shown above shed light on the GLIHNE, there is no systematic studies on GLIHNE by illustrating several necessary influences, such as nanopore size, ions, gas amount, and holding time and pressure. For example, there are limited molecular dynamic simulations focused on the influence of pressure on GLIHNE, due to its secondary effect on liquid density and gas diffusion in bulk liquid[29,32,55]. However, most processes involving GLIHNE are carried underground with typical geological pressure (5 ~ 40Mpa) [56–58], such as shale gas exploitation and carbon dioxide sequestration in aquifers. At such a high pressure, due to the nano-confinement, liquid and gas flow behavior and interaction cannot be simply interpreted by the mechanisms occurring at low pressure, such as heterogeneous catalysis and gas separation[59–62]. Therefore, an experimental investigation of GLIHNE under different pressures is critical for evaluating the hydraulic fracture parameters in shale gas reservoirs and designing carbon sequestration processes. Besides, the other parameters that widely exists in natural HNE ought to be considered, such as ions and gas amount in the system, since they can pose a different effect on the surface tension and gas solubility of the liquid in HNE than that in their bulk counterpart.

Currently, most of the studies shown above are conducted by molecular dynamic simulations, while the experimental investigation on GLIHNE are still lacking. The difficulties in revealing the GLIHNE has been summarized. Firstly, it is challenging to produce the material with nanoscale features[63], while itself can be easily handled at a much larger scale. Secondly,

measuring the gas liquid motions at the nanoscale is difficult. Last but not least, the solid-liquid interaction (SLI) is always coupled with the GLI in HNE, which poses the main challenge in revealing the GLIHNE experimentally. To be specific, by modifying a single system parameter, both the SLI and GLI are changed[64,65]. Therefore, most of the previous studies have not identified and individually analyzed the GLIHNE. The experimental setup has to satisfy these requirements to reveal the GLIHNE.

1.4 Methodology

By considering the difficulties in studying GLIHNE experimentally, a recently developed liquid nanofoam (LN) system has attracted our attention. The LN system is composed of a hydrophobic nanoporous media and a non-wetting liquid phase. At ambient pressure, the liquid molecules cannot enter nanopores due to surface energy at the nanopore entrance. When an external pressure is applied and overcomes the surface energy barrier between the hydrophobic surface of the nanopores and the non-wetting liquid, the liquid molecules are compressed into and fill the hydrophobic nano-channels. Through this pressure-induced liquid infiltration process, a large amount of external energy is converted into solid-liquid interfacial tension and dissipated as heat. This liquid infiltration process is a novel energy mitigation mechanism with extremely high efficiency (~100 J/g), nearly 2 orders of magnitude higher than traditional materials[66,67].

At nanoscale, during the pressure induced liquid infiltration, the gas molecules initially sealed in nanopores are gradually dissolved by the infiltrated liquid molecules. When the external pressure is removed subsequently, both the liquid and gas molecules flow out from the nanochannels. During this liquid infiltration and outflow cycles, the nanoporous framework is damage free as the energy dissipation mechanism of the LN system is based on the pressure-induced liquid infiltration into the nano-channels rather than permanent crushing or plastic

buckling of the nano-channels[68]. In such a system, the nanoscale GLI is interpreted by the macroscale liquid outflow behavior which can be precisely measured. Therefore, the LN system is a potential platform to experimentally investigate the GLIHNE.

In the LN systems, the size of nano-channels, the ion species in the liquid phase, gas amount in the nano-channels and the bulk liquid phase, and other parameters can be manipulated separately to reveal their effects on the unique GLIHNE.

1.5 Objectives

The focus of this research is to understand the GLIHNE by using the LN system and the thesis is organized as follows. In chapter 3, the nanopore size effect on the degree of liquid outflow of the LN system as well as the GLIHNE has been investigated. In chapter 4, the ion effect on gas oversolubility in HNE has been revealed by decoupling the SLI from the GLI in HNE. In chapter 5, the effect of gas amount on the liquid outflow has been studied by varying the gas amount in both the nano- and bulk- environments. In chapter 6, the gas diffusion behavior from the nano- to bulk- phase has been thoroughly studied by holding the LN systems at different peak pressures for certain durations. In chapter 7, the preliminary results of gas species and temperature effect on GLIHNE has been introduced as future study.

Chapter 2. BACKGROUND

2.1 Hydrophobic Surface Treatment of Nanoporous Particles

The nanoporous media used in the LN systems is nanoporous silica gels. In nature, these silica-based nanoporous particles have hydrophilic nanopore surfaces. When these hydrophilic particles are mixed with water, these nanopores are soaked up with the liquid molecules immediately. Consequently, the LN system is nearly incompressible, as shown in Figure 2.1.

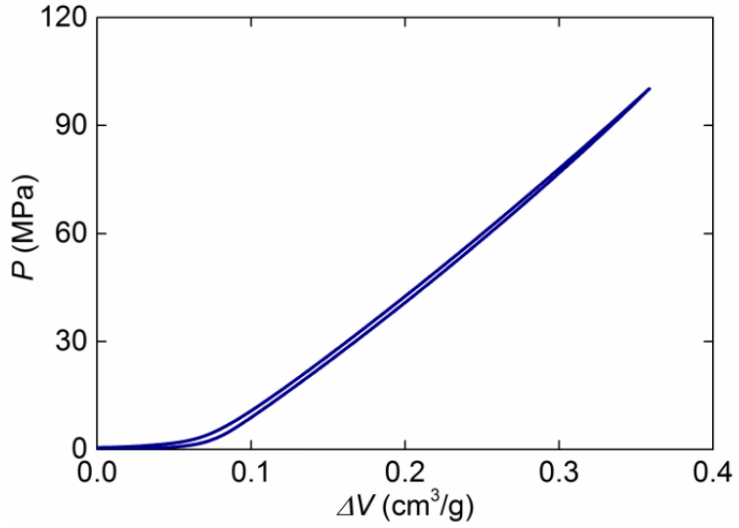

Figure 2.1. Typical compressive behavior of the mixture of hydrophilic nanoporous particles and a wettable liquid phase.

To increase the surface hydrophobicity, surface treatment is applied to graft an alkyl layer onto the nanopore surface[69]. The detailed surface treatment procedure is described as follows. About 0.5 g of raw silica nanoporous particles is firstly vacuum dried at 100 °C for 2 h to remove moisture. Then, the particles are immediately immersed in 40 mL dry toluene, which is stirred at 90°C for 3 hours for well mixing. After cooling to room temperature, 10 mL of surface reagent and 1 mL of pyridine as catalyst are added into the mixture, which is stirred and refluxed

at 95 °C in a heating mantle for 5 hours. During the surface treatment, alkyl groups are attached to hydroxyl sites on the nanopore surfaces as shown in equation (2.1). The surface treated nanoporous particles are washed with dry ethanol and dried in vacuum at 50 °C for two days.

$$SiO_2 - OH + R - Si(CH_3)(CH_3)Cl \longrightarrow SiO_2 - O - Si(CH_3)(CH_3) + HCl \quad (2.1)$$

After the surface treatment process, the surface properties of the nanopore wall are dominated by the alkyl group and converted from hydrophilic to hydrophobic, as shown in Figure 2.2. The anchored alkyl layers on the nanopore wall reduce the effective nanopore size. Commonly used surface treatment reagents and their effective layer thicknesses are listed in Table 2.1.

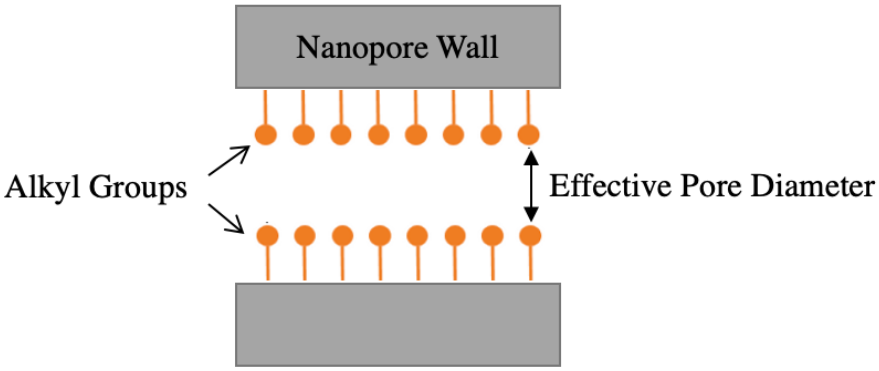

Figure 2.2. Schematic of the surface modifications.

Table 2.1. Surface groups and the bonded layer thickness.

Surface group	Chemical formula	Effective layer thickness (nm)[70,71]
Chloro-trimethyl-silane (C_1)	CH_3- $Si(CH_3)_2Cl$	0.3
Chloro-triethyl-silane (C_4)	CH_3-$(CH_2)_3$-$Si(CH_3)_2Cl$	0.5
Chloro-dimethyl-octyl-silane (C_8)	CH_3-$(CH_2)_7$-$Si(CH_3)_2Cl$	0.8

2.2 Liquid Infiltration

In order to apply the external pressure on the LN system, the nanoporous material and liquid are sealed inside a stainless-steel cell by two cylindrical pistons equipped with O-rings, as shown in Figure 2.3.

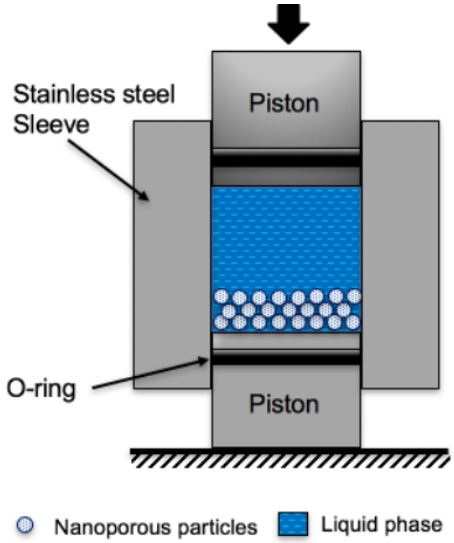

Figure 2.3. Schematic of LN specimen sealed in a testing cell with two pistons.

As an external force, F, is applied on the cell with a constant speed, a hydrostatic pressure, P, is built in the testing cell and applied on the sealed LN specimen. The externally applied hydrostatic pressure is calculated as $P = 4F/\pi d^2$, where d is the diameter of the pistons. The specific volume change of the LN system is calculated as $V = \delta \cdot \pi d^2/4m$, where δ and m are the measured displacement of the piston and the mass of the nanoporous silica gel, respectively. During the loading process, the initial response is linear elastic, as shown in Figure 2.4.. As the externally applied hydrostatic pressure is high enough to overcome the surface energy barrier between the hydrophobic nanopore surface and the non-wetting liquid, liquid molecules are forced into and fill the nanopores. The pressure-induced liquid filling process and the resulting pressure plateau are referred to as liquid infiltration and the liquid infiltration plateau,

respectively. The pressure of the first turning point of the loading curve is defined as the liquid infiltration pressure, P_{in}, which is determined by the effective excessive solid-liquid interfacial tension, $\Delta\gamma$. As described by the classic Laplace-Young equation $P_{in} = \Delta\gamma / d_n$, where d_n is the effective nanopore diameter[72].

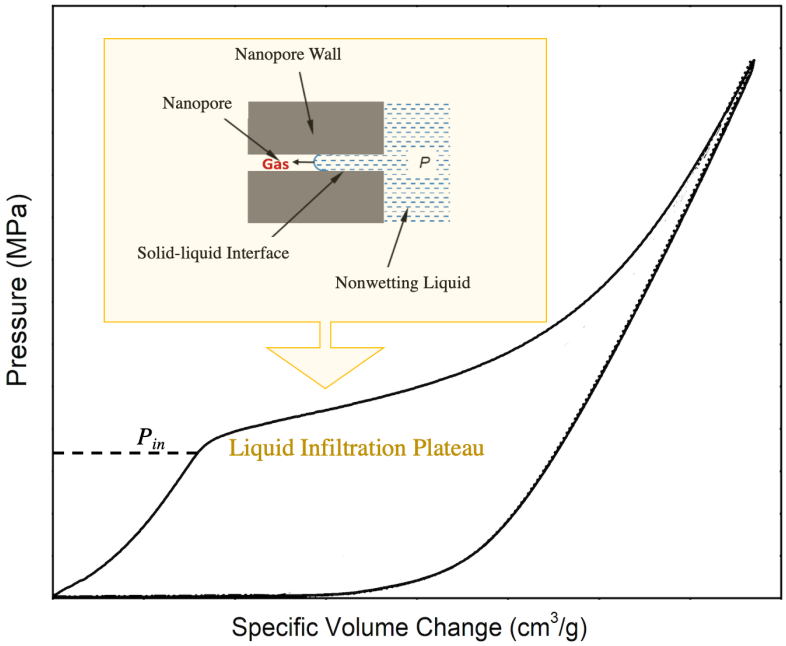

Figure 2.4. Pressure-induced liquid flow in LN system.

Upon the completion of nano-channel filling, the slope of the loading curves quickly increases to a value that is slightly higher than the initial elastic one. As the nano-channels are filled with liquid, the nanoporous silica gel is turned into its solid counterpart, which has larger Young's and bulk moduli.

2.3 Spontaneous Liquid Outflow

Upon unloading, as shown in Figure 2.4, the internal pressure of the LN specimens drops linearly with small volume change in the beginning. The initial unloading slope is slightly higher than the initial infiltration slope, due to a lower water solid ratio outside of nanopores. When the pressure drops below P_{in}, the unloading slope reduces gradually indicating the volume change is enlarging. The initial slight increment suggests that the majority of liquid molecules are still

sealed inside nanopores due to water incompressibility. And it can be attributed to the gas nucleation from its dissolved state in nanopores. Then, the much-reduced slope of the unloading curve as well as the associated large specific system volume change is observed. It indicates that the confined liquid and gas molecules start to flow out from the hydrophobic nanopores. And the system returns to a length close to its original length. This spontaneous liquid outflow is dominantly affected by the GLIHNE. More importantly, the nanoscale liquid outflow has been successfully quantified by the LN system performance at macroscale.

2.4 Degree of Liquid Outflow

Although the liquid outflow cannot be directly observed in the unloading portion of the first cycle due to the outflow of mixed liquid and gas from the nano-channels, the degree of liquid outflow can be determined by the liquid infiltration plateau of the second cycle. Figure 2.5. shows a general three consecutive loading-unloading curves of a LN specimen. By comparing the first two loading-unloading cycles, P_{in} increases while the width of the infiltration plateau is much reduced in the 2nd cycle. This indicates that the volume of nanopores is partially available for liquid infiltration in the 2nd cycle, which is the volume of nanopores that liquid flows out of during the unloading process of the 1st cycle. The width of the infiltration plateau of each cycle is defined as the specific volume change between the loading and unloading curves at the infiltration pressure, as illustrated in Figure 2.5. As both the loading and unloading curves of 2nd and 3rd cycles of the LN specimen are nearly identical, only the width of the infiltration plateau of 1st and 2nd cycles, W_1 and W_2, are labeled. The degree of liquid outflow equals to the reusability of the LN specimens and is defined as $D_{out} = W_2/W_1$.

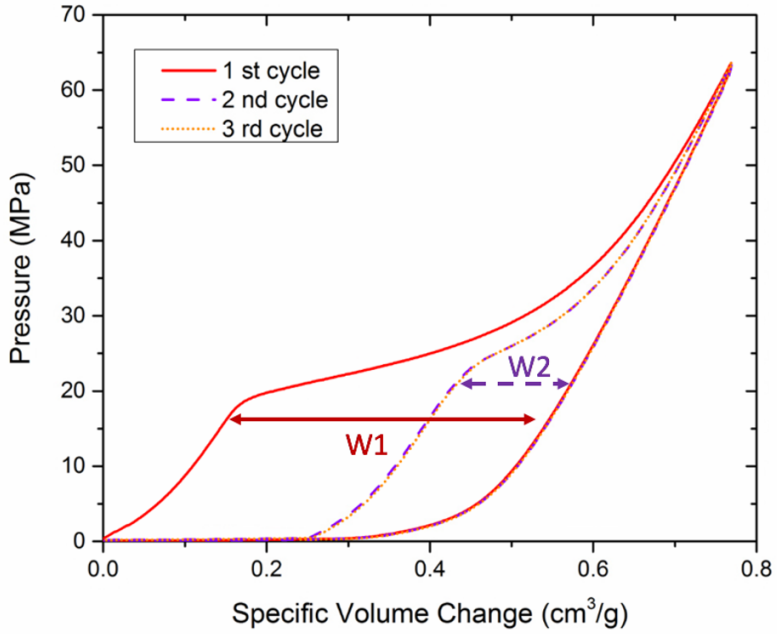

Figure 2.5. Three loading-unloading cycles of the LN system.

2.5 Solid-liquid Interaction (SLI) in Hydrophobic Nano-environment

The loading-unloading cycles for the LN system with the same nanoporous material is shown in Figure 2.6. The degree of liquid outflow is enhanced by adding LiCl electrolyte into deionized water. In the meantime, the infiltration pressure is also improved. According to classic Laplace-Young equation[72], with the same nanopore diameter, the infiltration pressure is proportional to the excessive solid-liquid interfacial tension. Since the excessive solid-liquid interfacial tension can represent the solid liquid interaction in a hydrophobic nano-environment (SLIHNE), the infiltration pressure (P_{in}) can work as an indication of the intensity of SLI in LN system with the same nanoporous material. Therefore, the degree of liquid outflow is promoted by the enhanced SLIHNE, which was focused on by most previous studies on nanofluidic motions[53,54]. However, in these MD simulations, the gas phase effect on liquid outflow has been ignored by placing liquid molecules in vacuum nanotubes or nanochannels. Other experimental work based on a single nanoporous media[64,65] shed light on the effect of ion effect on the liquid outflow. However, the ion concentration in the electrolyte solutions has an influence on both the

excessive solid-liquid interfacial tension and the gas solubility in HNE. Specifically, the degree of outflow can be changed by many factors, such as the nanoporous network[26,75], the excessive solid-liquid interfacial tension[64,65], as well as the gas oversolubility[30,31,33] . Therefore, the challenge in revealing the effect of GLI on the degree of liquid outflow lies in the difficulty to decouple the effect of SLIHNE.

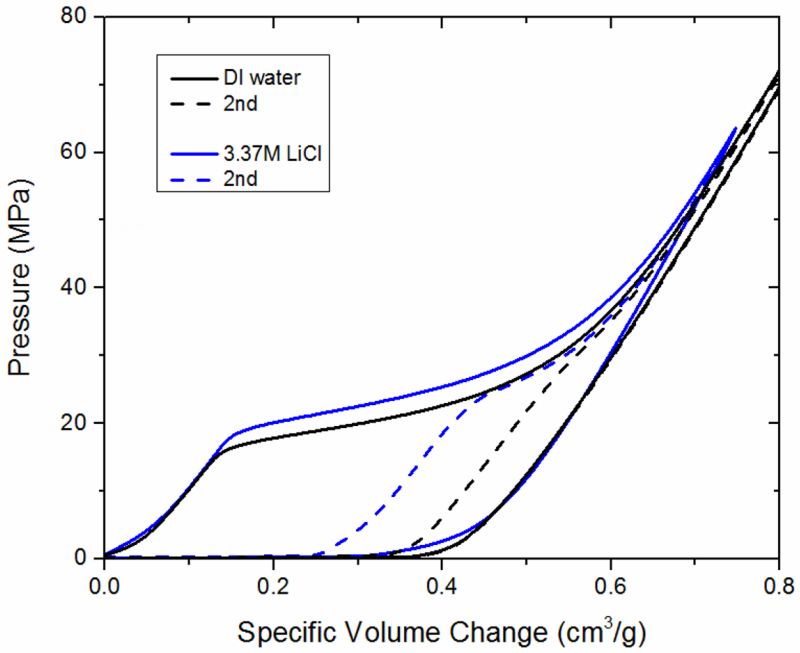

Figure 2.6. The effect of SLI on degree of liquid outflow.

2.6 Gas Oversolubility in HNE

The solubility of gas in bulk liquid phase can be described by Henry's Law, which establishes a linear relationship between the concentration of dissolved gas and its partial pressure above the liquid phase. However, in HNE, considerable accumulation of gas molecules has been observed near the hydrophobic pore surfaces, where water depletion occurs[45,46]. This significantly increased gas solubility in HNE has been regarded as the oversolubility phenomenon and the enhanced factor is referred as the oversolubility factor by comparing with its bulk gas solubility. This oversolubility phenomenon is dependent on the gas, solvent, and

solid nanoporous framework (absorbent). Based on previous studies, there are three atomic mechanisms that the oversolubility is stem from[77]. 1) adsorption-driven phenomenon which arises from the strong interactions between gas and solid framework; 2) for weak gas-solid interactions, confinement-induced gas uptake is favored in the regions of low liquid density, near the hydrophobic pore walls; 3) for partially saturated pores, adsorption at the gas-liquid interface contributes to oversolubility. In LN systems, nanopores are saturated by the infiltrated liquid, therefore, oversolubility can be attributed to the mechanisms 1 and 2. By comparing the gas solubility in nanopores to that in bulk liquid, the oversolublity factor can be determined. Studies has shown that the oversolubility factor is enhanced more with the least soluble gas N_2, while less with the most soluble gas CO_2 in zeolites (ZSM-5), porous silica (MCM-41), and MOF (MIL-100)[44]. The oversolubility of N_2 and CO_2 in nano-confined water has been found to exceed the bulk value by a factor of 30 and 15, respectively[33]. This phenomenon has been observed in various gas-liquid combinations, including H_2, or CH_4 dissolved in water, n-hexane, or ethanol confined in different HNE[43–48].

Chapter 3. NANOPORE SIZE EFFECT ON GLIHNE

3.1 Introduction

Understanding liquid motion in nano-environment is of great significance for a wide range of applications, including drug delivery, molecular transportation, catalysis, sensing, energy absorption, and many others[78–82]. Recently, a liquid nanofoam (LN) system, which employs the liquid flow in nanopores as its energy absorption mechanism, has received increasing attention[83–88]. In an LN system composed of liquid and a hydrophobic silica gel, the liquid can be driven into the nanopores when an applied external load is sufficiently high, leading to the absorption of tremendous amount of energy. Upon removal of the external load, the liquid may or may not flow out from the nanopores. Although the mechanistic determinants for the liquid outflow process remain poorly understood, it is clear that the liquid outflow contributes to the energy absorption properties of the LN system. Sun et al. converted an elastic spring like LN system into an energy absorber with high efficiency by suppressing the liquid outflow[89].

It has been demonstrated in previous studies that the liquid outflow behavior in the nano-environment is sensitive to the quality of surface treatment[90,91], pore geometry[92,93], species and concentration of electrolyte[64], relaxation time[94,95], degree of liquid degassing[96], and temperature[97]. In addition to these factors, Borman et al. have found that the transition of a liquid from nonwetting to wetting in porous structures is related to the degree of filling, i.e., the infiltration depth, using percolation and fluctuation theories[98–102]. For instance, as the infiltration depth reaches a critical value of 0.9, the recoverability of the system at 279 K becomes zero, i.e. no liquid outflow occurs[98]. In current work, we have further hypothesized that the critical infiltration depth is a function of nanopore size. To test this hypothesis, we have examined the

liquid outflow behavior in nanopores using a nanoporous silica gel with a wide pore size distribution. Our results show that the critical infiltration depth increases as the nanopore size becomes smaller.

3.2 Material and Experimental Setup

The nanoporous material used in current study was a hydrophobic precipitated silica (Perform-O-Sil 668, Nottingham Corp.). The as-received material was in powder form, with the average particle size around 4 μm. Due to the low strength of the porous frame (lower than the required activation pressure for mercury porosimetry analysis method) and the relatively large nanopores (>100 nm, the upper limit of gas adsorption analysis method), mercury porosimetry and BET methods were not applicable for analyzing the porous structure of this nanoporous silica. Instead, water porosimetry[70,103,104] was used to characterize the porous structure. The specific nanopore volume of the nanoporous silica was measured to be 1.8 cm^3/g. The porosity was then calculated as 80% based on the measured specific nanopore volume and the density of solid silica.

In Figure 3.1., a cylindrical testing cell and two poly(methyl methacrylate) pistons were designed to investigate the nanoscale liquid motion of the LN. The cross-sectional area of the pistons, A_p, was 286 mm^2.The pistons were equipped with O-rings to seal the LN sample which contained 0.3 g of the nanoporous silica gel and 2 g of liquid. The nanoporous silica gel was pre-compressed into a close packed disk to minimize the air trapped in between the particles. The liquid phase used in current study were DI water, 23 wt% lithium chloride (LiCl) aqueous solution, and 46 wt% LiCl aqueous solution.

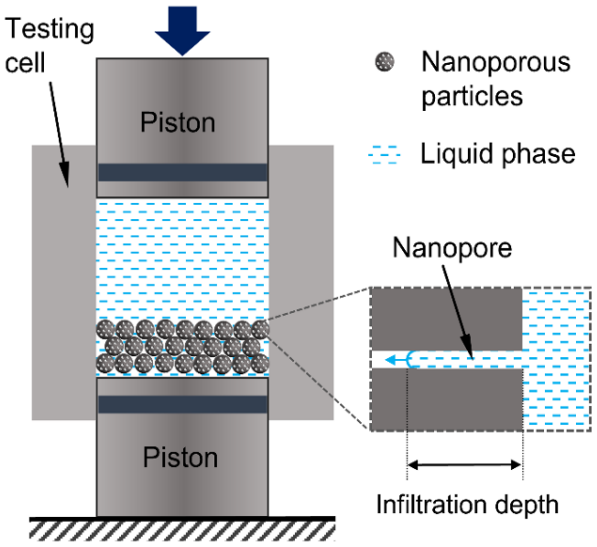

Figure 3.1. Schematic of the experimental setup.

The LN samples were compressed by an Instron 5982 universal tester equipped with environmental chamber (Instron, Inc.) at 20 °C, 50 °C and 80 °C. High vacuum grease was applied on the O-rings to reduce the friction between O-rings and pistons. No liquid leakage was observed during all compression tests. The applied pressure was calculated as $P=4F/\pi d^2$, where F is the force exerted on the piston and d is the diameter of the pistons. For the single-step test, the applied force increased gradually to 2 kN, which was equivalent to an applied pressure of 7 MPa, at a constant loading rate of 2 mm/min, after which the crosshead of the Instron machine was moved back at the same speed. The loading-unloading process was repeated for five cycles. For the consecutive-step test, an LN sample with identical solid and liquid content was compressed at six consecutive steps at the same loading rate. The peak pressure of each step was increased monotonically from 1.25 MPa to 7 MPa. To study the liquid outflow behavior of each step, the LN sample was compressed for three cycles in each step. The specific volume change of the LN sample was defined as $\Delta V= \delta \cdot \pi d^2/4m$, where δ and m are the piston displacement and the mass of the nanoporous silica gel, respectively.

3.3 Results

In the single-step test, the applied force increased gradually at a constant loading speed of 2 mm/min. When the pressure reached 7 MPa, the crosshead of the Instron machine was moved back at the same rate. The results of the single-step test are shown in Figure 3.2. As all the subsequent cycles are nearly identical to the second one, only the first two loading-unloading curves are shown here for clarity. For water based-LN, a non-linear pressure-volume change is observed in the first loading cycle (Figure 3.2a). Microscopically, pressure-induced liquid molecules flow into the nanopores starts at 1.0 MPa associated with the specific volume change in the LN of 0.9 cm^3/g and ends up at the point of 3.0 MPa and 2.7 cm^3/g. This process is referred to as liquid infiltration and identified as the stress plateau of the loading curve[83,86]. For self-comparison purpose, the starting point of the infiltration plateau is defined as the point at which the slope of the loading curve is reduced by 50% of that of the initial elastic region and the ending point is defined as the point at which the slope increases by 50% of that of the infiltration plateau. The infiltration pressure (P_{in}) of the LN is the critical pressure forcing the liquid molecules into the nanopores, which is a function of the nanopore size based on the classic Laplace-Young equation[105]. The infiltration volume (V_{in}) of the LN, which is determined by the width of the infiltration plateau, is around 1.8 cm^3/g. In the single-step test, this value is the same as the total pore volume of the nanoporous silica gel characterized by the water porosimetry method. In the second loading cycle, the curve is no longer hysteretic indicating nearly zero liquid outflow takes place in the unloading process of the first cycle. The energy absorption behavior of the LN is similar to the plastic behavior of regular foams which is permanent. As the liquid phase changes to 23 wt% LiCl aqueous solution, the initial P_{in} increases to 1.5 MPa due to the increased effective surface tension of the liquid phase[106]. More importantly, the reusability of

LN increases to approximately 25%, i.e. 25% liquid molecules flow out from the nanopore during the unloading process of the first cycle. The reusability is further promoted to 80% when the concentration of LiCl solution increases to 46 wt%.

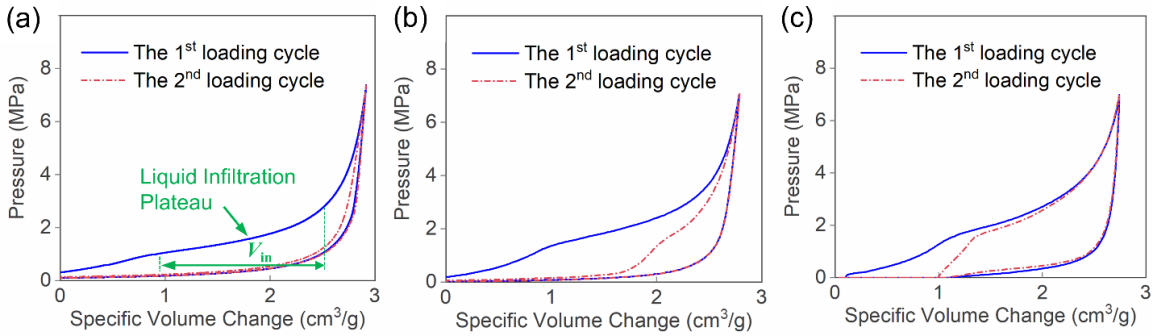

Figure 3.2. Typical sorption isotherm curves of single-step test at 20 °C. Liquid phase (a) water (b), 23 wt% LiCl aqueous solution, and (c) 46 wt% LiCl aqueous solution.

3.4 Discussion

The considerably different liquid outflow behavior in Figure 3.2 is likely to result from the gas-liquid interaction in the nanopores[107]. For water based-LN, as the external loading reaches P_{in} and increases, the liquid gradually enters the nanopores, leading to an increasing infiltration depth (inset in Figure 3.1). The normalized infiltration depth D is defined as $D=V_l/V_p$, where V_l and V_p are the volume of intruded liquid molecules and total available pore volume of the nanoporous material, respectively. As D increases, the gas phase in the nanopores is compressed and stores more potential energy. Consequently, the effective gas solubility in the confined liquid molecules is significantly enhanced[108]. Note that due to the entrapment, the gas solubility in nano-environment is distinct from that in bulk phase[46]. Once a critical value D^* is reached, the effective gas solubility in the confined liquid molecules is sufficiently high and the gas can diffuse into the bulk liquid phase. After removal of the external loading, the gas phase, which can act as the driving force for liquid outflow, is absent[109]. Thus, no liquid outflow can be observed as the liquid-solid interfacial tension is not sufficient. As the LiCl concentration

increases, the gas solubility is remarkably reduced[110,111]. Therefore, for LiCl solution based-LN samples, the gas phase is highly compressed and stores higher potential energy in the nanopores in the infiltration process. During unloading, the stored potential energy in the gas phase is released. Combining with the solid-liquid interfacial tension, the driving force is high enough to promote the liquid outflow. The gas outflow is validated by the air bubbles generated in the bulk liquid phase after the single-step compressive tests (Figure 3.4). Before the test, the nanoporous silica particles are a close-packed layer with no visible air bubbles (Figure 3.4a). For water based-LN, the volume of the silica gel layer expands dramatically during the unloading process, with large amount of visible air bubbles in the testing cell (Figure 3.4b). The air, initially trapped in the nanopores, diffuses out of nanopores and the nanopore volume is occupied by infiltrated liquid molecules. In this single-step compression test, as all the nanopores are completely filled by the liquid molecules, the D^* is reached. For LN with 23 wt% LiCl aqueous solution, the volume expansion of the silica gel layer after the first loading cycle is smaller than that of water based-LN, indicating that less gas phase diffuses out of the nanopores. The non-diffused gas phase performs as the driving force for liquid outflow. Thus, the LN sample shows 25% reusability. For LN with 46 wt% LiCl aqueous solution, the volume of silica gel layer almost remains the same after the completion of the first loading cycle, which indicates most of the gas phase stays in the nanopores. As a result, nearly 80% of liquid molecules outflow from the nanopores.

Single-step compression test on degassed LN samples further validates that the gas phase in the nanopores acts as the dominating driving force during the liquid outflow process. The degassed LN sample was prepared by placing the mixture in vacuum (4 kPa) for 24 h. Thus, the gas phase was partially removed by the degassing pretreatment. More specifically, both the gas

dissolved in liquid and small bubbles in the mixture were almost entirely eliminated, while the gas in nanopores was only partially removed[96]. Upon compression, the remaining gas phase in the nanopores was more prone to dissolve in the liquid and the driving force for liquid outflow was much reduced compared with undegassed LN. As a result, the infiltration width of the second loading cycle of 46 wt% LiCl aqueous solution based-LN showed that the extent of liquid outflow was remarkably reduced from 80% (Figure 3.2c) to 15% (Figure. 3.3c). For water and 26 wt% LiCl aqueous solution based-LN, the extent of liquid outflow became nearly zero (Figure. 3.3a and 3.3b).

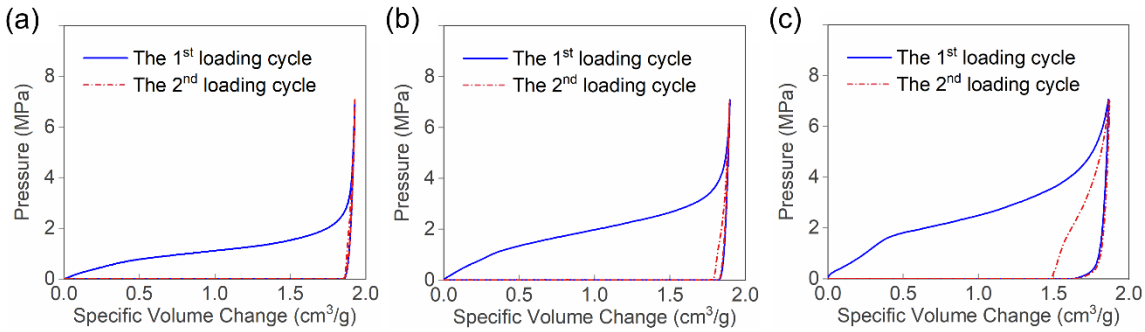

Figure 3.3. Typical sorption isotherm curves of the single-step test on degassed LN at 20 °C. Liquid phase: (a) water, (b) 23 wt% LiCl aqueous solution, and (c) 46 wt% LiCl aqueous solution.

These results confirm that the gas phase is the primary driving force for the liquid outflow. Please also note the pressure level of the plateau in the unloading curve (~0.1 MPa) in Fig. 3.3c is much lower than that (~0.8 MPa) in Fig. 3.2c, indicating that part of the driving force for liquid outflow, i.e. the gas phase, is lost. These results are contradictory to the literature results[96], in which the liquid outflow is promoted by degassing. This is attributed to the remarkably different pore size in these two LN systems. In the ZSM-5 zeolite based-LN[96], the pore size is ~2 nm and the liquid outflow path can be easily blocked by the excessive gas phase. Therefore, by removing the excessive gas, the liquid outflow path would become continuous,

which benefits liquid outflow. Besides, due to the ultra-small pore size, the interfacial force (~18 MPa), which is governed by classic Laplace-Young equation, is high enough to drive the liquid out and the gaseous driving force can be neglected. While in current system, the pore size is 1 or 2 orders of magnitude larger and the gas blocking effect can be ignored. In addition, the interfacial force (~2 MPa) is not sufficient for liquid outflow and the gaseous driving force becomes dominant. Consequently, degassing leads to a lower liquid outflow extent in current LN system.

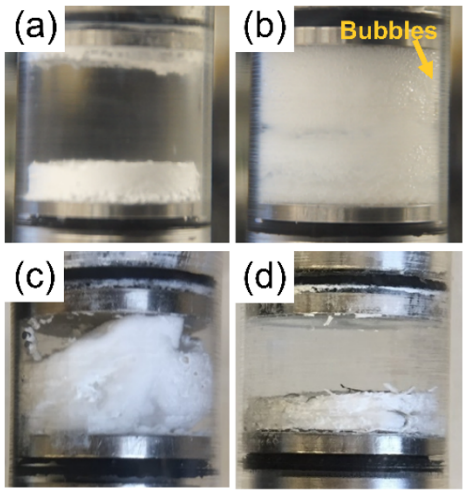

Figure 3.4. (a-d) Snapshots of the LN sample (a) before single-step test (b-d) after single-step test. Liquid phase: (b) water, (c) 23 wt% LiCl aqueous solution, and (d) 46 wt% LiCl aqueous solution.

To study the effect of nanopore size on D^*, we have characterized the nanoporous structure of the silica gel by the water porosimetry method. Following the classic Laplace-Young equation, $r = 2\gamma/P_{in}$ (where γ is the excessive solid-liquid interfacial tension with value of 72.8 mN/m[70] and r is the effective nanopore radius), the pressure-volume change curve is converted into nanopore size distribution by the water porosimetry analysis. The nanopores of the silica gel used in current study exhibit a wide diameter distribution from 40nm to 400nm (Figure 3.5a). The pore size distribution characterized by water porosimetry is further verified

from the SEM photos of the silica gel as shown in Figure 3.5b. Combining the pore size distribution and the consecutive loading mode, we reveal the effect of nanopore size on *D**.

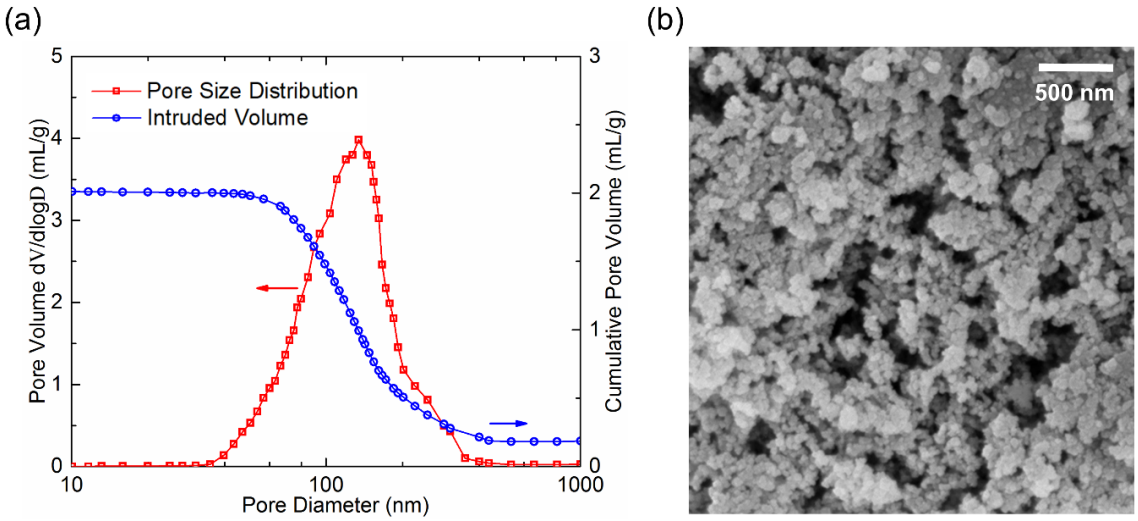

Figure 3.5. (a) Pore size distribution of silica gel and intruded volume vs. pore size curve. (b) Typical SEM image of the nanoporous silica.

In the consecutive-step test, the LN was compressed at six consecutive steps at a constant loading rate of 2 mm/min. The peak pressure of each step was increased monotonically from 1.25 MPa to 7 MPa. Thus, the widely distributed nanopores are divided into six segments with different average nanopore sizes by controlling the applied peak pressure. The combination of all the test curves matches well with the loading-unloading curve of the single-step test (Figure 3.6), indicating all the nanopores in the silica gel are involved in the stepwise tests. More importantly, for water based-LN, all the sorption isotherm curves of the six steps show partial repeatability of the liquid infiltration process as indicated by the overlapped areas between steps (Figure 3.6a), which is not shown in the single-step test (Figure 3.2a). The repeatable hysteretic behavior demonstrates that the energy absorption mechanism of LN is associated with the liquid motion in nanopores rather than the plastic deformation such as the buckling of the nanopore walls which is irreversible. The repeatable liquid infiltration process also indicates that part of the liquid

molecules outflow from the nanopores when the external pressure is removed. In other words, by controlling the peak pressure, the D^* is not reached in each step. Similarly, the reusability of LN is promoted in the consecutive-step test for LN with LiCl aqueous solution (Figure 3.6b and 3.6c), indicating that more liquid molecules flow out from the nanopores in the consecutive-step test than in single-step test.

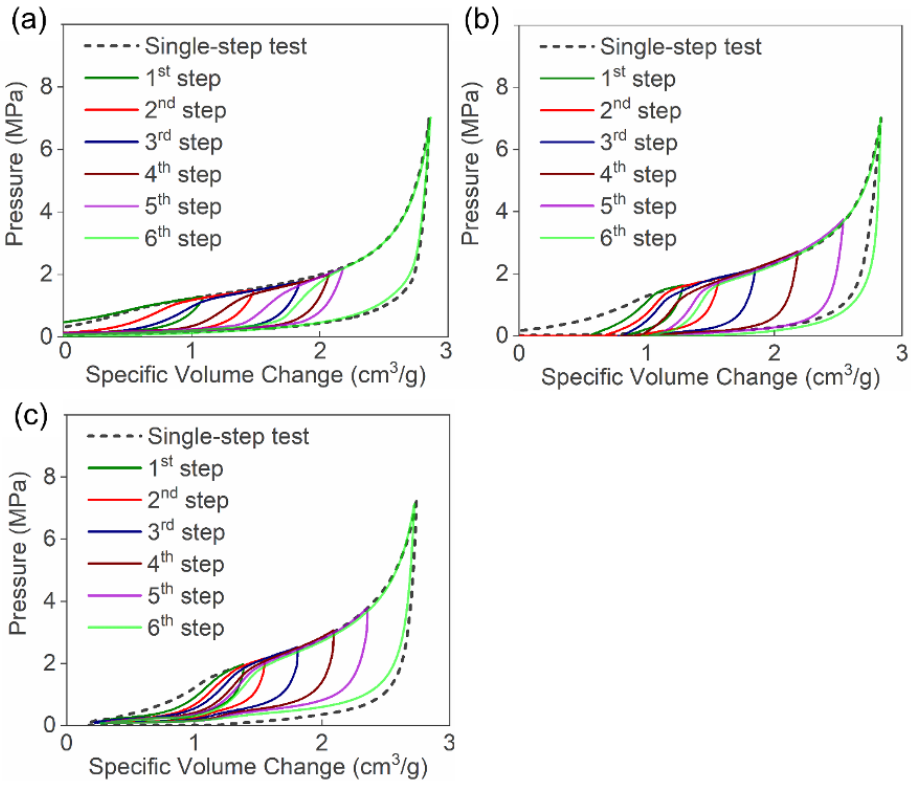

Figure 3.6. (a-c) Typical sorption isotherm curves of the consecutive-step test at 20 °C. Liquid phase: (a) water, (b) 23 wt% LiCl aqueous solution, and (c) 46 wt% LiCl aqueous solution.

To better understand the effect of nanopore size on D^*, the loading cycle is repeated for three times for each step (Figure 3.7). The loading cycles are referred to as $L_{i,j}$, where i is the step number and j is the cycle number in each step.

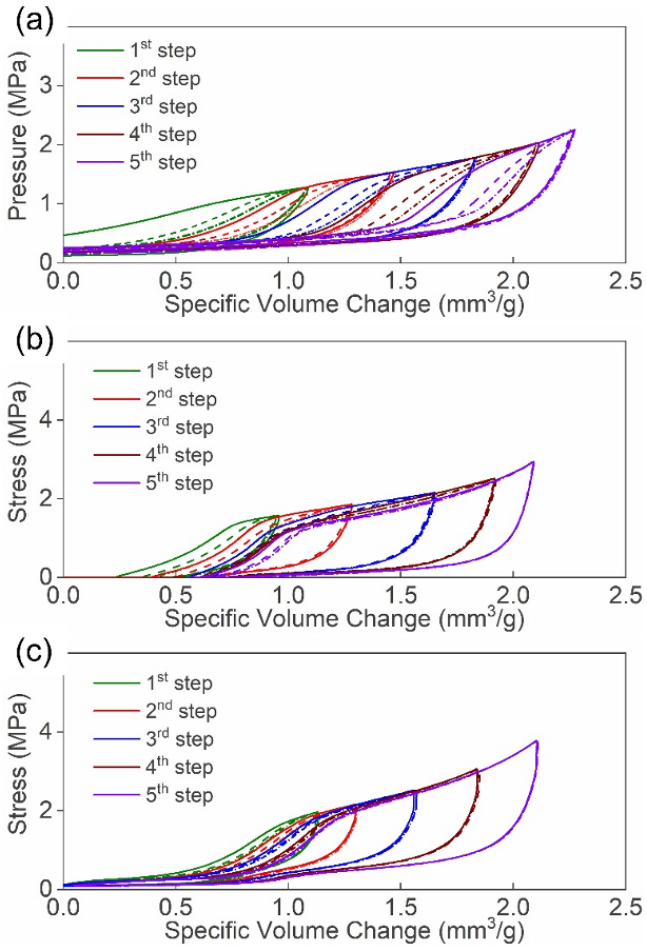

Figure 3.7. The results of the consecutive-step cyclic test (1st to 5th steps) at 20 °C. Liquid phase: (a) water, (b) 23 wt% LiCl aqueous solution, and (c) 46 wt% LiCl aqueous solution.

The normalized critical infiltration depth (D^*) can be determined from the recoverability (R) after the first loading cycle in each step and summarized in Table 3.1. During the outflow process in each step, only the portion with infiltration depth smaller than D^* can flow out of the nanopores. Both D^* and R are defined by the volume ratio. Thus, for each loading step, the normalized critical infiltration depth equals to recoverability of the first loading cycle, $D^*=R_{i,1}$. R can be determined from the consecutive-step cyclic test. As shown in Figure 3.8, $P_{max,i}$ is the peak pressure of the i^{th} step. In each step, only nanopores with P_{in} in between $P_{max,i-1}$ and $P_{max,i}$ are considered. The average infiltration pressure for the i^{th} step, $P_{in,i} = (P_{max,i-1} + P_{max,i})/2$. The value of $P_{max,0}$ is the initial infiltration pressure of the LN measured in the single-step test (Figure

3.2). The average nanopore size (r_i) is calculated by using the average infiltration pressure ($P_{in,i}$) and the classic Laplace-Young equation. The recoverability (R) is calculated by $R_{i,j}=V_{i,j+1}/V_{i,1}$, where $V_{i,j}$, the infiltration volume in loading cycle $L_{i,j}$, is defined as the volume change of the LN with infiltration pressure ranging from $P_{max,i-1}$ to $P_{max,i}$. $V_{i,4}$ is determined by volume change of the cycle $L_{i+1,1}$ in the pressure range of $P_{max,i-1}$ and $P_{max,i}$ (Figure 3.8).

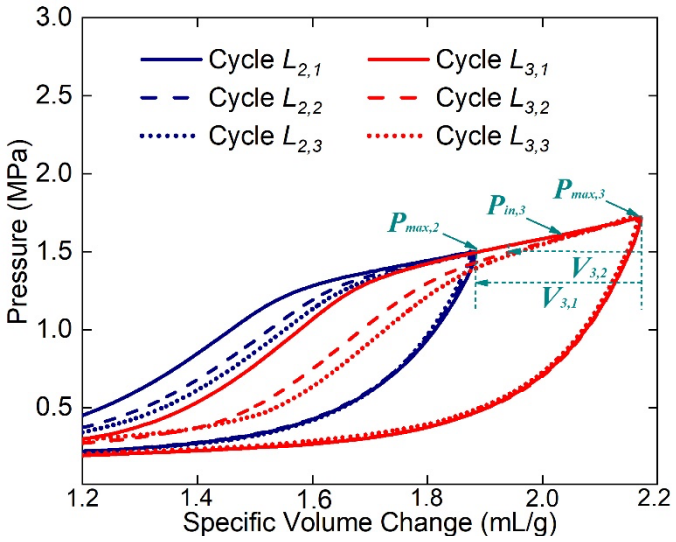

Figure 3.8. Typical sorption isotherm curves of the 2nd and 3rd steps in the consecutive-step test.

Table 3.1. The experimental results of consecutive-step tests of LN containing various aqueous solutions at 20 °C.

i	ri (nm)	Ri,j (%)								
		Water			23 wt% LiCl solution			46 wt% LiCl solution		
		1st	2nd	3rd	1st	2nd	3rd	1st	2nd	3rd
1	150	75±1	63±2	53±2	76±2	65±2	56±2	85±2	82±2	80±2
2	120	80±1	74±1	68±2	82±2	77±2	73±2	90±2	88±1	87±2
3	100	81±2	75±3	68±3	86±2	84±2	83±2	94±2	93±2	93±2
4	85	82±2	76±3	69±4	90±2	87±2	86±2	100±1	100±1	100±1
5	70	83±2	75±5	65±5	93±2	92±2	91±3	100±1	100±1	100±1

Figure 3.9a shows the relationship between D^* and r_i of LN containing various aqueous solutions at 20 °C. Note for smaller pores, D^* is still underestimated here. As the loading

increases, the larger pores are first filled while the smaller ones are empty. As the liquid molecules are forced to enter smaller pores, the larger ones have been already fully filled. Thus, liquid molecules in smaller pores will interact with neighboring larger pores, which is known as "multi-particle interaction"[101]. This multi-particle interaction leads to a reduced D^* for smaller pores in this study. As shown in Figure 3.9a, for water based-LN, D^* increases from 0.75 to 0.83 as the pore size decreases from 150 nm to 70 nm. The trend is consistent with literature results[98], in which Borman et al. observed D^*=0.9 for an LN system composed of water and a hydrophobic silica gel with average pore size of 13 nm. As the concentration of LiCl increases, D^* also increases. As previously validated in the single-step tests, this is due to the reduced gas solubility in liquid phase with higher electrolyte concentration[110,111]. The gas phase tends to be sealed in the nanopore and drives liquid outflow, leading to a larger D^*.

Figure 3.9a also shows that D^* increases as the pore size gets smaller, i.e., it is easier for liquid molecules to flow out from smaller pores than from larger ones at the same infiltration depth. The pore size effect on D^* is associated with the gas-liquid interaction in nanopores. (1) As the pore size decreases, the solvation of the gas phase in confined liquid phase becomes more difficult[108]. In larger pores, the gas molecules can be quickly dissolved in the liquid. However, the water molecules cannot surround and dissolve the gas molecules due to insufficient space in smaller pores, leading to the formation of gas clusters. Therefore, it promotes the retention of the "driving force" for outflow in smaller pores. (2) It is easier for smaller pores to regain the "driving force" if the gas molecules were dissolved in the liquid phase during the loading process. Upon unloading, in smaller pores, the dissolved gas molecules can diffuse back, nucleate and grow in the "sealed end" of the nanopores rather than directly diffuse into the bulk liquid phase, which promotes the liquid outflow as well[107]. With these two synergetic

mechanisms, the value of D^* in smaller nanopores is much larger than that in larger nanopores. Please note that the gas phase effect on liquid outflow can be quantified by measuring the gas pressure in the nanopore during liquid infiltration. However, due to the dynamic gas diffusion process during liquid infiltration, the infiltration pressure or the infiltration depth cannot be directly converted to the gas pressure by ideal gas law.

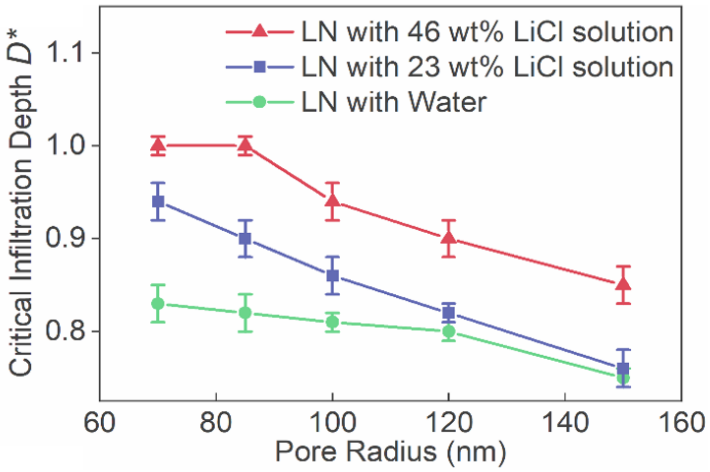

Figure 3.9. Relationship between critical infiltration depth D^* and pore radius r_i of LN containing various aqueous solutions at 20 °C.

The temperature effect on critical infiltration depth (D^*) has also been investigated. Figure 3.10 shows the results of the consecutive-step cyclic tests of water based-LN at different temperatures. The recoverability (R) is summarized in Table 3.2.

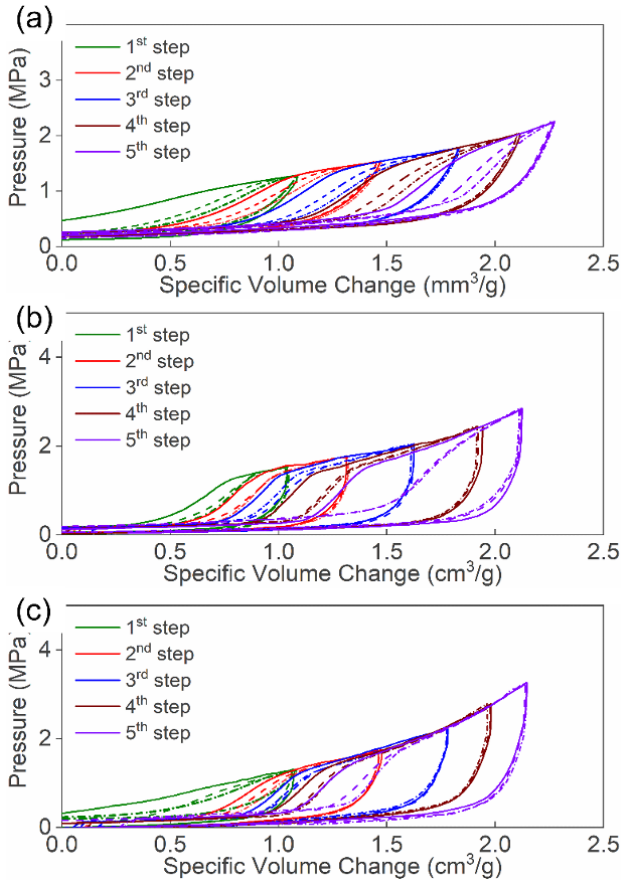

Figure 3.10. The results of the consecutive-step cyclic test (1st to 5th steps) at different temperatures (a) 20 °C (b) 50 °C (c) 80 °C.

Table 3.2. The experimental results of consecutive-step tests of water based LN tests at different temperatures.

i	r_i (nm)	$R_{i,j}$ (%)								
		20 °C			50 °C			80 °C		
		1st	2nd	3rd	1st	2nd	3rd	1st	2nd	3rd
1	150	75±1	63±2	53±2	78±1	74±2	71±2	86±2	83±2	82±2
2	120	80±1	74±1	68±2	81±2	77±2	74±2	92±2	90±1	89±1
3	100	81±2	75±3	68±3	83±2	81±2	80±2	94±1	93±2	93±2
4	85	82±2	76±3	69±4	85±2	82±2	81±2	100±1	100±1	100±1
5	70	83±2	75±5	65±5	86±1	84±2	83±2	100±1	100±1	100±1

Figure 3.11 shows that D^* is sensitive to temperature change. D^* increases at elevated temperature, which suggests that the increased temperature promotes the liquid outflow. This

finding is in agreement with previous works[112,113]. The thermal effect on liquid outflow is attributed to the temperature sensitive outflow pressure[114].

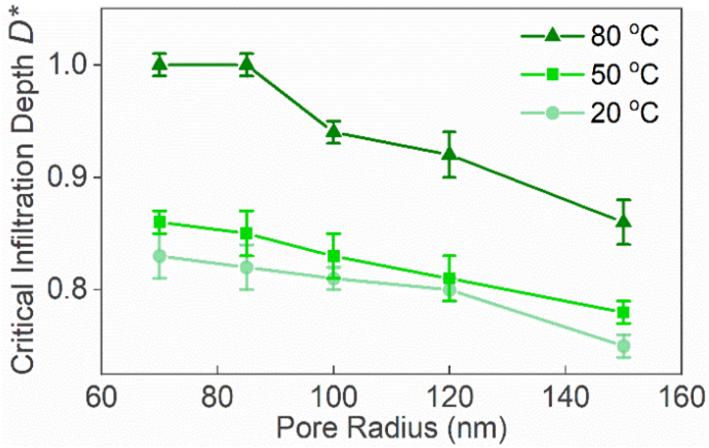

Figure 3.11. Relationship between critical infiltration depth D^* and pore radius r_i of water based LN at different temperatures.

3.5 Conclusion

In summary, the liquid outflow behavior of the LN is experimentally investigated. The system reusability under two different loading modes is distinct from each other. The degree of liquid outflow is a function of the nanopore size. When the nanopore size decreases, both D^* and the degree of liquid outflow increase. This is related to the reduction of gas solubility and diffusion rate in the nano-environment. The smaller the nanopore is, the larger tolerance the system has. With the enhanced D^*, the LN can be implemented for cyclic loading applications as a reusable energy absorber.

Chapter 4. THE EFFECT OF IONS ON GLINE

4.1 Introduction

Liquid motion in nano-environment has immense importance in various applications including gas and petroleum extraction and storage[17,115], membrane-based osmosis and filtering process[116,117], heterogeneous catalytic reactions[118,119], and chromatographic analysis[120]. Recently, a unique pressure-induced liquid motion in hydrophobic nano-channels has been employed as a novel energy mitigation mechanism in Liquid Nanofoam (LN) system[68,86,87]. In an LN system, particles containing open hydrophobic nano-channels are immersed in non-wettable liquid. At ambient condition, the nano-channels are not accessible to the liquid molecules due to the surface energy barrier at the nano-channel entrance[121]. When an external pressure is applied and overcomes the surface energy barrier, the liquid molecules can be compressed into and fill the hydrophobic nano-channels. Under quasi-static loading conditions, large amount of energy is dissipated as heat during the filling. As the energy dissipation mechanism of the LN system is based on the pressure-induced nanoscale liquid motion rather than permanent crushing or plastic buckling of the nano-channels[10], the LN system holds great promise for the development of reusable energy absorbers, which is particularly important for repetitive head impacts in sports and battlefield. The reusability of LN is determined by the degree of liquid outflow from the hydrophobic nano-channels when the external pressure is removed.

Previous studies have suggested that the degree of liquid outflow is related to the morphology of the nanoporous network[26,75], the excessive solid-liquid interfacial tension[64],[65] and the gas oversolubility in naon-environment[43,44,46]. However, there is lack of experimental validation for numerical models. For example, it was predicted by a molecular dynamic model that liquid outflow is impossible in nano-channels with pore size larger than 6 nm[75], which is not

true as we have observed partial liquid outflow in nano-channels with pore size of 120 nm in our previous studies[86,87] and 8.0 nm in this study. The challenge in understanding the liquid outflow mechanism by experimental approaches lies in the coupling effect of the above system determinants. Specifically, changes in the nanoporous network, such as the nanopore size, vary the excessive solid-liquid interfacial tension suggested by the Young-Laplace equation[72] as well as the gas oversolubility[76]. Other experimental work based on a single nanoporous media[64,65] shed light on the effect of ion effect on the liquid outflow. However, the ion concentration in the electrolyte solutions has influence on both the excessive solid-liquid interfacial tension and the gas oversolubility.

In this study, we have successfully decoupled the effect of gas oversolubility from the one of excessive solid-liquid interfacial tension by precisely adjusting the concentration of different electrolytes to keep the surface tension of all liquid phases the same. By immersing nanoporous material with same porous structure and surface properties into these aqueous electrolyte solutions, the excessive solid-liquid interfacial tension of the resulted LN systems has been set as a constant. This approach is capable of individually investigate the effect of the gas oversolubility on liquid outflow from hydrophobic nano-channels.

4.2 Materials and Experiment Setup

The nanoporous material used in current study was a reversed phase silica gel (Fluka 100 C_8, Sigma Aldrich). The as-received material was in powder form, and the particle size was in the range of 40-63um. The nanoporous structure of the material was characterized by a Brunauer–Emmett–Teller (BET) analyzer (ASAP 2020, Micromeritics Instrument Inc.). The measured specific surface area, average pore size, and pore volume of the nanoporous material were 227.4 m^2/g, 8.0 nm, and 0.43 cm^3/g, respectively. Four types of aqueous electrolyte

solutions, 3.04 M NaCl, 3.37 M LiCl, 3.43 M NaBr, and 3.84 M LiBr, were selected and prepared at 23 °C. The surface tension of all aqueous electrolyte solutions was measured by a tensiometer (Model 250, Ramé-Hart).

To prepare the LN specimens, 0.2 g of the reversed phase silica gel was firstly placed at the bottom of a 316-stainless-steel cell as depicted in Figure 4.1. Then, 2.3 mL of aqueous electrolyte solution was slowly dropped into the cell by glass Pasteur pipette. Once the cell was filled by the LN samples, it was sealed by an O-ring fixed on a 316-stainless-steel piston. The diameter of the piston, d, was 12.7 mm. For each aqueous electrolyte solution, three LN specimens were prepared with the same amounts of particle and liquid.

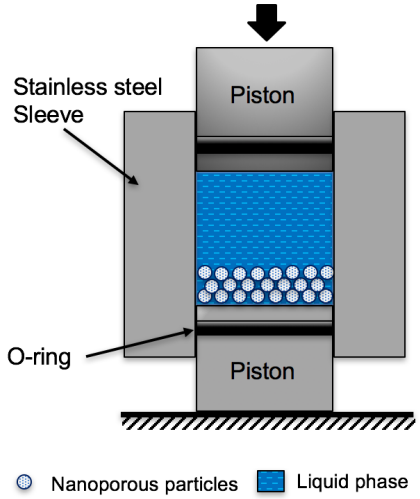

Figure 4.1. Schematic of LN specimen sealed in a testing cell with two pistons.

The sealed testing cell was placed on the platen of a universal tester (Mode 5982, Instron) and compressed at the speed of 2 mm/min. As an external force, F, was applied on the cell, a hydrostatic pressure, *P*, was built in the testing cell and applied on the sealed LN specimen. When the applied load reached 8 kN (equivalent to 63 MPa), the load cell of the Instron machine was moved back at the same speed. The externally applied hydrostatic pressure was calculated as $P = 4F/\pi d^2$. The specific volume change of the LN was calculated as $V = \delta \cdot \pi d^2/4m$, where δ and

m were the measured displacement of the piston and the mass of the nanoporous silica gel, respectively. The loading-unloading cycles were repeated for 3 times for each LN specimen.

4.3 Results

Figure 4.2a shows the typical first loading-unloading cycles of LN specimens containing different aqueous electrolyte solutions. During loading process, the initial response of all LN specimens is linear elastic, as the externally applied hydrostatic pressure is not high enough to overcome the surface energy barrier between the hydrophobic nanopore surface and the non-wetting aqueous electrolyte solutions. As the pressure increases to the liquid infiltration pressure (P_{in}, ~ 17 MPa), the pressure of the first turning point of the loading curve, the liquid molecules are compressed into and fill the nano-channels. The pressure induced liquid filling process and the resulted pressure plateau are referred to as liquid infiltration and the liquid infiltration plateau, respectively. The relationship between the excessive solid-liquid interfacial tension, $\Delta\gamma$, and P_{in} can be described by the classic Laplace-Young equation as $P_{in} = \Delta\gamma / d_n$, where d_n is the nanopore diameter. Upon the completion of nano-channel filling, the slope of the loading curves quickly increases to a value that is slightly higher than the initial elastic one. As the nano-channels are filled with liquid, the nanoporous silica gel is turned into its solid counterpart, which has larger Young's and bulk moduli. All the LN specimens have same excessive solid-liquid surface tension, as they possess same P_{in} and the liquid infiltration plateau.

The surface tension of aqueous solutions is linearly proportional to the molar concentration of electrolytes solutions as illustrated by equation (4.1) [122–124]

$$\gamma_s = \gamma_w + k \cdot c_s \tag{4.1}$$

Where γ_s is the surface tension of the aqueous electrolyte solution at 23 °C, γ_w = 72.18 mN/m is the measured surface tension of water at 23 °C, k is the linear coefficient of electrolyte

at 23 °C, and c_s is the molar concentration of the electrolyte. As listed in Table 4.1, all four selected aqueous electrolyte solutions have the same surface tension.

The measured k values agree with previous literature[122–125]within the experimental error.

Table 4.1. Surface tension and air solubility of selected aqueous electrolyte solutions at 23 °C.

Electrolyte	k (mN·L/m·mol)	c_s (mol/L)	γ_s (mN/m)
3.04 M NaCl	1.44	3.04	76.56 ± 0.59
3.37 M LiCl	1.42	3.37	76.95 ± 0.66
3.43 M NaBr	1.28	3.43	76.57 ± 0.27
3.84 M LiBr	1.18	3.84	76.72 ± 0.93

Combining with the same porous structure and surface condition of the nano-channels, all the LN specimens have same excessive solid-liquid surface tension. This is essential to study the gas phase effect on liquid outflow as the same excessive solid-liquid surface tension ensures that the liquid outflow initiates at same condition.

During unloading, the internal pressure of the LN specimens drops linearly with small volume change at the beginning. With further reduction in the internal pressure, a transition zone with reduced slope is observed. The much reduced slope of the unloading curve as well as the associated large specific system volume change suggest that the confined liquid and gas molecules in the hydrophobic nano-channels start to flow out. The variation of the pressure associated with the transition zone (inset in Figure 4.2a) indicating the influence of the electrolyte types on liquid outflow behavior.

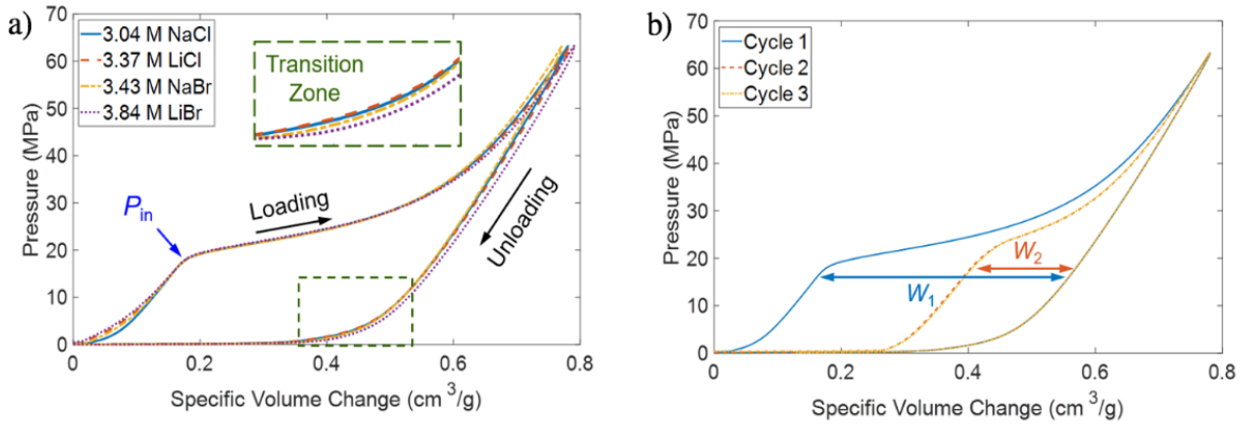

Figure 4.2. Typical loading-unloading cycles of LN specimens containing different aqueous electrolyte solutions: (a) typical first loading-unloading cycles of different LN specimens. The inset shows the difference in transition zone of LN specimens containing different electrolytes, (b) the first three consecutive loading-unloading cycles of LN specimen with 3.04 M NaCl solution.

Although the liquid outflow cannot be directly observed in the unloading portion of the first cycle due to the outflow of mixed liquid and gas from the nano-channel, the degree of liquid outflow can be determined by the liquid infiltration plateau of the second cycle. Figure 4.2b shows the first three consecutive loading-unloading curves of the LN specimen containing 3.04 M NaCl aqueous solution. By comparing the first two loading-unloading cycles, P_{in} is increased while the width of the infiltration plateau is much reduced in the 2nd cycle. This indicates that only partial nano-channel volume is available for liquid infiltration in the 2nd cycle, which is the volume of liquid flowing out of the nano-channel during the unloading process of the 1st cycle. The width of infiltration plateau of each cycle is defined as the specific volume change between the loading and unloading curves at the pressure of 17 MPa, as illustrated in Figure 4.2b. As both the loading and unloading curves of 2nd and 3rd cycles of the LN specimen are nearly identical, only the width of infiltration plateau of 1st and 2nd cycles, W_1 and W_2, are measured and summarized in Table 4.2.

Table 4.2. The measured infiltration plateau width and degree of liquid outflow of LN specimens.

Electrolyte Solution	W_1 (cm^3/g)	W_2 (cm^3/g)	D_{out} (%)
3.04 M NaCl	0.395 ± 0.001	0.162 ± 0.004	41.15 ± 0.94
3.37 M LiCl	0.401 ± 0.010	0.151 ± 0.006	37.57 ± 0.68
3.43 M NaBr	0.395 ± 0.001	0.108 ± 0.010	27.42 ± 2.50
3.84 M LiBr	0.400 ± 0.003	0.072 ± 0.014	18.08 ± 3.32

The measured W_1 is close but smaller than the total pore volume of the nanoporous silica gel, which is due to the van der Waals distance between the liquid molecules and the hydrophobic wall of nano-channels[50,126]. The degree of liquid outflow equals to the reusability of the LN specimens and is defined as $D_{out} = W_2/W_1$.

For LN specimens containing other aqueous electrolyte solutions, the consecutive loading-unloading cycles have the same trend as the NaCl-based system as shown in Figure 4.3.

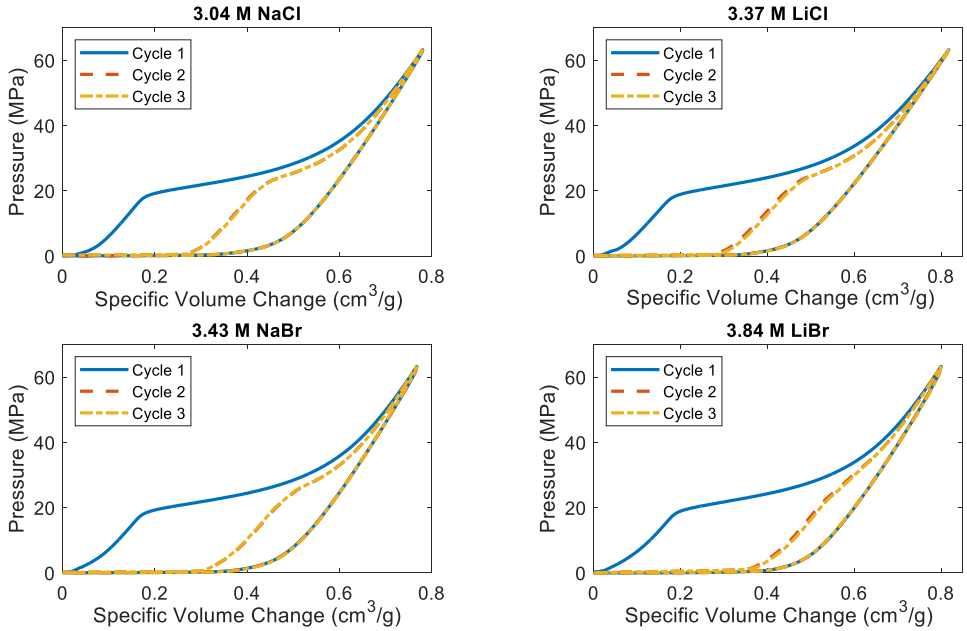

Figure 4.3. Typical loading-unloading curves of LN systems containing different aqueous electrolyte solutions. The 2nd and 3rd cycles are almost identical for all LN systems.

The calculated average degree of liquid outflow of LN specimens is plotted in Figure 4.4. Although all the LN systems have the same excessive solid-liquid interfacial tension, they have different degree of liquid outflow.

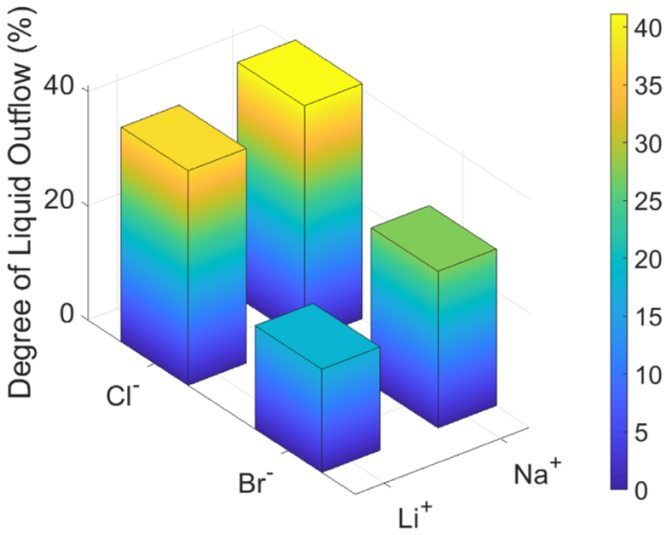

Figure 4.4. Ion effect on the degree of liquid outflow from hydrophobic nano-channels.

4.4 Discussion

As all the LN specimens have same liquid infiltration behavior, the ion effect on the liquid-solid interaction in the nano-channels is identical[83,127,128]. The variation in the degree of liquid outflow should be attributed to the ion effect on GLIHNE. It has been found that the presence of electrolytes reduces the gas solubility in bulk phase due to the "salting-out" effect[35,129,130]. Based on Henry's law and van ´t Hoff equation, the gas solubility in pure water can be quantified as shown in equation (4.2).

$$C_{g,0} = \frac{P_g}{k_{H,0}} \cdot \exp\left[C \cdot \left(\frac{1}{T} - \frac{1}{T_0}\right)\right] \tag{4.2}$$

where $C_{g,0}$ is the gas solubility in water, P_g is the partial pressure of gas, $k_{H,0}$ is the Henry's coefficient at the standard state temperature T_0 = 298 K, C is a constant for specific gas species, and T is the real environmental temperature.

The ion effect on gas solubility can be precisely estimated by the model developed by Schumpe[131], as shown in equation (4.3).

$$\log\left(\frac{C_{g,0}}{C_{g,i}}\right) = \sum(h_i + h_g)C_i \tag{4.3}$$

where $C_{g,i}$ is the gas solubility in aqueous electrolyte solution, h_i and h_g are ion-specific and gas-specific parameters respectively, and C_i is the ion molar concentration in the electrolyte solution.

By considering the air composition as 78.09% of nitrogen, 20.95% of oxygen, 0.93% of argon, and 0.004% of carbon dioxide, the air solubility in water and the aqueous electrolyte solutions is the summation of the gas solubilities. All the calculation results are listed in Tables 4.3.- 4.5.

Table 4.3. Gas solubility in pure water at 23 °C.

	C (K)	$k_{H,0}$ (atm/M)	$k_{H,T}$ (atm/M)	P_g (atm)	$C_{g,0}$ (M)	h_g (L/mol)
N_2	1300	1639.34	1591.77	0.7809	4.91×10^{-4}	-0.008
O_2	1700	769.23	740.17	0.2095	2.83×10^{-4}	0
Ar	1300	714.28	693.55	0.0093	1.34×10^{-5}	-0.009
CO_2	2400	29.41	27.85	0.00004	1.43×10^{-6}	-0.0183

Table 4.4. Ion-specific parameters and molar concentration at 23 °C.

Ion	Li^+	Na^+	Cl^-	Br^-
h_i (L/mol)	0.0691	0.1171	0.0334	0.0137

Table 4.5. Estimated bulk phase gas solubility in selected aqueous electrolyte solutions at 23 °C.

Electrolyte Solution	C_0 (M)	P_B (MPa)	C_B (M)	P_E (MPa)	C_E (M)	f	C_{Nano} (M)
3.04 M NaCl	2.85×10^{-4}	27.67±1.35	7.85×10^{-2}	0.45±0.10	1.55×10^{-3}	27.00	7.70×10^{-3}
3.37 M LiCl	3.71×10^{-4}	26.68±0.53	9.83×10^{-2}	0.51±0.02	2.23×10^{-3}	18.46	6.85×10^{-3}
3.43 M NaBr	2.92×10^{-4}	25.78±1.79	7.49×10^{-2}	0.65±0.13	2.18×10^{-3}	19.29	5.63×10^{-3}
3.84 M LiBr	3.97×10^{-4}	18.87±2.40	7.46×10^{-2}	0.68±0.10	3.08×10^{-3}	13.50	5.36×10^{-3}

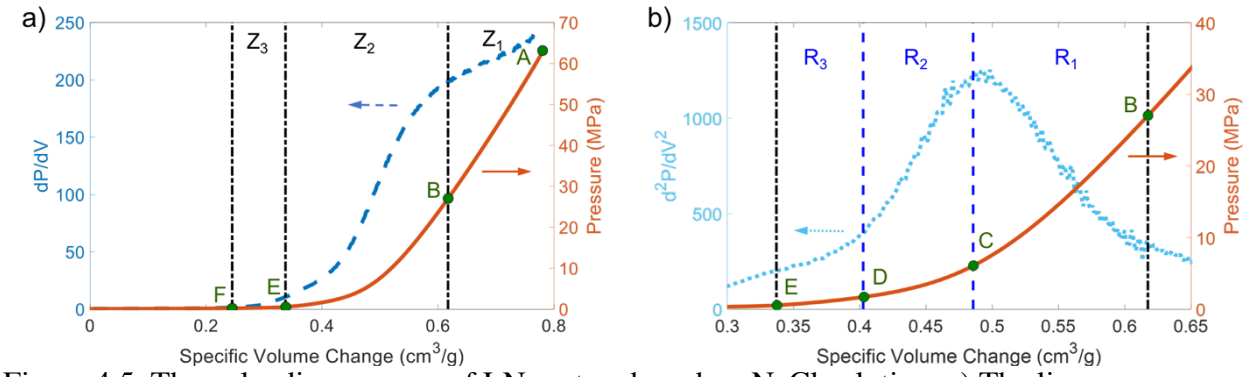

Figure 4.5. The unloading process of LN system based on NaCl solution. a) The linear expansion, transition, and stabilized zones of the unloading curve; and b) The subdivided regions of the transition zone, Z_2.

In Figure 4.5a, the unloading process of LN specimens is divided into three zones by following the slope of the unloading curve (dP/dV), . The first zone (Z_1, from point A to point B) is the linear expansion of the LN system resulted from the reduced external pressure. The second zone (Z_2, from point B to point E) is defined as the transition zone of the liquid outflow. In the transition zone, the significantly dropped slope of the unloading curve indicates that with same dP there is increased specific system volume recovery of the LN system. The pressure at point B of all LN systems (> 18 MPa) significantly promotes bulk gas solubility. According to Henry's law, the bulk gas solubility is linearly proportional to the total pressure applied to the solution. The estimated bulk gas solubility and the internal pressure of the LN at point B are summarized in Table 4.5. Please note that even all the gas initially stored in the nano-channels (~3.29×10^{-6} mol) flows into the bulk liquid phase at this pressure, the gas can be fully dissolved by the bulk electrolyte solutions and would not have much effect on system volume recovery. Therefore, the increased system volume recovery is due to the liquid outflow from the hydrophobic nano-channels. It is noticed that higher P_B promotes the degree of liquid outflow of LN systems. The third zone (Z_3, from point E to point F) has the system volume recovery at nearly constant

internal pressure of the LN. The point F is the ending point of the unloading curve, where the crosshead of the Instron machine is detached from the testing cell and the internal pressure drops to 0 MPa. The total system volume recovery from point B to point F for all the LN specimens is close to the value of W_1. As only partial space in the nano-channels is available for liquid infiltration in the 2nd loading, the total system volume recovery during the 1st unloading process is the combination of liquid and gas outflow from the nano-channels. Different from the loading process, the unloading portion of all 3 cycles follows the exact same path (Figure 4.3). In each cycle, the nano-channels are fully filled by liquid and gas molecules at the peak loading pressure (point A). As the loading-unloading process is continuous, the gas diffusion, a slow time-dependent behavior, can be ignored. Therefore, the unloading process is reset to the same starting point at point A in every cycle.

As the crosshead of the Instron machine moves back at a constant speed, the specific volume change, dV is proportional to time, dt. Therefore, the slope of the unloading curve is an analog of pressure drop speed in the nano-channels (dP/dt). Similarly, d^2P/dV^2 is an analog of pressure deceleration (d^2P/dt^2). By following the "pressure deceleration", the transition zone can be subdivided into 3 regions (Figure 4.5b). In the 1st region (R_1, from point B to point C), the "pressure deceleration" increases. As the pressure in the nano-channels is proportional to the spacing between liquid molecules, i.e. the potential energy of liquid molecules, the increase in pressure deceleration indicating accelerated mass transport from nano-channels to the bulk phase. As the weight of gas is negligible compared to liquid, R_1 is dominated by liquid outflow. In addition, due to the oversolubility[44,132], the liquid phase confined in nano-channels can uptake much more gas than the bulk liquid phase. The gas-liquid interaction is much stronger in the nano-channels than in the bulk phase. Therefore, most of the gas molecules are retained in the

nano-channels. Accompanied with the liquid outflow, the gas concentration in the nano-channels increases, while the potential energy of the liquid molecules decreases quickly. At point C, the pressure deceleration reaches its maximum value and starts to decrease, indicating reduced liquid outflow. In the 2nd region (R_2, from point C to point D), as the pressure drop speed still decreases, the increasing system volume recovery is mainly contributed by gas outflow. This is attributed to the increased gas concentration in the nano-channels. In the 3rd region (R_3, from point D to point E), the pressure deceleration starts to converge to a constant. This is due to the gas escaped from the nano-channels are dissolved by the bulk liquid phase. With the reduced pressure and the increased gas content, the bulk liquid phase is saturated with gas and suppresses gas outflow. The saturated bulk liquid phase is proven by the gas precipitation at further reduced pressure. Gas bubbles have been observed in our previous study[76].

At point E, the pressure deceleration and the pressure in the nano-channels are nearly constants. At this low pressure level, the gas molecules may not be fully dissolved and the pressure change in the nano-channels is more sensitive to the gas volume change rather than the potential energy of the liquid molecules. To maintain the pressure inside the nano-channels, with one unit volume of liquid outflow, one unit volume of gas is precipitated out from the confined liquid molecules. Thus, at point E, the confined liquid in the nano-channels is also saturated with gas. The corresponding gas solubility is about 4.12×10^{-2} M (one unit volume of gas fully dissolved in one unit volume of liquid), which is much higher than the calculated C_E listed in Table 4.5. The ratio between the nano- and bulk- gas solubility is the oversolubility factor, f. The values of f are summarized in Table 4.5. These experimental results are at the same order of values predicted by previous numerical results[16]. The smaller values are due to the presence of electrolytes.

The ion species have influence on C_0, f and D_{out}. In the bulk phase, cation has more prominent effect on gas solubility, as Na^+ based systems have much reduced gas solubility. This is due to the solvated cation structure in the solution. In the nano-channels, both cation and anion have significant effect on the oversolubility factor. This is because the unique ion structure in the nano-channels, where the solvated cation structure cannot fully developed[28]. Instead, the anions have stronger interaction with the water molecules that can otherwise dissolve gas molecules[31]. Na^+ has less effect on f than Li^+, as the gas oversolubility in Na^+ based solutions is closer to that in pure water. Similarly, Cl^- has less effect on f than Br^-. Consequently, the pair of Na^+ and Cl^- has least effect on f, while the pair of Li^+ and Br^- dramatically reduces f. For LiCl and NaBr solutions, their oversolubility factors are similar and in between the values of NaCl and LiBr.

The gas oversolubility in nano-channels of each electrolyte solution at ambient condition, C_{Nano}, can be calculated as $C_0 \cdot f$ and listed in Table 4.5. It seems that higher gas oversolubility leads to higher degree of liquid outflow. However, when the C_{Nano} has higher value, its effect on liquid outflow is weaker (Figure 4.6). In addition, the D_{out} is more sensitive to the species of anion than that of cation as shown in Figure 4.4. This is different from the effect of electrolytes on f. The electrolyte solutions with higher C_{Nano} have stronger interaction with gas molecules and can accommodate more gas molecules in the nano-channels, and thus retain more gas in R_1. In R_2, gas molecules start to escape from the nano-channels. The loss of gas content in the nano-channels equals to the reduced reusability of the system and can be seized only when the bulk liquid phase is saturated with gas. Lower C_0 is desired to quickly shut down the gas transportation from the nano-channels to the bulk phase. Therefore, to enhance D_{out} or the system reusability, lower C_0 and larger f are necessary.

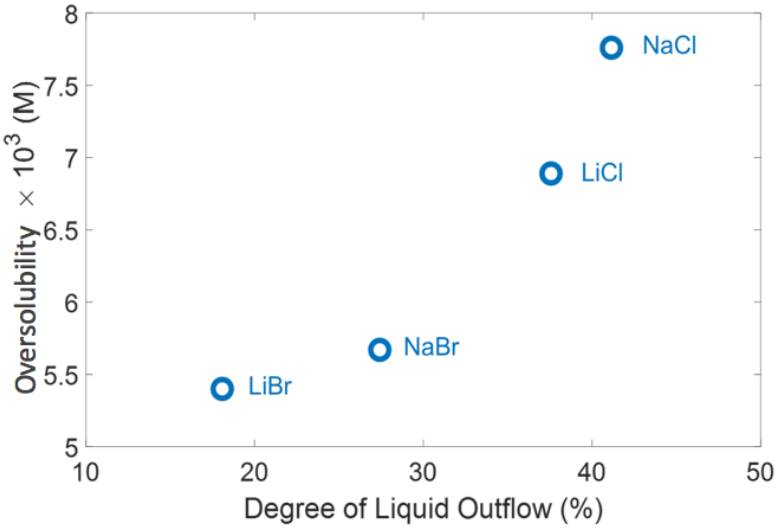

Figure 4.6. The effect of gas oversolubility on the degree of liquid outflow from the nano-channels.

4.5 Conclusion

In summary, the effect of gas oversolubility on liquid outflow from hydrophobic nano-channels has been investigated independently by maintaining the same excessive solid-liquid interfacial tension. The pairs of cations and anions not only alter the gas solubility in bulk phase but also affect the gas oversolubility factor in nano-channels. The degree of liquid outflow from hydrophobic nano-channels is determined by both the bulk solubility and the oversolubility factor. Controversially to the bulk phase, anion has more effect on the degree of liquid outflow and the system reusability than cation. These findings not only provide design guidelines for reusable nanofluidics-based energy absorbers, but also extend the knowledge of gas-liquid interaction in confined environment.

Chapter 5. EFFECT OF EXTRA GAS AMOUNT ON GLIHNE

5.1 Introduction

Liquid flow in nanopores is of great importance for a variety of applications, including water filtration[133,134], drug delivery[135,136], heterogeneous catalysis[137,138], chemical and bio-sensing[139,140], and many others. Specially, forced liquid flow in hydrophobic nanopores is employed as a novel mechanism for energy storage and mitigation in a liquid nanofoam (LN) system[68,88,141]. In an LN system composed of a hydrophobic nanoporous media and a non-wetting liquid, the liquid molecules are forced into the nanopores when the applied external load is sufficient to overcome the capillary force. As the external load is removed, the intruded liquid can be fully or partially expelled from the hydrophobic nanopores[87,142]. Due to its highly hysteretic mechanical response, tremendous amount of energy is mitigated by the LN system. With the liquid outflow, the LN system recovers its energy mitigation capacity and is capable of mitigating repetitive impacts. The system recoverability of LN is determined by the degree of liquid outflow from the hydrophobic nanopores during the load releasing process. Therefore, understanding the underlying mechanism of this confined liquid outflow behavior is essential to develop advanced energy absorption system for repetitive impacts in sports, battlefield, and transportation. Moreover, the elucidation and manipulation of the nanoscale liquid outflow will provide important insights and immediate guidance for designing other systems consisting of liquid and nanoporous media such as thermal actuators[143,144] and ionic-liquid based supercapacitors[145].

The liquid outflow from hydrophobic nanopores have been studied by many researchers and it has been found that the liquid outflow behavior in nano-environment is related to the excessive liquid-solid interfacial tension[65,127,146], nanoporous structure[92], and liquid-gas

interaction[26]. For example, the addition of potassium chloride increases the excessive liquid-solid interfacial tension of the LN system and promotes the degree of liquid outflow[65]. In addition to the liquid-solid interaction in the nano-environment, it has also been demonstrated by molecular dynamics simulations that liquid outflow can be significantly promoted by a single gas molecule[26]. In our previous works[142,147], reduced gas solubility in the liquid phase endows the LN system with higher degree of liquid outflow. Sun et al.[109] also reported liquid outflow has been improved by hindering the time-dependent mass transportation in the nanopores. However, experimental studies on the gas phase effect is still scarce. There is lack of a comprehensive understanding of the mechanism underpinning liquid outflow and the fundamentals of liquid-gas interaction in the nano-environment. An experimental approach to individually investigate the gas phase effect on liquid outflow is in high demand.

In this study, we have thoroughly studied the gas phase effect on the liquid outflow by introducing different amount of gas into LN systems with constant excessive liquid-solid interfacial tension. The degree of liquid outflow in these LN systems are characterized by cyclic quasi-static compression tests. The results show that the degree of liquid outflow is promoted as the amount of gas increases. Further theoretical analysis reveals that the fast gas saturation of the bulk liquid and the enhanced bubble nucleation in the hydrophobic nanopores suppress gas outflow but promote liquid outflow.

5.2 Material and Experimental Setup

The nanoporous material used in current study was a hydrophilic nanoporous silica (SP-120-20, DAISO Fine Chem USA, INC.). The as-received material was in powder form, with an average pore size of 12 nm and particle size around 20 μm. The specific pore volume of the nanoporous silica was 700 mm^3/g. The pore size distribution and specific pore volume were

confirm by the BET analysis (ASAP 2020, Micromeritics Instrument Inc.), as shown in Figure 5.1.

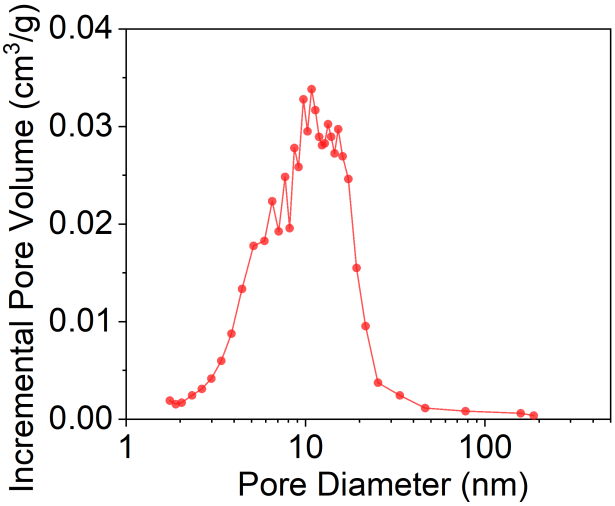

Figure 5.1. Pore size distribution of nanoporous silica SP-120-20 characterized by an ASAP 2020 porosimetry system.

To make its surface hydrophobic, a thin layer of chloro(dimethyl)octylsilane was anchored onto the nanopore surface, as previously reported[86,87]. Briefly, 1 g of silica gel was mixed with 40 mL of anhydrous toluene. 10 mL of chloro(dimethyl)octylsilane and 1 mL of pyridine were then injected into the mixture. The mixture was gently stirred at 95 ºC for 18 h, after which the surface-treated silica gel was filtered, washed with ethanol, and dried for at least 24 h before use. The liquid phase of the LN was de-ionized (DI) water.

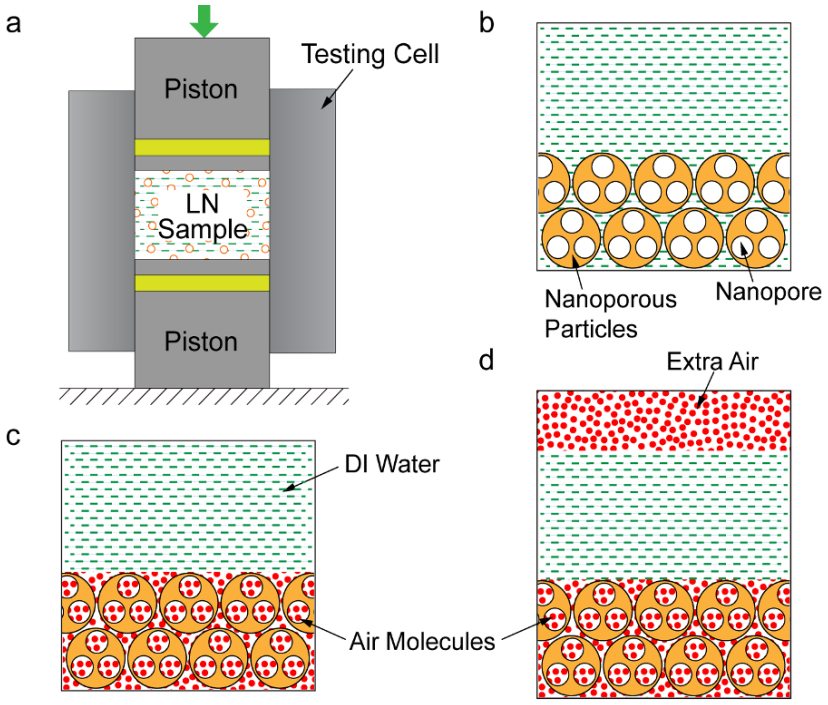

Figure 5.2. Schematic of the experimental setup and LN samples containing various amount of air (a) the quasi-static compression test of LN sample sealed in a testing cell (b) the degassed LN sample, LN-V (c) the LN sample without degassing, LN-N (d) the LN sample with extra gas, LN-EL and LN-EM.

The LN sample was prepared by sealing 0.2 g of surface-treated silica gel and 1.5 mL of DI water in a stainless-steel testing cell with two O-ring equipped pistons, as shown in Figure 5.2a. The cross-sectional area of the pistons, A, was 286 mm^2. Four types of LN samples were prepared with same amount of silica gel and DI water but different amount of the gas phase, i.e. air. LN sample, denoted as LN-V (Figure 5.2b), was prepared by placing the mixture in vacuum (< 3 KPa) for several hours to minimize the amount of air in the nanopores and the bulk liquid phase. The LN sample prepared at ambient condition without degassing was denoted as LN-N, which contained small amount of air trapped in between hydrophobic silica gel particles (Figure 5.2c). Extra gas was introduced into the LN sample by sealing an additional air column in the testing cell, forming LN sample LN-EL and LN-EM (Figure 5.2d). The detailed LN sample

information is summarized in Table 5.1. The gas volume in the nanopores was calculated as $V_i = m \cdot V_{sp}$, where m and V_{sp} were the mass and specific pore volume of the silica gel, respectively. The volume of extra gas in the LN was determined by $V_o = A \cdot l - (V_{DI} + m/\rho + V_i)$, where l was the total length of the sealed LN sample, V_{DI} was the volume of DI water, and ρ was the density of silicon dioxide. The gas to liquid volume ratio of the prepared LN samples at ambient condition was calculated as $\phi = (V_i + V_o)/V_{DI}$.

Table 5.1. LN sample information.

Sample	m	V_{DI}	V_i	V_o	P_d	ϕ
LN-V	0.2 g	1.5 mL	0	0	0	0
LN-N	0.2 g	1.5 mL	0.14 mL	0.08 mL	0.3 MPa	15%
LN-EL	0.2 g	1.5 mL	0.14 mL	0.75 mL	2.9 MPa	60%
LN-EM	0.2 g	1.5 mL	0.14 mL	1.95 mL	7.7 MPa	140%

LN sample sealed in the testing cell was compressed by a universal tester (Floor Model 5982, Instron, Inc.) at the speed of 2 mm/min. For each type of LN, three samples were tested. The applied force, F, increased gradually to 10 kN, leading to an equivalent pressure of 35 MPa in the testing cell. As the peak force was reached, the Instron crosshead was moved back at the same speed. To study the liquid outflow behavior of the LN, the compression test was repeated at least three times for each LN sample. The hydrostatic pressure in the testing cell was calculated as $P = F/A$. The specific volume change of the LN sample was calculated as $\Delta V = A \cdot \delta/m$, where δ was the measured piston displacement.

5.3 Results

Figure 5.3a shows typical consecutive loading-unloading cycles of an LN sample. Only the 1st and 2nd loading-unloading cycles are shown here, since all subsequent cycles are nearly identical to the 2nd one. At ambient condition, the water molecules stay outside of the nanopores due to the surface hydrophobicity. As the external force is applied, initially, the mechanical

response of LN samples is nearly elastic and the system bulk moduli is contributed by both liquid and solid compositions. When the pressure reaches approximately 13 MPa, the slope of the loading curve shows considerable reduction and an infiltration plateau with the smallest slope of the loading curve is formed. This corresponds to the water molecules being forced into the nanopores, referred to as the liquid infiltration process. The pressure at which liquid infiltration occurs is defined as the liquid infiltration pressure, P_{in}, which is governed by the classic Laplace-Young equation, $P_{in} = 2\Delta\gamma/d$, where $\Delta\gamma$ is the excessive solid-liquid interfacial tension and d is the nanopore diameter. As all the nanopores are filled with water molecules, the liquid infiltration plateau ends as indicated by the next turning point at 22 MPa. The effective nanopore volume of the LN, which is determined by the width of the infiltration plateau W_1, is around 690 mm^3/g. Thereafter, the LN system becomes elastic again. Upon unloading, the pressure drops quickly in a linear manner at the beginning. As the pressure further reduces, the slope of the unloading curve starts to decrease. The reduced slope of the unloading curve as well as the associated specific volume change indicate the combined liquid and gas outflow from the hydrophobic nanopores.

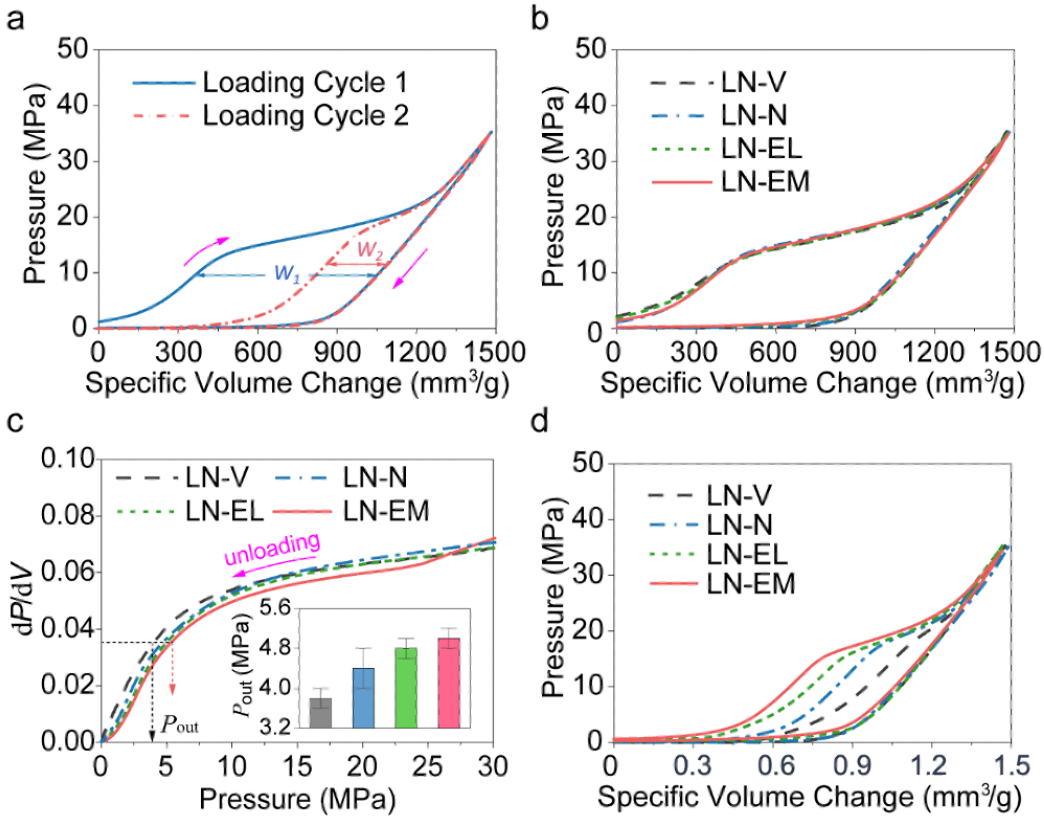

Figure 5.3. Quasi-static compression testing results of different LN samples (a) typical consecutive loading-unloading cycles of an LN sample (b) typical first loading-unloading cycles of different LN samples (c) reduced slope of the unloading curves in the first cycles of different LN samples (d) typical second loading-unloading cycles of different LN samples.

When the external pressure is removed, both confined gas and liquid molecules start to flow out from the nanopores. It is difficult to quantify the volume of liquid outflow by analyzing the unloading curve. Instead, the width of the liquid infiltration plateau in the second loading-unloading cycle is a direct measure. In the second cycle, the LN system shows similar hysteric loading-unloading response. However, compared with the first cycle, P_{in} is increased, while the width of the infiltration plateau, W_2, is much smaller. The reduced infiltration plateau width suggests that the volume of nanopores is only partially available in the second cycle, which is due to the partial liquid outflow from the nanopores in the first cycle. The volume of the liquid

outflow is equivalent to the volume of gas retained in the hydrophobic nanopores. Therefore, the degree of liquid outflow from nanopores or the degree of gas retention in the nanopores, D_{out}, is defined as

$$D_{\mathrm{out}} = W_2/W_1 \tag{5.1}$$

Figure 5.3b shows the typical first loading-unloading cycles of four LN samples. The curves are shifted along the x-axis for better comparison. During the loading process, the mechanical response of four LN samples is nearly the same, i.e. neither the effective pore volume W_1 nor the liquid infiltration pressure P_{in} of the LN is affected by the considerably increased amount of gas phase. Since all the LN samples possess same P_{in}, according to the classic Laplace-Young equation, the excessive surface tension at the solid-liquid-gas interface is a constant. The additional gas content has negligible effect on the interfacial tension. As the excessive solid-liquid-gas interfacial tension significantly affects the liquid outflow behavior[127,146], maintaining it as a constant is crucial for the investigation of the gas phase effect. During unloading, the fast linear reduction in system pressure ends at a higher pressure when the LN sample contains larger gas volume. The above described identical loading process and difference in unloading process indicate that the additional gas volume in LN systems has prominent effect on the combined gas and liquid outflow from the hydrophobic nanopores.

Table 5.2. Measured effective pore volume and calculated degree of liquid outflow of different LN samples.

Sample	W_1 (mm^3/g)	W_2 (mm^3/g)	D_{out} (%)	P_{out} (MPa)
LN-V	690 ± 9	119 ± 8	17 ± 1	3.8 ± 0.2
LN-N	692 ± 6	232 ± 11	34 ± 1	4.4 ± 0.4
LN-EL	695 ± 9	330 ± 13	47 ± 2	4.8 ± 0.2
LN-EM	688 ± 7	407 ± 17	59 ± 2	5.0 ± 0.2

When the linear unloading ends, the system volume expands more with unit pressure reduction. This indicates confined gas and liquid molecules flow out from the nanopores and the corresponding critical pressure is defined as the outflow pressure, P_{out}. To further quantify P_{out}, the slope of the unloading curves (dP/dV) is plotted versus the system pressure in Figure 5.3c. The increased V_o reduces the effective bulk modulus of the resulted LN samples, which is validated by the reduced slope from 30 MPa to 15 MPa. P_{out} is quantified when the slope (dP/dV) is reduced to 0.35 and increases from 3.8 MPa (LN-V) to 5.1 MPa (LN-EM) with increasing ϕ (inset in Figure 5.3c and Table 5.2). Concurrently, W_2 monotonically increases with increasing ϕ (Figure 5.3d and Table 5.2). Since all the LN samples have similar W_1, D_{out} increases from 17% to 59% with the promoted P_{out} (Figure 5.4a and Table 5.2), as ϕ increases from 0 to 140% (Figure 5.4b). The degree of liquid outflow is significantly enhanced by the only system variable, i.e. the extra gas in the LN systems.

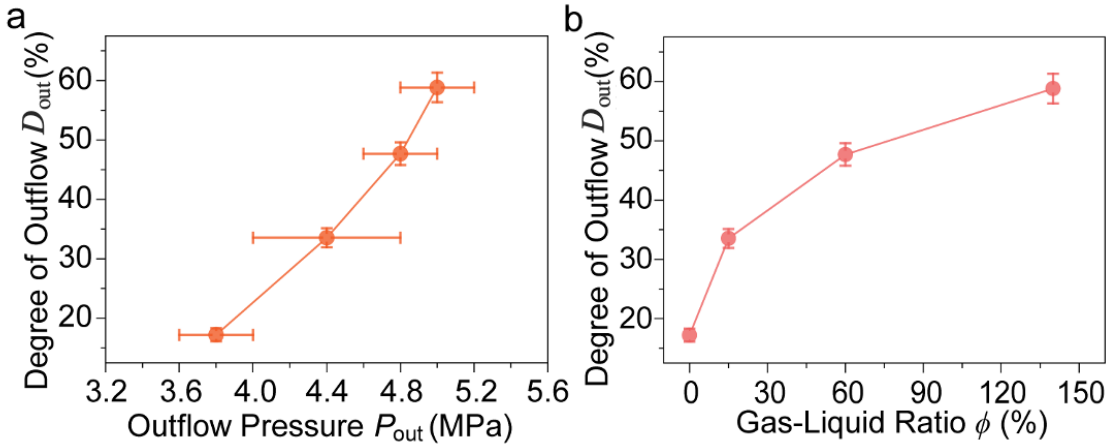

Figure 5.4. Degree of liquid outflow as a function of (a) P_{out}, the outflow pressure and (b) ϕ, the gas-liquid ratio.

5.4 Discussion

At the molecular level, as all the LN samples have identical excessive solid-liquid interfacial tension, the variation in D_{out} is attributed to the enhanced liquid-gas interaction in the

nanopores in the unloading process. During the loading process, the system pressure gradually increases and gas molecules are dissolved into the bulk and confined liquid phases in a stepwise manner (Figure 5.5 a-c). First, the gas outside nanopores are dissolved into the bulk liquid (Figure 5.5b). According to Henry's law, the bulk gas solubility is proportional to the system pressure[148]

$$C_{\mathrm{g}} = P_{\mathrm{g}}/k_{\mathrm{H,T}} \tag{5.2}$$

where C_{g} is the gas solubility in bulk liquid, P_{g} is the partial pressure of gas, and $k_{\mathrm{H,T}}$ is the Henry's coefficient at temperature T. At 1 atm, the air solubility is 7.6×10^{-4} M. The pressure at which all the extra air molecules outside nanopores are dissolved into the bulk liquid phase, denoted as P_{d}, is calculated and summarized in Table 5.1. P_{d} is much smaller than the infiltration pressure P_{in}. Therefore, all the air molecules outside nanopores are fully dissolved into the bulk liquid phase before liquid infiltration occurs. During liquid infiltration process, the bulk liquid phase (both water and dissolved air molecules) starts to enter the nanopores and dissolves the confined air molecules. Due to the gas oversolubility in the nanopores (more than ten times higher than bulk solubility[43,44,46,132,142]), all air molecules inside the nanopores are dissolved by the intruded liquid phase (Figure 5.5c). The calculated gas concentration in the bulk liquid $c_{\mathrm{b,0}}$ as well as in the nanopores $c_{\mathrm{n,0}}$ are summarized in Table 5.3 and plotted in Figure 5.5d. The values of $c_{\mathrm{b,0}}$ and $c_{\mathrm{n,0}}$ increase with ϕ, while the concentration difference $\Delta c_0 = (c_{\mathrm{b,0}} - c_{\mathrm{n,0}})$ is a constant.

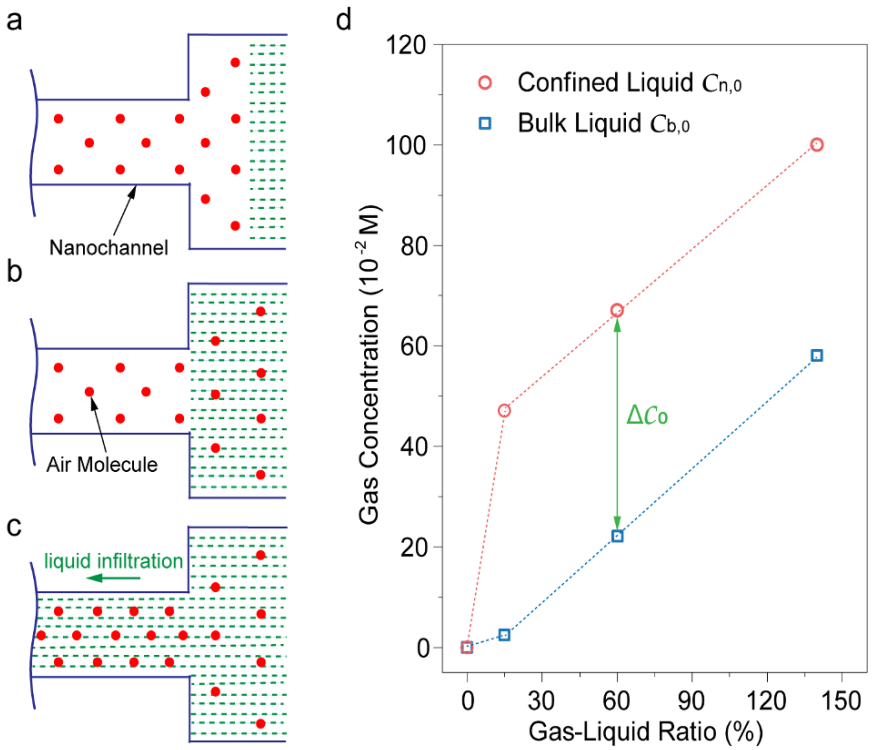

Figure 5.5. (a-c) Stepwise gas molecules dissolution into the bulk and confined liquid phases (d) gas concentration in the bulk and confined liquid at peak pressure.

Table 5.3. Gas concentration in the bulk liquid, $c_{b,0}$ and gas concentration in the nanopores, $c_{n,0}$ at peak pressure.

Sample	$c_{b,0}$ (M)	$c_{n,0}$ (M)	Δc_0 (M)
LN-V	0	0	0
LN-N	2.4×10^{-3}	4.7×10^{-2}	4.4×10^{-2}
LN-EL	2.2×10^{-2}	6.7×10^{-2}	4.4×10^{-2}
LN-EM	5.8×10^{-2}	1.0×10^{-1}	4.4×10^{-2}

As the unloading process begins, the initial linear response (Figure 5.3b-c) is due to the linear volume expansion of the bulk liquid phase resulted from the reduced system pressure. As the total volume change of the LN systems is small and the sudden pressure drop (~ 20 MPa reduction in 5 s), the liquid outflow from the nanopores to the bulk liquid phase is limited and negligible.

When the linear unloading ends ($dP/dV \approx 0.06$ in Figure 5.3c), instead of the linear volume expansion, the combined liquid and gas outflow from the nanopores to the bulk liquid phase dominates the system volume recovery. Particularly, the gas outflow includes gas diffusion and advection from the nanopores to the bulk liquid phase. As stated in Fick's law[149], the gas diffusion flux is directly proportional to the concentration gradient. Since Δc_0 is a constant for all LN samples except LN-V, the initial gas molecules diffusion rates are exactly the same. In addition, the gas diffusion is a slow process, given the unloading process is completely in less than a minute, the amount of gas diffusing from the nanopores to the bulk liquid phase can be ignored.

The gas advection is defined as the dissolved gas molecules flow out from the nanopores to the bulk liquid phase with the liquid, driven by the increased intermolecular spacing in the nanopores. The gas advection flux is proportional to the mass transfer velocity and the gas concentration at the interface between nanopores and the bulk liquid phase. Since the system volume recovery is controlled at a constant rate (2 mm/min), the initial mass transfer velocities of all LN samples are the same. The advection-induced gas concentration reduction is

$$\Delta c_{\mathrm{n,a}}(t) = \int_0^t k_{\mathrm{a}}(\tau) \cdot c_{\mathrm{n}}(\tau) \mathrm{d}\tau \tag{5.3}$$

where k_{a} is a time-dependent parameter and c_{n} is the gas concentration in liquid confined in the nanopores at time τ. The gas outflow process leads to gas concentration decrease in the confined liquid and increase in the bulk liquid (Figure 5.6a-b).

Given the large and quick pressure drop in the linear unloading process, the bulk gas solubility is reduced accordingly based on the Henry's law. Therefore, the gas molecules escaped from the nanopores quickly saturate the bulk liquid phase. As the bulk liquid phase is not capable of accommodating more gas molecules, the gas outflow from nanopores is blocked (Figure 5.6b).

The critical pressure, at which the gas saturation occurs, is defined as the blocking threshold pressure of gas outflow, P_t. Given $c_{n,0} \geq c_{b,0}$, the liquid flowing out from the nanopores has higher gas concentration than that of the liquid intrudes into the nanopores during loading process. Therefore, with the additional gas outflow, the bulk liquid phase is saturated at higher pressure ($P_t > P_d$) for a given LN system. The total time needed to saturate the bulk liquid phase is defined as the threshold time of gas outflow, t_0.

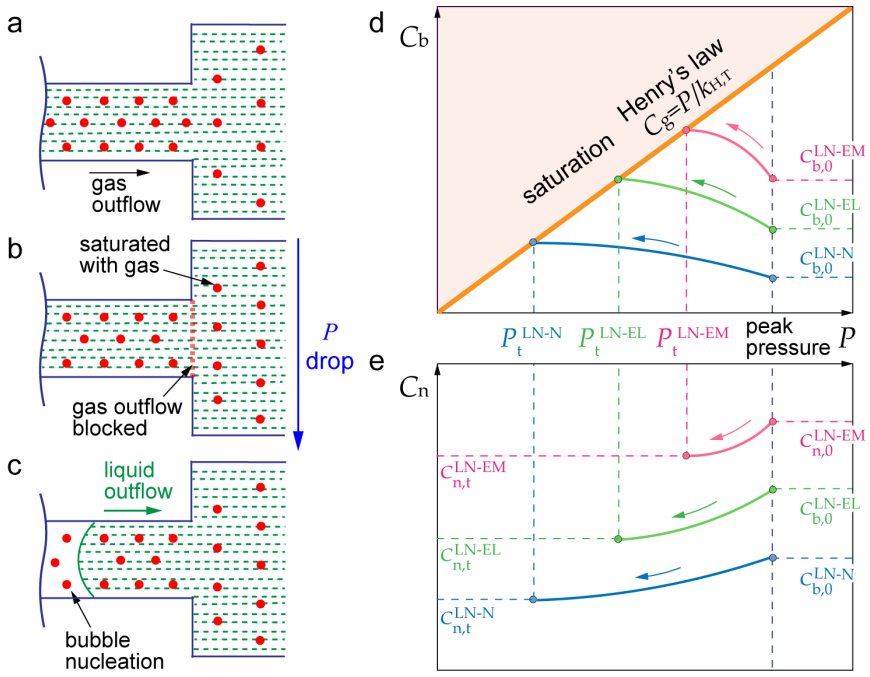

Figure 5.6. (a-c) Liquid outflow and bubble nucleation in nanopores (d) schematic of gas concentration increase contour in the bulk liquid phase (e) schematic of gas concentration decrease contour in the nanopores.

When the bulk liquid is saturated during the unloading process, the bulk gas concentration is

$$c_b(t_0) = c_{b,0} + \frac{V_i}{V_{DI} - V_i}\Delta c_{n,a} = P_t/k_{H,T} \tag{5.4}$$

Accordingly, the bulk gas concentration increase contour in LN specimens is qualitatively sketched versus the system pressure in Figure 5.6d. For LN samples with extra gas, both $c_{\mathrm{b},0}$ and $\Delta c_{\mathrm{n,a}}$ increases with ϕ. For LN-V sample, the gas content in the LN-V has been minimized and the bulk phase will never be saturated with gas, i.e. $P_{\mathrm{t}}^{\mathrm{LN-V}} = 0$. From equation (5.4) and Figure 5.6d, $P_{\mathrm{t}}^{\mathrm{LN-EM}} > P_{\mathrm{t}}^{\mathrm{LN-EL}} > P_{\mathrm{t}}^{\mathrm{LN-N}} > P_{\mathrm{t}}^{\mathrm{LN-V}}$. As the LN samples are completely sealed, the total gas amount is conservative. The gas amount increase in the bulk phase is equivalent to the gas amount decrease in the nanopores. Thus, when the bulk liquid is saturated during the unloading process, the gas concentration in the nanopores is

$$c_{\mathrm{n}}\left(t_0\right) = c_{\mathrm{n},0} - \Delta c_{\mathrm{n,a}} \tag{5.5}$$

As depicted in Figure 5.6e, as the gas outflow is ceased at a higher threshold pressure, more gas molecules are retained in the confined liquid, i.e. $c_{\mathrm{n,t}}^{\mathrm{LN-EM}} > c_{\mathrm{n,t}}^{\mathrm{LN-EL}} > c_{\mathrm{n,t}}^{\mathrm{LN-N}} > c_{\mathrm{n,t}}^{\mathrm{LN-V}}$. At the threshold pressure, although the bulk liquid has been saturated, the gas remained in the nanopores are still dissolved by the confined liquid due to the oversolubility in the nano-environment. In short, both P_{t} and $c_{\mathrm{n}}\left(t_0\right)$ increase with ϕ.

Once the gas outflow is ceased, the free energy of the confined liquid in the nanopores starts to increase with system pressure reduction. To maintain the minimum system free energy, liquid-gas phase separation takes place in the nano-environment, i.e. bubble nucleation occurs (Figure 5.6c). According to classic bubble nucleation theory in the absence of gas phase[107,150,151], the formation of a vapor nucleus increases the system free energy by (i) $\gamma_{\mathrm{sv}}A_{\mathrm{sv}}$, where γ_{sv} is the solid-vapor interfacial tension and A_{sv} is the solid-vapor interface area; (ii) $\gamma_{\mathrm{lv}}A_{\mathrm{lv}}$, where γ_{lv} is the liquid-vapor interfacial tension and A_{lv} is the liquid-vapor interface area; and (iii) $P_{\mathrm{out}}V$, where P_{out} is the liquid outflow pressure and V is the volume recovery of the LN system. On the other

hand, the system free energy is reduced due to the surface hydrophobicity by $\Delta\gamma A_{\mathrm{ls}}$, where A_{ls} is the liquid-solid interface area. Thus, a thermodynamic equilibrium is expressed as

$$\gamma_{\mathrm{sv}}A_{\mathrm{sv}} + \gamma_{\mathrm{lv}}A_{\mathrm{lv}} + P_{\mathrm{out}}V = \Delta\gamma A_{\mathrm{ls}} \tag{5.6}$$

The above equilibrium well describes the phase separation process in the confined nano-environment. However, the gas phase, which has strong interaction with the confined liquid and influences the liquid outflow behavior, exists. In this case, the confined gas solution becomes supersaturated[152,153] given that no gas molecules exist in the vapor bubble. Based on Henry's law, the excessive gas molecules tend to separate from the confined liquid into the vapor phase, releasing the system free energy by $P_{\mathrm{g}}V_{\mathrm{g}} = C_{\mathrm{n,t}}k_{\mathrm{H,T}}V_{\mathrm{g}}$, where V_{g} is gas volume separated from the confined liquid phase. Then, the above thermodynamic equilibrium equation is modified as

$$\gamma_{\mathrm{sv}}A_{\mathrm{sv}} + \gamma_{\mathrm{lv}}A_{\mathrm{lv}} + P_{\mathrm{out}}V = \Delta\gamma A_{\mathrm{ls}} + C_{\mathrm{n,t}}k_{\mathrm{H,T}}V_{\mathrm{g}} \tag{5.7}$$

from which the liquid outflow pressure is calculated as

$$P_{\mathrm{out}} = \frac{k_{\mathrm{H,T}}V_{\mathrm{g}}}{V}C_{\mathrm{n,t}} + \frac{\Delta\gamma A_{\mathrm{lv}} - \gamma_{\mathrm{sv}}A_{\mathrm{sv}} - \gamma_{\mathrm{lv}}A_{\mathrm{lv}}}{V} \tag{5.8}$$

P_{out} is promoted by the retained gas concentration in the confined liquid. This trend agrees well with our experimental results (inset in Figure 5.3c) as well as literature results[154], in which the supersaturation limit pressure increases with the increase of dissolved gas concentration in bulk liquid.

Based on the above analysis, when the unloading starts, the gas and liquid molecules flow out from the nanopores to the bulk liquid. The gas outflow is blocked once the bulk phase is saturated, while the liquid outflow continues. For the LN sample containing higher gas content, the gas outflow suppression (Figure 5.6b) as well as bubble nucleation (Figure 5.6c) occur at a higher threshold pressure due to the faster bulk liquid saturation and the enhanced liquid-gas interaction in the gas-supersaturated liquid in the nanopores. Consequently, the higher system

free energy reduction resulted from the releasing of gas molecules from confined liquid to vapor phase drives more liquid out, leading to a higher D_{out}.

5.5 Conclusion

In summary, we have independently investigated the gas effect on the liquid outflow from hydrophobic nanopores by maintaining the excessive solid-liquid interfacial tension as a constant. The degree of liquid outflow from hydrophobic nanopores is found to be a function of the amount of gas in the LN samples. Higher amount of gas blocks the gas outflow at a higher threshold pressure, and thus retains more gas molecules in the nanopores. The additionally retained gas molecules promotes the bubble nucleation process and results higher degree of liquid outflow.

Chapter 6. TIME AND PRESSURE EFFECT ON GLIHNE

6.1 Introduction

Understanding the gas-liquid interaction in nano-environment is of great importance to a number of natural and technical processes, such as shale gas exploitation[23,24], gas-diffusion electrodes[155,156], geological carbon dioxide (CO_2) sequestration[16,157], and gas-liquid membrane contactors[117,158]. The dissolved gas diffusion in pressurized liquid confined in nano-environment plays a key role in these processes. In nanopores with characteristic pore sizes comparable to those of gas and liquid molecules, the classic diffusion theories break down. For instance, the gas solubility in nanoconfined-liquid is much higher than that in bulk liquid and has been observed in various gas-liquid combinations, including CO_2, H_2, or CH_4 dissolved in water, n-hexane, or ethanol confined in nanoporous silica, MCM-41, and SBA-15[43,47,48,159]. This gas oversolubility significantly affects the gas diffusion behavior in confined nano-environment. Besides, pressure effect on gas diffusion in bulk liquid is negligible due to the incompressible mean free path of bulk liquid molecules[29,55], while pressure change results in condensation of liquid molecules[49,53] and gas clusters[26] under hydrophobic nanoconfinement. These density changes pose a noteworthy impact on the nanoscale gas diffusion process. Li et al[45]. have found that the characteristics of CO_2 diffusivity in water under nanoconfinement is different from its bulk counterpart through molecular dynamic (MD) simulation. However, despite the importance of gas diffusion in nanoconfined-liquid, an elucidation of the time- and pressure- dependent diffusion process is currently lacking and experimental studies, suffered from the technical challenges at nanoscale, are still scarce.

A recently developed nanofluidics-enabled energy absorption system, referred to as liquid nanofoam (LN)[66,68,147,160], is a potential platform to experimentally investigate the gas diffusion

behavior in nanoconfined liquid. LN is composed of a hydrophobic nanoporous media and a non-wetting liquid phase. The nanopores are initially filled with gas molecules as their hydrophobic surface inhibits the entering of liquid molecules. When the LN system is pressurized to a critical value, the liquid molecules infiltrate into the nanopores and dissolve all the gas molecules. This liquid infiltration process is a novel energy mitigation mechanism with unprecedented energy absorption efficiency (~100 J/g), nearly 2 orders of magnitude higher than traditional materials[66,126]. As the pressure is removed, the spontaneous liquid outflow from the hydrophobic nanopores is driven by the gas-liquid interaction[109,147]. It has been demonstrated that the degree of liquid outflow reduces with the increase amount of gas escaped from the nanoconfined-liquid to the bulk liquid phase[142,161]. Previous studies on this gas transfer from the nano to bulk phases are focused on advection, while the gas diffusion is ignored due to the relatively short time duration of the liquid outflow process. In current study, the gas diffusion from the nano to bulk phases is thoroughly studied by holding the infiltrated liquid molecules in the hydrophobic nanopores at different peak pressures with variable time durations.

6.2 Materials and Methods

The nanoporous material used in the LN system was a hydrophobic silica gel (Fluka 100 C8, Sigma-Aldrich). The material was in powder form, with the particle size of 40-63 um. The average pore size, nanopore volume, and Brunauer-Emmett-Teller (BET) surface area were 8.0 nm, 0.43 cm^3/g, and 227.4 m^2/g respectively, measured by a surface area and porosity analyzer (ASAP 2020, Micromeritics Instrument Inc.). The liquid phase in the LN system was a 3.0 M sodium chloride (NaCl) aqueous solution.

The LN samples were prepared by sealing 0.2 g of the hydrophobic silica gel and 0.9 mL of 3.0 M NaCl aqueous solution in a stainless-steel cell with two O-ring equipped pistons, as

depicted in Figure 6.1. The diameter of the piston, *d*, was 19 mm. The length of all the LN samples was the same, indicating that the amount of air in the LN samples was a constant[49].

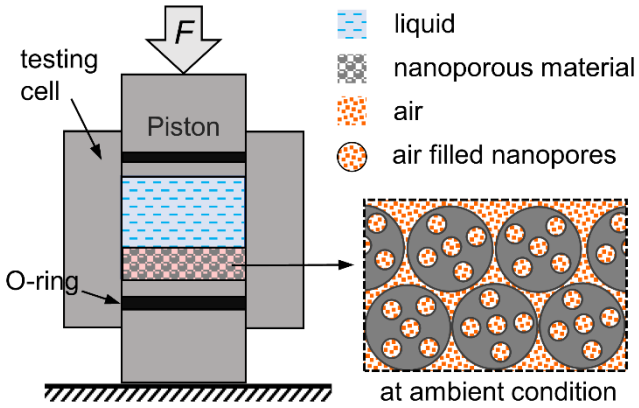

Figure 6.1. Schematic of an LN sample sealed in a testing cell with two pistons.

All experiments were conducted at 35 ºC, in a temperature chamber (Mode 3119-606, Instron). The LN sample sealed in the testing cell was placed on a platen of a universal tester (Mode 5982, Instron). The loading speed of the compression test was 2 mm/min. As the compression progressed, the force *F* increased and the hydrostatic pressure $P = 4F/\pi d^2$ was built up in the testing cell and exerted on the LN sample. As *F* reached the preset peak value F_{max}, the Instron load-cell was moved back at the same speed. When the load-cell returned to its original position, the 1st loading-unloading cycle was completed. This loading-unloading process was consecutively repeated for at least 5 times for each LN sample. The specific volume change of the LN sample was calculated as $V = \delta \cdot \pi d^2/4m$, where δ and m were the measured displacement of the piston and the mass of the nanoporous silica gel, respectively.

To study the time- and pressure- dependence of gas diffusion behavior in the nanoconfined liquid, a peak-pressure-holding test was designed. After the completion of the 1st loading-unloading cycle, the LN sample was compressed to F_{max} at the same loading speed. Then, the LN sample was held at F_{max} for a certain time duration, t_h, before the load-cell was moved back at the same speed in the 2nd cycle. Immediately after the 2nd cycle, a 3rd loading-unloading cycle without

holding was applied to characterize the change in degree of liquid outflow. LN samples with the same composition were held at $F_{max} = 17\ kN$, corresponding to a system peak pressure of 60 MPa, for 1.5 h, 3 h, 6 h, 9 h, 12 h, and 15 h, respectively. To investigate the pressure effect on the gas diffusion behavior, another series of peak-pressure-holding tests were performed at $F_{max} = 43\ kN$, equivalent to a system peak pressure of 150 MPa.

6.3 Results

6.3.1 Pressure-induced liquid infiltration tests ($t_{\mathrm{h}} = 0$)

Figure 6.2 shows typical consecutive loading-unloading cycles of LN sample without peak-pressure-holding process. From the 3rd loading-unloading cycle, the curves are identical to that in the 2nd cycle. For clarity, only the first three consecutive loading-unloading cycles are shown here. At ambient condition, the surface energy barrier of the hydrophobic nanopore surface prevents the liquid flowing into the nanopores and the nanopores are initially filled with air, as illustrated in Figure 6.1. When the system pressure increases, the initial mechanical response of LN system is elastic with a relatively high bulk modulus. As the system pressure reaches a critical value, the system bulk modulus is reduced considerably and a pressure plateau with a large volume change is formed. This dramatic volume change is due to the liquid infiltration into the nanopores. The initial pressure of the plateau, namely the liquid infiltration pressure, is governed by the classic Laplace-Young equation as $P_{in} = \Delta\gamma/d = 19\ MPa$, where $\Delta\gamma$ is the excessive solid-liquid interfacial tension and d is the nanopore diameter. With the increased system pressure, the gas molecules outside the nanopores are fully dissolved by the bulk liquid phase based on the Henry's law, while the gas molecules inside the nanopores are fully dissolved by the confined liquid phase based on the Henry's law and gas oversolubility[44,148,161]. When all the nanopores are filled with liquid, the slope of the loading curve increases to a value slightly higher than its initial bulk

modulus due to the reduced liquid amount outside of the nanopores. The accessible nanopore volume is determined by the width of the pressure plateau W_1 (Figure 6.2). The measured W_1 (0.396±0.004 cm^3/g) is slightly smaller than the nanopore volume measured by gas adsorption analysis, which is due to the van der Waals distance between the liquid molecules and the hydrophobic surface of nanopores.

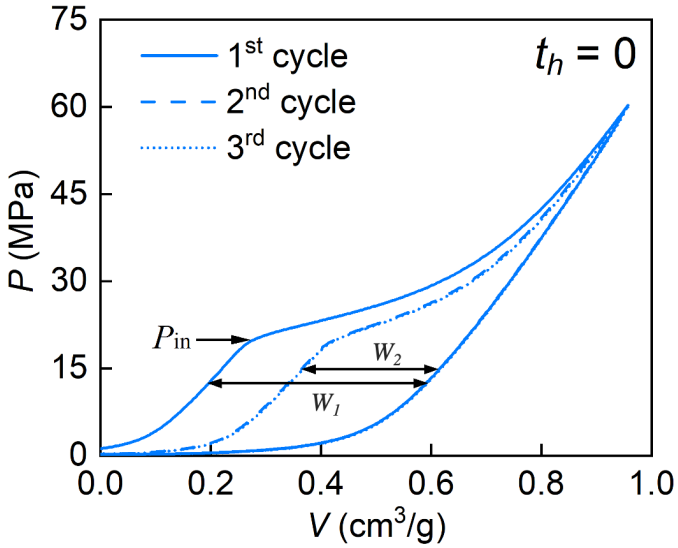

Figure 6.2. Typical consecutive loading-unloading curves of LN sample in pressure-induced liquid infiltration test without peak-pressure-holding process.

Upon unloading, the pressure drops quickly with a slope similar to the initial elastic loading one. As the system pressure decreases to 10 MPa, the slope reduces and forms another pressure plateau, suggesting that the confined liquid as well as the dissolved gas molecules flow out from the hydrophobic nanopores. Simultaneously, with the reduced system pressure and the amount of liquid molecules confined in the nanopores, the gas molecules preserved in the nanopores precipitate out from the nanoconfined liquid and occupy the nanopore volume. The precipitated gas molecules are fully dissolved again when the liquid molecules infiltrate into the nanopores in the next loading process.

In the 2nd cycle, the accessible nanopore volume W_2, is much reduced (Figure 6.2), indicating only part of the intruded liquid flow out of the nanopores during the unloading process in the 1st cycle. The degree of liquid outflow in the N^{th} cycle is determined as W_{N+1}/W_N. As shown in Figure 6.2, the degree of liquid outflow in the 1st cycle is 62.5%. From the 2nd cycle, a 100% liquid outflow suggests that the LN system works as a stable energy absorber under consecutive loading-unloading conditions.

6.3.2 Peak-pressure-holding tests ($t_h > 0$)

To study the unique gas diffusion behavior in the confined nano-environment, LN samples are held at the peak pressure at the end of the 2nd loading process. Figure 6.3a shows the loading-unloading curves of an LN sample with 3h holding time. The 1st cycle and the loading curve of the 2nd cycle are exactly the same as those in liquid infiltration tests without holding time. In the 3rd cycle, the reduction in the plateau width (W_3) indicates a much-reduced degree of liquid outflow during the unloading process of the 2nd cycle. It suggests that around 27% (W_3/W_2) of gas diffused out during the 3 hours holding time. As the holding time increasing, as shown in Figure 6.3b, $W_3^{t_h>0}$ gradually decreases.

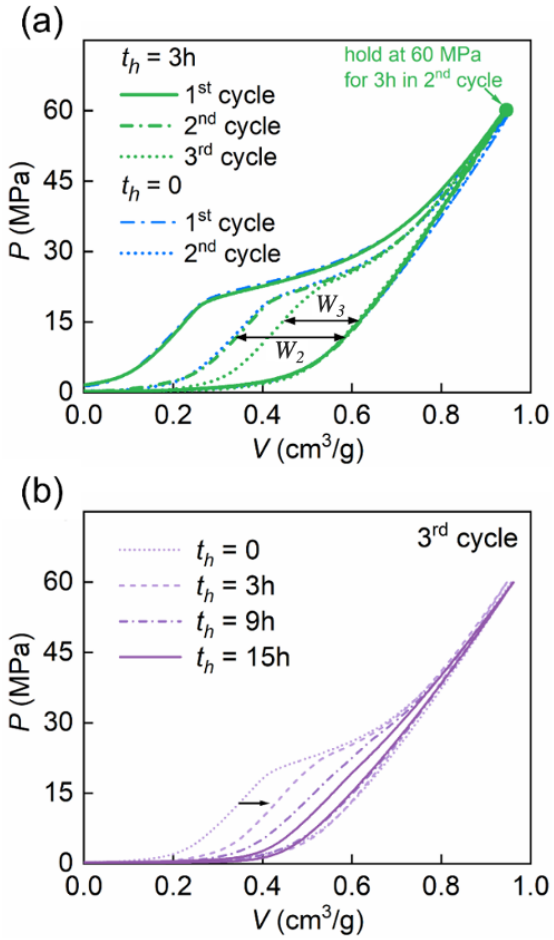

Figure 6.3. Typical loading-unloading curves of (a) an LN sample with 3-hour peak-pressure-holding process and (b) the 3rd loading-unloading cycle of LN samples with various holding time.

6.3.3 Pressure effect on gas diffusion in nanopores

To further study the effect of holding pressure on the behavior of gas diffusion from nanoconfined liquid phase to bulk one, the peak pressure of the infiltration tests is increased from 60 MPa to 150 MPa. Figure 6.4 shows typical loading-unloading curves of 3-hour peak-pressure-holding tests at different peak pressures. As W_2 is insensitive to the pressure increase, the excessive solid-liquid interfacial tension as well as the preserved gas molecules are identical for the LN system and independent to the peak pressure under continuous liquid infiltration testing

cycles. After the peak-pressure-holding process in the 2nd cycle, $W_3^{150\,MPa} < W_3^{60\,MPa}$ demonstrates the promoted gas diffusion rate at higher holding pressure.

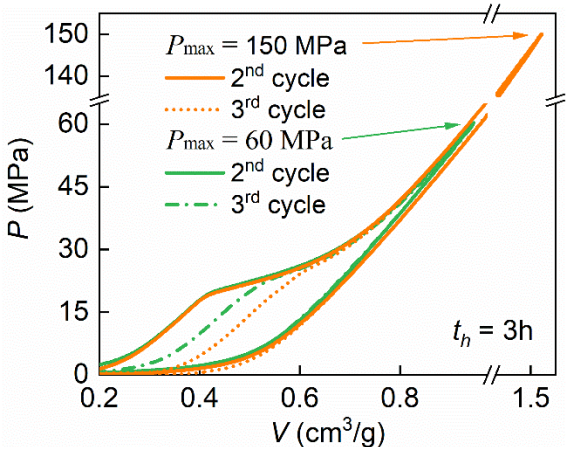

Figure 6.4. Typical loading-unloading curves of LN samples in 3-hour peak-pressure-holding liquid infiltration tests with different peak pressures.

The measured degree of liquid outflow under 60 Mpa and 150 Mpa with different holding durations are illustrated in Table 6.1. It is clear that the degree of outflow decreases as the holding time and holding pressure growing.

Table 6.1. The measured degree of liquid outflow in the 2nd loading-unloading cycle ($W_3^{t_h \geq 0}/W_2$).

Pressure	Holding Time						
	0	1.5 h	3 h	6 h	9 h	12 h	15 h
60 MPa	100 ± 0	77.9 ± 2.4	73.0 ± 3.2	54.1 ± 5.7	36.1 ± 8.7	32.5 ± 5.1	22.9 ± 7.3
150 MPa	100 ± 0	65.1 ± 4.2	44.4 ± 2.5	32.9 ± 2.1	16.8 ± 2.2	15.1 ± 3.1	8.8 ± 7.6

6.4 Discussion

As demonstrated in our previous studies[142,147,161], the liquid outflow from hydrophobic nanopores is dominated by both the excessive solid-liquid interfacial tension and the gas-liquid

interaction in the nanopores during the unloading process. In all the liquid infiltration tests with or without peak-pressure-holding process, the same liquid phase as well as the nanopore surface properties ensure a constant excessive solid-liquid interfacial tension. Thus, the much-reduced degree of liquid outflow is attributed to a time-dependent gas-liquid interaction during the peak-pressure-holding process, which promotes gas to escape from the hydrophobic nanopores.

In the infiltration tests without peak-pressure-holding process ($t_h = 0$), the gas escape includes gas advection and gas diffusion from the nanopores to the bulk liquid during the unloading process. Given the unloading process completes in seconds, the amount of gas diffusion from the nanopores to the bulk liquid (a relatively slow process) can be ignored. The negligible gas diffusion is also validated by the same loading-unloading curves in the 2nd and 3rd cycles in Figure 6.2. Otherwise, a reduced W_3 should be observed. The gas advection describes the dissolved gas flowing out with the liquid and is proportional to the transfer velocity and total gas amount in the nanoconfined liquid. Since the system volume recovery speed (2 mm/min) and the unloading curves of the 2nd and the 3rd cycles are the same, the initial transfer velocity of all LN samples is nearly the same. Therefore, the amount of gas molecules escaped from the nanopores through advection is estimated as

$$n_a = \alpha \cdot n_0 \tag{6.1}$$

where n_0 is the total amount of gas molecules dissolved in the nanoconfined liquid before the onset of unloading process and α is ratio of the advected gas amount to the total gas amount. The amount of gas molecules preserved in the nanopores is

$$n_p^{t_h=0} = (1 - \alpha) \cdot n_0 \tag{6.2}$$

While in the infiltration tests with peak-pressure-holding process ($t_h = 3h$), the gas outflow includes the gas diffusion during the holding process and the gas advection during the

unloading process. The amount of gas diffusion is denoted as n_d. The residue amount of gas molecules before the onset of unloading process is $n_r = n_0 - n_d$. Consequently, the amount of gas molecules preserved in the nanopores is estimated as

$$n_p^{t_h>0} = (1-\alpha) \cdot n_r \tag{6.3}$$

By comparing equations 6.2 and 6.3, the amount of preserved gas molecules in the nanopores is reduced due to the gas diffusion during the peak-pressure-holding process. As the degree of liquid outflow is positively related to the amount of preserved gas molecules in the nanopores[142,161],

$$\frac{n_r}{n_0} = \frac{n_p^{t_h>0}}{n_p^{t_h=0}} \approx \frac{W_3^{t_h>0}}{W_2} \tag{6.4}$$

Please note that n_0 is a constant, as the nanopore volume, peak pressure and initial gas content sealed in the testing cell are all constants for all the LN samples. As shown in Figure 6.3b, $W_3^{t_h>0}$ gradually decreases with increased holding time, which demonstrates the time-dependent gas diffusion process from the nanoconfined liquid phase to the bulk liquid one.

This pressure effect on gas diffusion in nanoconfined liquid is not seen in bulk liquid. In continuous theory, as described by the Fick's second law, the diffusion rate is proportional to the diffusivity and the curvature of concentration profile. According to the Wilke-Chang equation[34], diffusivity is related to the density, molecular weight, and viscosity of the solvent, all of which are insensitive to pressure change. Therefore, the pressure effect on gas diffusion in bulk liquid is negligible, which has also been demonstrated by both experimental and numerical studies[29,162].

Given the diffusion path in the nanoporous particles and the initial gas concentration are the same for all LN samples before the onset of peak-pressure-holding, the pressure effect on gas diffusion is due to the enhanced diffusivity in the nano-environment. The enhanced diffusivity is

attributed to the allocation of liquid and dissolved gas molecules in the hydrophobic nanopores. Under the hydrophobic nanoconfinement, gas molecules tend to be co-adsorbed with liquid molecules on the hydrophobic nanopore wall[77]. As a result, the gas molecules are enriched in the adsorption layer, leading to the oversolubility of gas molecules[45,46], which is much higher than the gas solubility around the center of the nanopores or in the bulk liquid phase (the green profile in Figure 6.5). This oversolubility endows the adsorption layer to uptake more gas molecules than the nanopore center. In addition, as the system pressure increases, the spacing between the gas molecules is reduced and the system free energy is enhanced. The accumulation of gas molecules in the adsorption layer is energetically favorable and further promoted. Consequently, the gas concentration near the nanopore wall increases with the applied pressure, while the gas concentration at the nanopore center and in the bulk liquid phase is insensitive to the pressure increase (the red profile in Figure 6.5). This pressure-dependent gas concentration gradient between the adsorption layer in the hydrophobic nanopores and the bulk liquid phase leads to a higher gas diffusion rate.

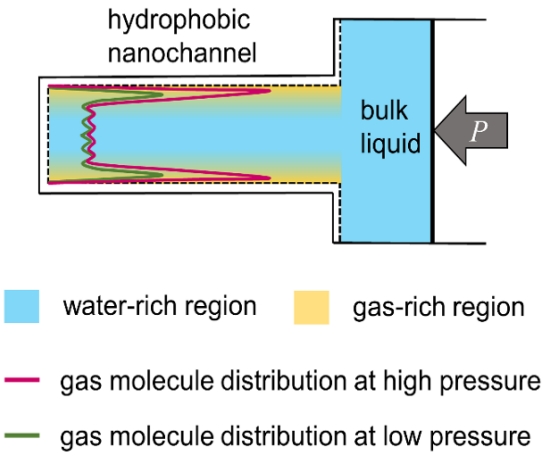

Figure 6.5. Schematic of the pressure effect on dissolved gas diffusion from hydrophobic nanopore to bulk liquid.

Since n_0 is a constant, the gas diffusion during peak-pressure-holding process can be simplified as the drive-in deposition. The concentration of gas molecules in this type of diffusion is decaying exponentially[163]. Therefore, to model the residue gas amount in the nanopores, exponential decay is applied as

$$\frac{n_r - n_\infty}{n_0 - n_\infty} = \exp\left(-\frac{t}{\tau}\right) \tag{6.5}$$

where n_∞ is the residue gas amount in the hydrophobic nanopores after infinite holding process and τ is a constant.

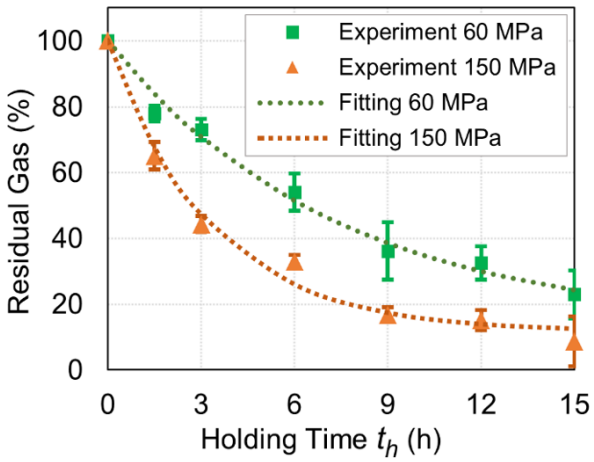

Figure 6.6. The preserved gas in the hydrophobic nanopores.

As the experimental results cannot quantify the distribution of gas molecules along the nanopore depth, this simplified model is only capable of estimating the total amount of gas retained in and flew out from the nanopores. Table 6.1 summarizes the experimental measurement of the degree of liquid outflow. Figure 6.6 shows the residue gas in the nanopores as a function of time under different peak pressures.

Table 6.2. The parameters in the exponential decay model.

Pressure	n_∞/n_0 (%)	τ (h)	R^2
60 MPa	13.0	7.4	98.7 %
150 MPa	11.5	3.3	98.8 %

By fitting the experimental data, the parameters used in equation 6.5 are listed in Table 6.2. The residue gas amount shows a clear exponential decay trend. The time constant τ under 150 MPa is 3.3 h and much smaller than that under 60 MPa, indicating an enhanced gas diffusion rate under high pressure. The amount of residue gas in the nanopores after infinite diffusion time converges to a smaller value when the holding pressure is higher. This is attributed to the higher gas solubility of the bulk liquid phase under higher pressure, which facilitates the gas diffusion from the nanoconfined liquid phase to the bulk one. Both τ and n_∞ reveal that the rate of dissolved gas diffusion out from hydrophobic nanopores is promoted by pressure.

6.5 Conclusion

In this work, we have investigated the dissolved gas diffusion from hydrophobic nanopores to bulk liquid in a LN system by experimentally quantify the change in degree of liquid outflow. It has been found that as the holding time increases, the gas diffusion progress exhibits an exponentially decaying rate. In contrast to continuous theories, pressure has a prominent effect on the nanoscale gas diffusion. As pressure increases, the gas diffusion process from the nanoconfined liquid to the bulk liquid is significantly promoted. The pressure effect is related to the gas oversolubility and uneven distribution of gas and liquid molecules caused by the hydrophobic nanoconfinement. These findings extend the knowledge of the dissolved gas diffusion in a nano-environment and will guide the future design of CO_2 sequestration and shale gas extraction systems.

Chapter 7. FUTURE STUDY

7.1 Effect of Gas Species on GLIHNE

The gas phase in LN systems used in this thesis is air as no special treatment is needed. However, mixture compounds in air are not ideal to evaluate the gas phase effect. In addition, the gas solubility in bulk liquid phase as well as the oversolubility in HNE are highly dependent on gas species. Based on Henry's law, the gas solubility of different gas species in bulk water can be calculated, as shown in Table 7.1. The gas solubility of carbon dioxide in bulk water is almost 45 times higher than that of air, while the gas solubility of helium is only half of the air. The degree of liquid outflow of LN systems will be affected by the selection of gas species, which will further quantify the effect of bulk gas solubility and oversolubility on GLIHNE.

Table 7.1. Bulk phase gas solubility for different gas species in deionized water at 25°C.

Gas Species	Gas solubility in deionized water (10^{-3} mol/L)
He	0.370
Air	0.763
CO_2	34.002

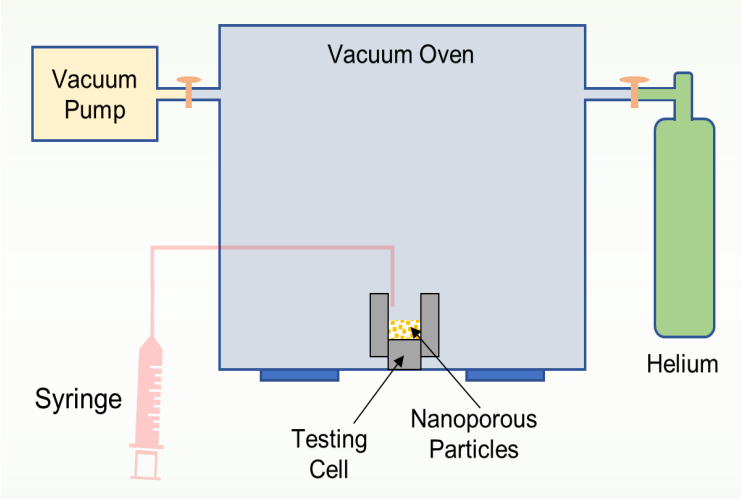

Figure 7.1. Experimental setup of replacing air in nano-channels with helium.

In order to replace the air trapped in the nanopores and the bulk liquid phase by other gas species, gas exchange processes will be implemented before liquid infiltration tests. As shown in Figure 7.1, a thin layer of nanoporous particles will be placed in a vacuum chamber. After degassing for 24h, selected gas will be fed into the vacuum chamber to fill the nanopores.

Next, a certain amount of DI water will be filled into the testing cell by a syringe connected to the vacuum chamber. The filled DI water will be degassed in the vacuum chamber for another 24h at an elevated temperature. After the completion of degassing, the same selected gas will be fed into the vacuum chamber again to saturate the bulk liquid phase. The LN sample will be cooled down to room temperature in the selected gas environment before testing.

7.2 Temperature Effect on Gas Diffusion from HNE to Bulk Liquid Phase

In Chapter 3, we have shown that temperature can promote liquid outflow in each infiltration step in the LN system. This trend is also found without separating the infiltration plateau, as shown in Figure 7.2. By increasing temperature, both the liquid outflow pressure and the width of the second infiltration plateau increased. It suggests that the gas molecules are more likely to stay in nano-channels at elevated temperatures, which leads to a higher degree of liquid outflow.

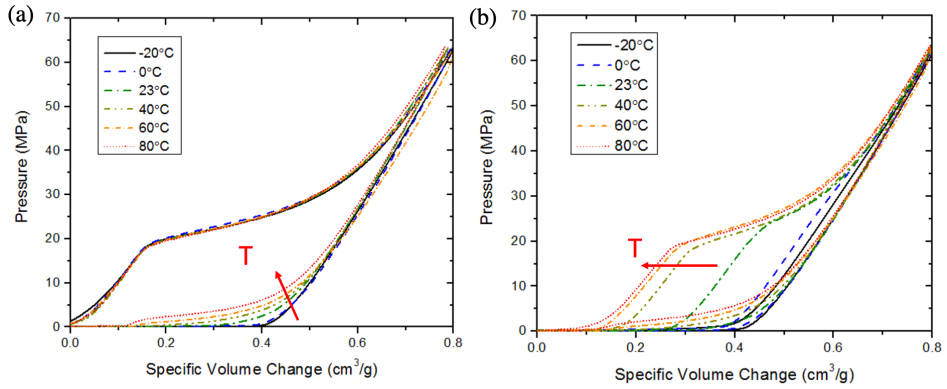

Figure 7.2. Temperature effect on liquid outflow in (a) the 1st and (b) the 2nd loading-unloading cycles.

Based on Henry's law and van ´t Hoff equation (equation 4.2), the gas solubility in bulk liquid phase is reduced by elevated temperature as shown in Figure 7.3. The temperature-elevated internal energy of the LN system facilitates the GLIHNE. Therefore, during unloading, the dissolved gas molecules are much easier to return to gas phase in system with a higher temperature. Moreover, due to oversolubility, the enlarged volume by gas phase in nano-channels is much more than that in bulk phase, leading to liquid outflow at a higher pressure (Figure 7.2). This elevated outflow pressure is able to induce more liquid outflow. However, when the temperature keeps increasing, its effect on liquid outflow is weaker (Figure 7.3).

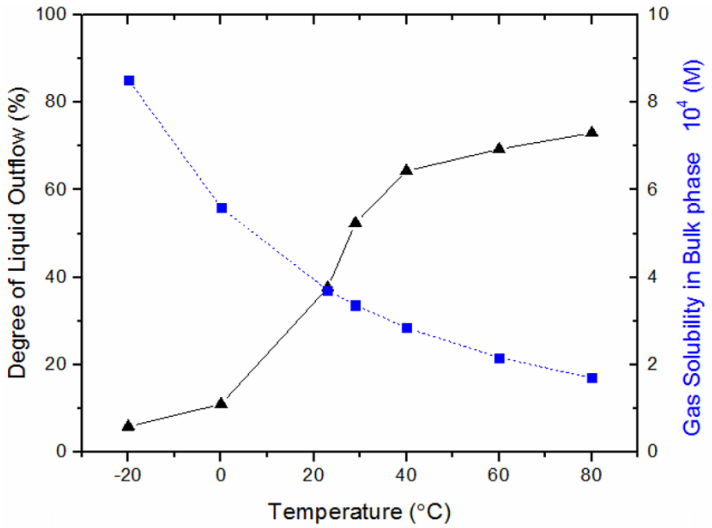

Figure 7.3. Temperature effect on bulk gas solubility and degree of liquid outflow.

Moreover, the temperature effect on gas diffusion from HNE to bulk liquid phase was also studied. Two LN systems with the same components were compressed under the same pressure at different temperatures for the same period of time. The results show that the residual gas amount in the LN system decreased more by holding the system with higher temperature (Figure 7.4). Since temperature can facilitate the internal energy of the LN system, which increases the kinetic energy of gas molecules, thus accelerates the gas diffusion process from HNE to bulk liquid phase.

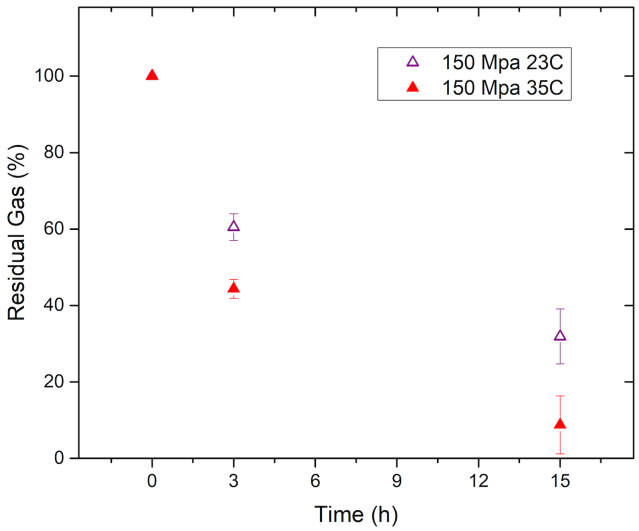

Figure 7.4. Temperature effect on the residual gas in the hydrophobic nanopores.

APPENDIX

APPENDIX

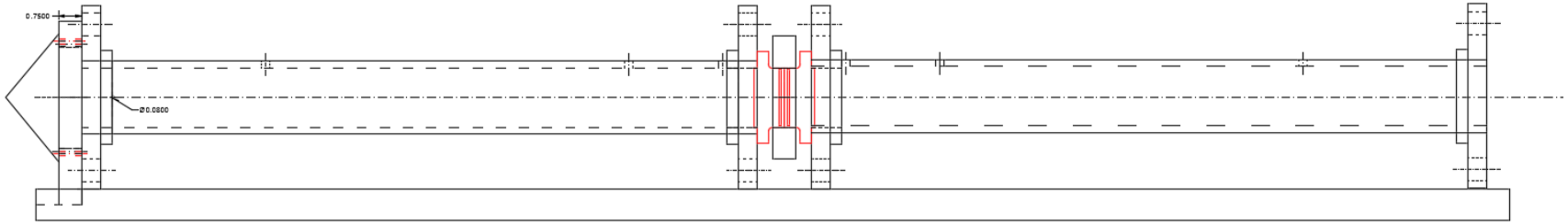

Figure A-1. Acoustic Impedance Tube – Assembly Drawing.

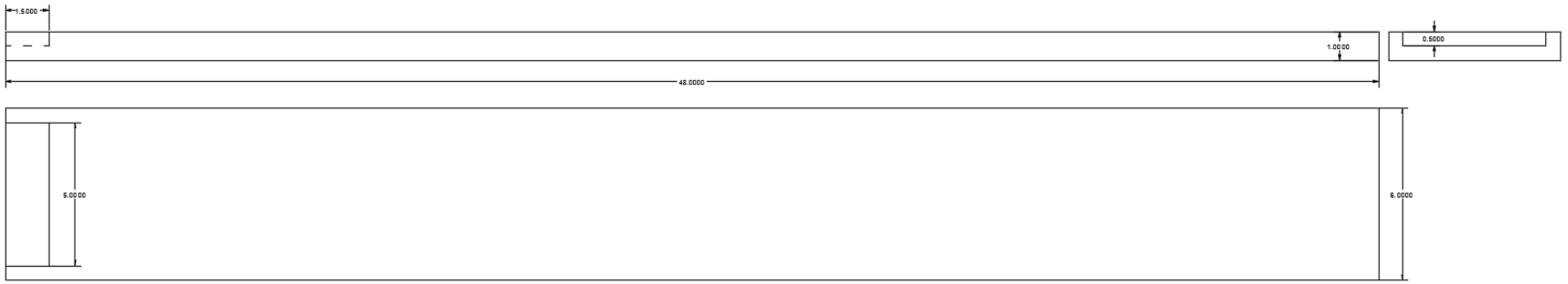

Name	Base	Unit	Inch	Designed by	Lijiang Xu
Material	Polyethylene Sheets	Quantity	1	Civil and Environmental Engineering of Michigan State University	

Figure A-2. Acoustic Impedance Tube – Base.

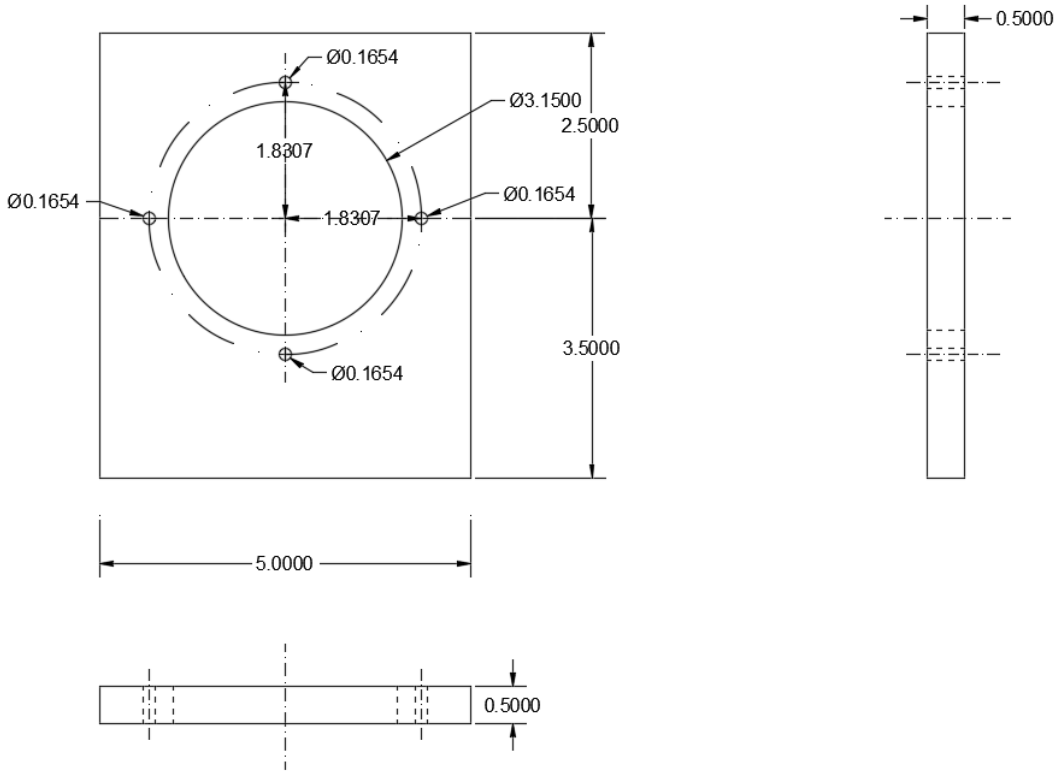

Name	High Frequency Speaker Plate	Unit	Inch	Designed by	Lijiang Xu
Material	304 Stainless Steel Sheet	Quantity	1	Civil and Environmental Engineering of Michigan State University	

Figure A-3. Acoustic Impedance Tube – High Frequency Speaker Plate Support.

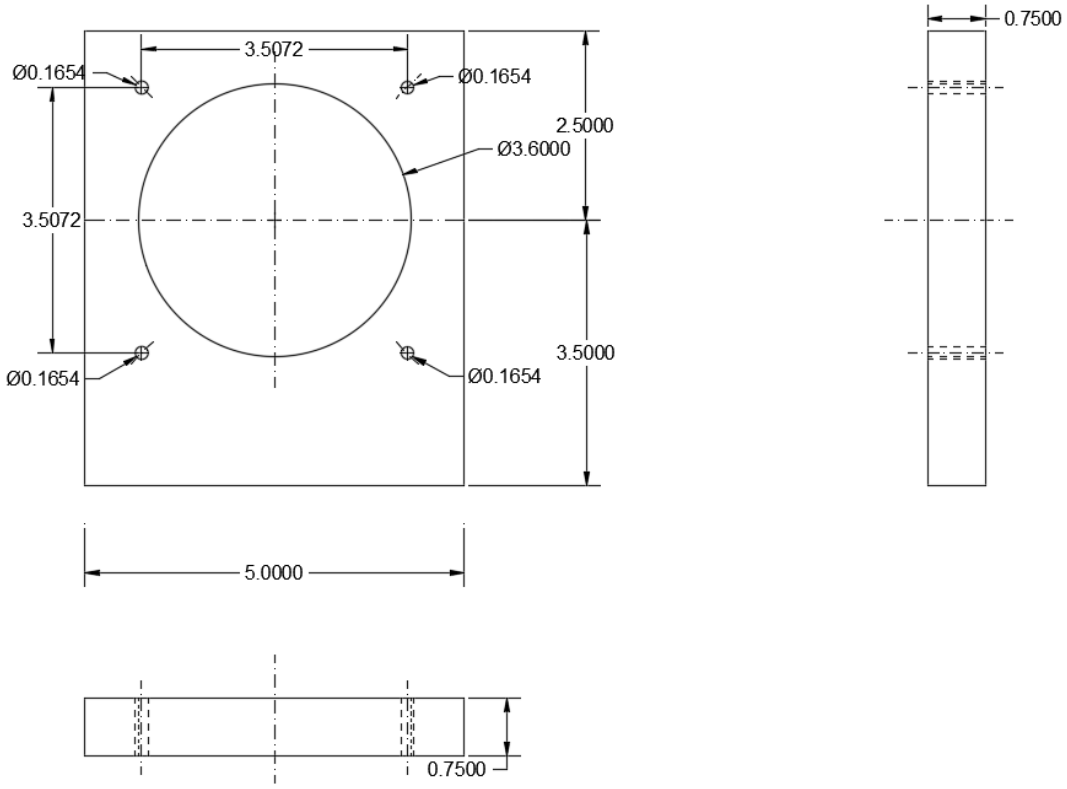

Name	Low Frequency Speaker Plate	Unit	Inch	Designed by	Lijiang Xu
Material	304 Stainless Steel Sheet	Quantity	1	Civil and Environmental Engineering of Michigan State University	

Figure A-4. Acoustic Impedance Tube – Low Frequency Speaker Plate Support.

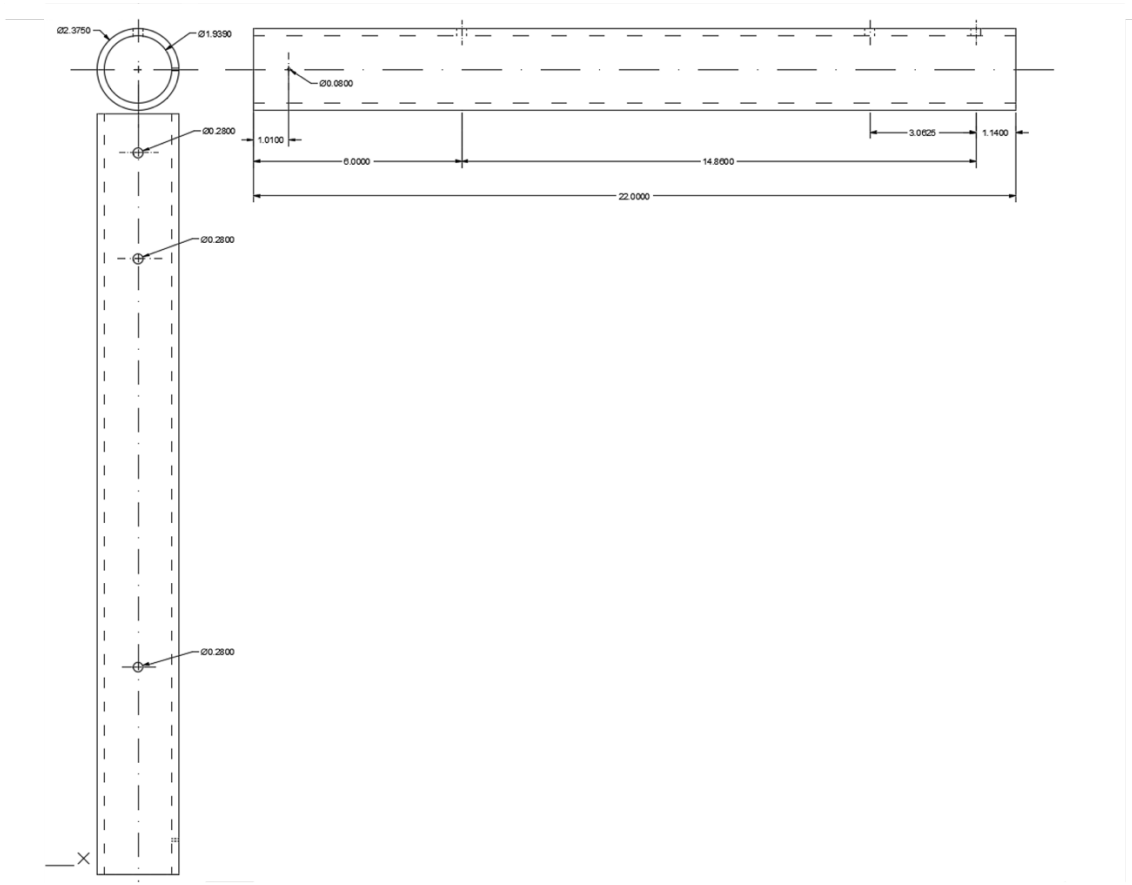

Name	Tube	Unit	Inch	Designed by	Lijiang Xu
Material	304 Stainless Steel Pipe	Quantity	2	Civil and Environmental Engineering of Michigan State University	
Note: Both ends need to be threaded to fit in 4.25in flanges					

Figure A-5. Acoustic Impedance Tube – Tube.

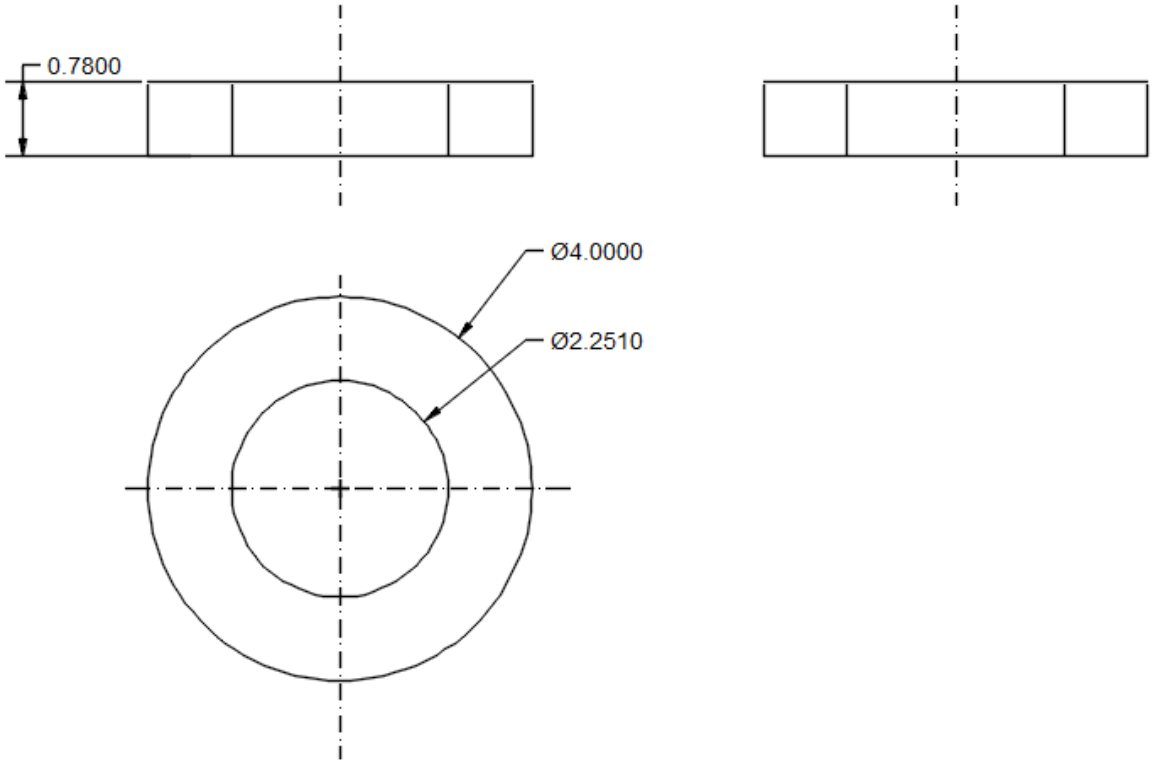

Name	Cell	Unit	Inch	Designed by	Lijiang Xu
Material	Acrylic	Quantity	1	Civil and Environmental Engineering of Michigan State University	

Figure A-6. Acoustic Impedance Tube – Acrylic Cell.

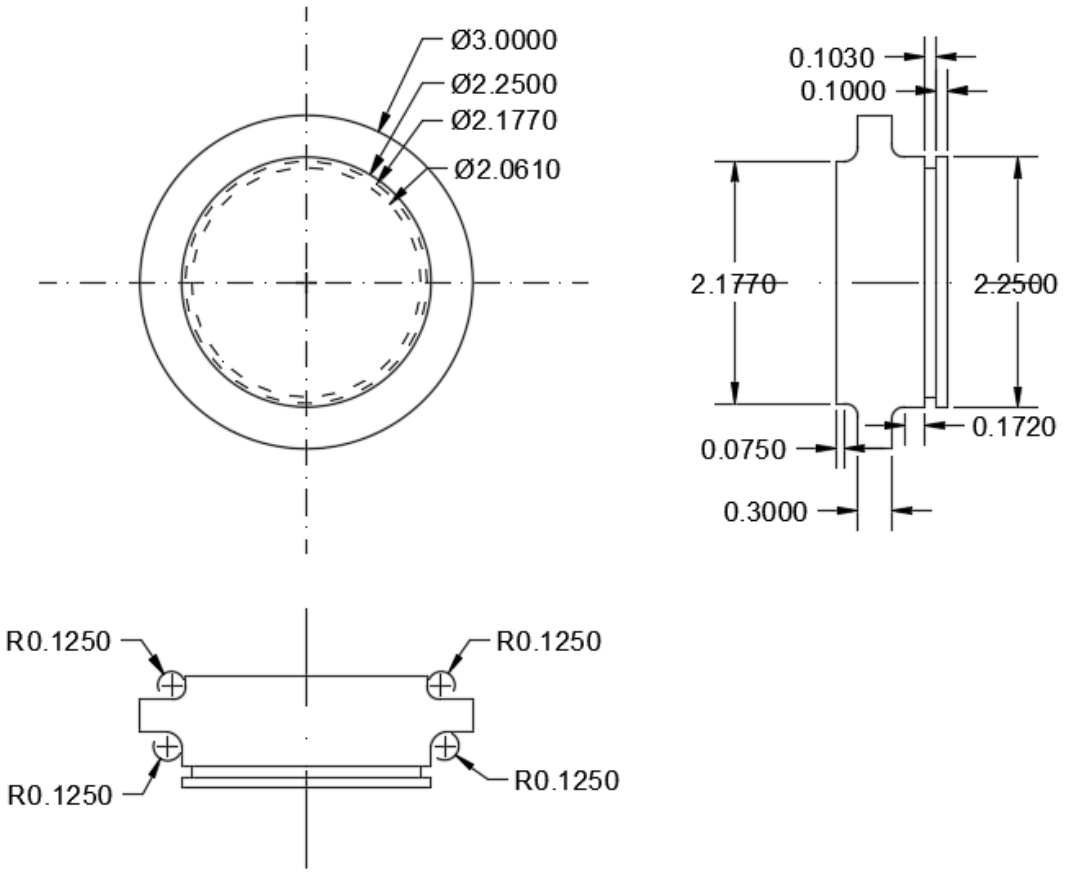

Name	Piston	Unit	Inch	Designed by	Lijiang Xu
Material	Clear Gray Polycarbonate	Quantity	2	Civil and Environmental Engineering of Michigan State University	

Figure A-7. Acoustic Impedance Tube – Polycarbonate Piston.

BIBLIOGRAPHY

BIBLIOGRAPHY

1. Hoel, M. & Kverndokk, S. Depletion of fossil fuels and the impacts of global warming. *Resour. energy Econ.* **18**, 115–136 (1996).

2. Höök, M. & Tang, X. Depletion of fossil fuels and anthropogenic climate change—A review. *Energy Policy* **52**, 797–809 (2013).

3. Shaffer, G., Olsen, S. M. & Pedersen, J. O. P. Long-term ocean oxygen depletion in response to carbon dioxide emissions from fossil fuels. *Nat. Geosci.* **2**, 105–109 (2009).

4. Bolaji, B. O. & Huan, Z. Ozone depletion and global warming: Case for the use of natural refrigerant--a review. *Renew. Sustain. Energy Rev.* **18**, 49–54 (2013).

5. Gao, J. & You, F. Design and optimization of shale gas energy systems: Overview, research challenges, and future directions. *Comput. Chem. Eng.* **106**, 699–718 (2017).

6. Melikoglu, M. Shale gas: Analysis of its role in the global energy market. *Renew. Sustain. Energy Rev.* **37**, 460–468 (2014).

7. Wilberforce, T. *et al.* A comprehensive study of the effect of bipolar plate (BP) geometry design on the performance of proton exchange membrane (PEM) fuel cells. *Renew. Sustain. Energy Rev.* **111**, 236–260 (2019).

8. Barbir, F. & Gomez, T. Efficiency and economics of proton exchange membrane (PEM) fuel cells. *Int. J. Hydrogen Energy* **21**, 891–901 (1996).

9. Lackner, K. S. A guide to CO2 sequestration. *Science (80-.).* **300**, 1677–1678 (2003).

10. Lal, R. Carbon sequestration. *Philos. Trans. R. Soc. B Biol. Sci.* **363**, 815–830 (2008).

11. Bazylak, A. Liquid water visualization in PEM fuel cells: A review. *Int. J. Hydrogen Energy* **34**, 3845–3857 (2009).

12. Anderson, R. *et al.* A critical review of two-phase flow in gas flow channels of proton exchange membrane fuel cells. *J. Power Sources* **195**, 4531–4553 (2010).

13. Kannan, A. M. & Munukutla, L. Carbon nano-chain and carbon nano-fibers based gas diffusion layers for proton exchange membrane fuel cells. *J. Power Sources* **167**, 330–335 (2007).

14. Joo, J. *et al.* Controlled water flooding of polymer electrolyte fuel cells applying superhydrophobic gas diffusion layer. *Curr. Appl. Phys.* **14**, 1374–1379 (2014).

15. Weber, A. Z. & Newman, J. Effects of membrane-and catalyst-layer-thickness nonuniformities in polymer-electrolyte fuel cells. *J. Electrochem. Soc.* **154**, B405 (2007).

16. Ho, T. A., Wang, Y., Xiong, Y. & Criscenti, L. J. Differential retention and release of CO2 and CH4 in kerogen nanopores: Implications for gas extraction and carbon sequestration. *Fuel* **220**, 1–7 (2018).

17. Guo, C., Xu, J., Wu, K., Wei, M. & Liu, S. Study on gas flow through nano pores of shale gas reservoirs. *Fuel* **143**, 107–117 (2015).

18. Striolo, A. & Cole, D. R. Understanding shale gas: Recent progress and remaining challenges. *Energy & Fuels* **31**, 10300–10310 (2017).

19. Blyverket, J. Molecular Dynamics Modeling of Clay-Fluid Interfaces. (2015).

20. Cygan, R. T., Romanov, V. N. & Myshakin, E. M. Molecular simulation of carbon dioxide capture by montmorillonite using an accurate and flexible force field. *J. Phys. Chem. C* **116**, 13079–13091 (2012).

21. Psarras, P., Holmes, R., Vishal, V. & Wilcox, J. Methane and CO2 adsorption capacities of kerogen in the Eagle Ford shale from molecular simulation. *Acc. Chem. Res.* **50**, 1818–1828 (2017).

22. Zhang, M., Zhan, S. & Jin, Z. Recovery mechanisms of hydrocarbon mixtures in organic and inorganic nanopores during pressure drawdown and CO2 injection from molecular perspectives. *Chem. Eng. J.* **382**, 122808 (2020).

23. Xu, H. Y. *et al.* Two-Phase Transport Characteristic of Shale Gas and Water through Hydrophilic and Hydrophobic Nanopores. *Energy and Fuels* **34**, 4407–4420 (2020).

24. Sun, Z., Shi, J., Wu, K. & Li, X. Gas Flow Behavior through Inorganic Nanopores in Shale Considering Confinement Effect and Moisture Content. *Ind. Eng. Chem. Res.* **57**, 3430–3440 (2018).

25. Board, O. S., of Sciences Engineering, Medicine & others. *Negative emissions technologies and reliable sequestration: A research agenda*. (National Academies Press, 2019).

26. Qiao, Y., Cao, G. & Chen, X. Effects of gas molecules on nanofluidic behaviors. *J. Am. Chem. Soc.* **129**, 2355–2359 (2007).

27. Akgerman, A. & Gainer, J. L. Diffusion of Gases in Liquids. *Ind. Eng. Chem. Fundam.* **11**, 373–379 (1972).

28. Reid, R. C., Prausnitz, J. M. & Poling, B. E. The properties of gases and liquids. (1987).

29. Cadogan, S. P., Maitland, G. C. & Trusler, J. P. M. Diffusion coefficients of CO2 and N2 in water at temperatures between 298.15 K and 423.15 K at pressures up to 45 MPa. *J. Chem. Eng. Data* **59**, 519–525 (2014).

30. Starr, F. W., Harrington, S., Sciortino, F. & Stanley, H. E. Dynamics of simulated water under pressure. *Phys. Rev. Lett.* **82**, 3629–3632 (1999).

31. Lu, W., Guo, H., Chou, I. M., Burruss, R. C. & Li, L. Determination of diffusion coefficients of carbon dioxide in water between 268 and 473K in a high-pressure capillary optical cell with in situ Raman spectroscopic measurements. *Geochim. Cosmochim. Acta* **115**, 183–204 (2013).

32. Sell, A., Fadaei, H., Kim, M. & Sinton, D. Measurement of CO2 diffusivity for carbon sequestration: A microfluidic approach for reservoir-specific analysis. *Environ. Sci. Technol.* **47**, 71–78 (2013).

33. K. Hijikata, S. H. K. O. H. Y. H. . I. Y. T. K. Measurement of CO2 Diffuison Coefficient and Application of LIF in Pressurized Water. **22**, 5 (1995).

34. Wilke, C. R. & Chang, P. Correlation of diffusion coefficients in dilute solutions. *AIChE J.* **1**, 264–270 (1955).

35. Clever, H. L. & Holland, C. J. Solubility of argon gas in aqueous alkali halide solutions. Temperature coefficient of the salting out parameter. *J. Chem. Eng. Data* **13**, 411–414 (1968).

36. Lei, Z., Dai, C. & Chen, B. Gas Solubility in Ionic Liquids. *Chem. Rev.* **114**, 1289–1326 (2014).

37. Liu, Y., Hou, M., Yang, G. & Han, B. Solubility of CO2in aqueous solutions of NaCl, KCl, CaCl2and their mixed salts at different temperatures and pressures. *J. Supercrit. Fluids* **56**, 125–129 (2011).

38. Crupi, V., Majolino, D., Migliardo, P., Venuti, V. & Bellissent-Funel, M. C. Structure and dynamics of water confined in a nanoporous sol-gel silica glass: a neutron scattering study. *Mol. Phys.* **101**, 3323–3333 (2003).

39. Gelb, L. D., Gubbins, K. E., Radhakrishnan, R. & Sliwinska-Bartkowiak, M. Phase separation in confined systems. *Reports Prog. Phys.* **62**, 1573 (1999).

40. Smirnov, P., Yamaguchi, T., Kittaka, S., Takahara, S. & Kuroda, Y. X-ray diffraction study of water confined in mesoporous MCM-41 materials over a temperature range of 223- 298 K. *J. Phys. Chem. B* **104**, 5498–5504 (2000).

41. Baugh, J., Kleinhammes, A., Han, D., Wang, Q. & Wu, Y. Confinement effect on dipole-dipole interactions in nanofluids. *Science (80-.).* **294**, 1505–1507 (2001).

42. Mattea, C., Kimmich, R., Ardelean, I., Wonorahardjo, S. & Farrher, G. Molecular exchange dynamics in partially filled microscale and nanoscale pores of silica glasses studied by field-cycling nuclear magnetic resonance relaxometry. *J. Chem. Phys.* **121**, 10648–10656 (2004).

43. Miachon, S. *et al.* Higher gas solubility in nanoliquids? *ChemPhysChem* **9**, 78–82 (2008).

44. Ho, L. N., Schuurman, Y., Farrusseng, D. & Coasne, B. Solubility of Gases in Water Confined in Nanoporous Materials: ZSM-5, MCM-41, and MIL-100. *J. Phys. Chem. C* **119**, 21547–21554 (2015).

45. Li, W., Nan, Y., Zhang, Z., You, Q. & Jin, Z. Hydrophilicity/Hydrophobicity Driven CO2 Solubility in Kaolinite Nanopores in Relation to Carbon Sequestration. *Chem. Eng. J.* **398**, 125449 (2020).

46. Luzar, A. & Bratko, D. Gas solubility in hydrophobic confinement. *J. Phys. Chem. B* **109**, 22545–22552 (2005).

47. Clauzier, S., Ho, L. N., Pera-Titus, M., Coasne, B. & Farrusseng, D. Enhanced H2 uptake in solvents confined in mesoporous metal-organic framework. *J. Am. Chem. Soc.* **134**, 17369–17371 (2012).

48. Rakotovao, V., Ammar, R., Miachon, S. & Pera-Titus, M. Influence of the mesoconfining solid on gas oversolubility in nanoliquids. *Chem. Phys. Lett.* **485**, 299–303 (2010).

49. Giovambattista, N., Rossky, P. J. & Debenedetti, P. G. Effect of pressure on the phase behavior and structure of water confined between nanoscale hydrophobic and hydrophilic plates. *Phys. Rev. E - Stat. Nonlinear, Soft Matter Phys.* **73**, 1–14 (2006).

50. Beckstein, O. & Sansom, M. S. P. Liquid-vapor oscillations of water in hydrophobic nanopores. *Proc. Natl. Acad. Sci. U. S. A.* **100**, 7063–7068 (2003).

51. Striolo, A., Gubbins, K. E., Chialvo, A. A. & Cummings, P. T. Simulated water adsorption isotherms in carbon nanopores. *Mol. Phys.* **102**, 243–251 (2004).

52. Thommes, M., Morell, J., Cychosz, K. A. & Fröba, M. Combining nitrogen, argon, and water adsorption for advanced characterization of ordered mesoporous carbons (CMKs) and periodic mesoporous organosilicas (PMOs). *Langmuir* **29**, 14893–14902 (2013).

53. Desbiens, N. *et al.* Water condensation in hydrophobic nanopores. *Angew. Chemie - Int. Ed.* **44**, 5310–5313 (2005).

54. Cailliez, F., Boutin, A., Demachy, I. & Fuchs, A. H. Thermodynamic study of water confinement in hydrophobic zeolites by Monte Carlo simulations. *Mol. Simul.* **35**, 24–30 (2009).

55. Moultos, O. A., Tsimpanogiannis, I. N., Panagiotopoulos, A. Z. & Economou, I. G. Atomistic molecular dynamics simulations of CO2 diffusivity in H2O for a wide range of temperatures and pressures. *J. Phys. Chem. B* **118**, 5532–5541 (2014).

56. Curtis, J. B. Fractured shale-gas systems. *Am. Assoc. Pet. Geol. Bull.* **86**, 1921–1938 (2002).

57. Shao, H., Ray, J. R. & Jun, Y.-S. Dissolution and precipitation of clay minerals under geologic CO2 sequestration conditions: CO2- brine- phlogopite interactions. *Environ. Sci. Technol.* **44**, 5999–6005 (2010).

58. Papavasileiou, K. D. *et al.* Molecular dynamics simulation of water-based fracturing fluids in kaolinite slit pores. *J. Phys. Chem. C* **122**, 17170–17183 (2018).

59. Eberle, A. P. R. *et al.* Direct measure of the dense methane phase in gas shale organic porosity by neutron scattering. *Energy & Fuels* **30**, 9022–9027 (2016).

60. Yang, F., Xie, C., Ning, Z. & Krooss, B. M. High-pressure methane sorption on dry and moisture-equilibrated shales. *Energy & Fuels* **31**, 482–492 (2017).

61. Zhang, H. & Cao, D. Molecular simulation of displacement of shale gas by carbon dioxide at different geological depths. *Chem. Eng. Sci.* **156**, 121–127 (2016).

62. Tang, X., Ripepi, N., Stadie, N. P. & Yu, L. Thermodynamic analysis of high pressure methane adsorption in Longmaxi shale. *Fuel* **193**, 411–418 (2017).

63. Uskokovic, V. Challenges for the modern science in its descend towards nano scale. *Curr. Nanosci.* **5**, 372–389 (2009).

64. Surani, F. B. & Qiao, Y. Infiltration and defiltration of an electrolyte solution in nanopores. *J. Appl. Phys.* **100**, 1–5 (2006).

65. Lu, W., Kim, T., Punyamurtula, V. K., Han, A. & Qiao, Y. Effects of addition of potassium chloride and ethylene glycol on nanofluidic behaviors. *J. Mater. Sci.* **46**, 4053–4057 (2011).

66. Gao, Y., Li, M., Zhang, Y., Lu, W. & Xu, B. Spontaneous outflow efficiency of confined liquid in hydrophobic nanopores. *Proc. Natl. Acad. Sci.* **117**, 25246–25253 (2020).

67. Liu, L. Nanofluidics: Fundamentals and applications in energy conversion. (Columbia University, 2010).

68. Zhang, Y., Li, M., Gao, Y., Xu, B. & Lu, W. Compressing liquid nanofoam systems: Liquid infiltration or nanopore deformation? *Nanoscale* **10**, 18444–18450 (2018).

69. Lu, W., Han, A., Kim, T., Chow, B. J. & Qiao, Y. Endcapping treatment of inner surfaces of a hexagonal mesoporous silica. *J. Adhes. Sci. Technol.* **26**, 2135–2141 (2012).

70. Fadeev, A. & Eroshenko, V. Study of Penetration of Water into Hydrophobized Porous Silicas. *J. Colloid Interface Sci.* **187**, 275–82 (1997).

71. Fadeev, A. Y. & Staroverov, S. M. Geometric structural properties of bonded layers of chemically modified silicas. *J. Chromatogr. A* **447**, 103–116 (1988).

72. Young, T. III. An essay on the cohesion of fluids. *Philos. Trans. R. Soc. London* 65–87 (1805).

73. Hummer, G., Rasaiah, J. C. & Noworyta, J. P. Water conduction through the hydrophobic channel of a carbon nanotube. *Nature* **414**, 188–190 (2001).

74. Holt, J. K. *et al.* Fast Mass Transport Through Sub – 2-Nanometer Carbon Nanotubes. **312**, 1034–1038 (2006).

75. Lefevre, B. *et al.* Intrusion and extrusion of water in hydrophobic mesopores. *J. Chem. Phys.* **120**, 4927–4938 (2004).

76. Li, M., Xu, L. & Lu, W. Nanopore size effect on critical infiltration depth of liquid nanofoam as a reusable energy absorber. *J. Appl. Phys.* **125**, 44303 (2019).

77. Ho, L. N., Clauzier, S., Schuurman, Y., Farrusseng, D. & Coasne, B. Gas uptake in solvents confined in mesopores: Adsorption versus enhanced solubility. *J. Phys. Chem. Lett.* **4**, 2274–2278 (2013).

78. Bianco, A., Kostarelos, K. & Prato, M. Applications of carbon nanotubes in drug delivery. *Curr. Opin. Chem. Biol.* **9**, 674–679 (2005).

79. Chen, P. *et al.* Probing single DNA molecule transport using fabricated nanopores. *Nano Lett.* **4**, 2293–2298 (2004).

80. Vairavapandian, D., Vichchulada, P. & Lay, M. D. Preparation and modification of carbon nanotubes: Review of recent advances and applications in catalysis and sensing. *Anal. Chim. Acta* **626**, 119–129 (2008).

81. Eroshenko, V., Regis, R.-C., Soulard, M. & Patarin, J. Energetics: a new field of applications for hydrophobic zeolites. *J. Am. Chem. Soc.* **123**, 8129–8130 (2001).

82. Gusev, A. A. & Guseva, O. Rapid mass transport in mixed matrix nanotube/polymer membranes. *Adv. Mater.* **19**, 2672–2676 (2007).

83. Liu, L., Chen, X., Lu, W., Han, A. & Qiao, Y. Infiltration of electrolytes in molecular-sized nanopores. *Phys. Rev. Lett.* **102**, 1–4 (2009).

84. Ganjiani, S. H. & Hossein Nezhad, A. Molecular Dynamics Simulation of the Effects of the Carbon–Water Interaction Parameters on the Nanofluidic Energy Absorption System. *J. Phys. Chem. C* **120**, 11864–11870 (2016).

85. Liu, H. & Cao, G. Reusable Energy Absorption Performance Based on Nanofluidic Systems. *J. Phys. Chem. C* **120**, 5213–5220 (2016).

86. Li, M. & Lu, W. Adaptive liquid flow behavior in 3D nanopores. *Phys. Chem. Chem. Phys.* **19**, 17167–17172 (2017).

87. Li, M. & Lu, W. Liquid marble: A novel liquid nanofoam structure for energy absorption. *AIP Adv.* **7**, 055312 (2017).

88. Li, M., Li, J., Barbat, S., Baccouche, R. & Lu, W. Enhanced filler-tube wall interaction in liquid nanofoam-filled thin-walled tubes. *Compos. Struct.* **200**, 120–126 (2018).

89. Sun, Y., Lu, W. & Li, Y. A defiltration control method of pressurized liquid in zeolite ZSM-5 by silanol introduction. *Appl. Phys. Lett.* **105**, 15–18 (2014).

90. Han, A. & Qiao, Y. Effects of gas-solid reaction on liquid defiltration in a MCM-41. *Chem. Eng. J.* **141**, 379–382 (2008).

91. Han, A. & Qiao, Y. Influence of surface treatment on defiltration of confined liquid in MCM-41. *Chem. Phys. Lett.* **454**, 294–298 (2008).

92. Rigby, S. P. & Edler, K. J. The influence of mercury contact angle, surface tension, and retraction mechanism on the interpretation of mercury porosimetry data. *J. Colloid Interface Sci.* **250**, 175–190 (2002).

93. Kim, T., Han, A. & Qiao, Y. Effects of surface-group length on liquid defiltration in a MCM-41. *J. Appl. Phys.* **104**, 034304 (2008).

94. Borman, V. D., Belogorlov, A. A. & Tronin, V. N. Anomalously slow relaxation of interacting liquid nanoclusters confined in a porous medium. *Phys. Rev. E* **93**, 1–11 (2016).

95. Borman, V. D., Belogorlov, A. A. & Tronin, V. N. Observation of relaxation of the metastable state of a non-wetting liquid dispersed in a nanoporous medium. *Colloids Surfaces A Physicochem. Eng. Asp.* **496**, 63–68 (2016).

96. Zhang, Y., Luo, R., Zhou, Q., Chen, X. & Dou, Y. Effect of degassing on the stability and reversibility of glycerol/ZSM-5 zeolite system. *Appl. Sci.* **8**, 1–13 (2018).

97. Sun, Y. T. *et al.* Mechanism of Water Infiltration and Defiltration through ZSM-5 Zeolite: Heating and Sodium Chloride Concentration Effect. *J. Nanomater.* **2013**, 249369 (2013).

98. Borman, V. D., Belogorlov, A. A., Byrkin, V. A., Tronin, V. N. & Troyan, V. I. Observation of a dispersion transition and the stability of a liquid in a nanoporous medium. *JETP Lett.* **95**, 511–514 (2012).

99. Borman, V. D., Belogorlov, A. A., Byrkin, V. A., Tronin, V. N. & Troyan, V. I. Dispersion transition and the nonergodicity of the disordered nanoporous medium-nonwetting liquid system. *J. Exp. Theor. Phys.* **117**, 1139–1163 (2013).

100. Borman, V. D., Belogorlov, A. A., Grekhov, A. M. & Tronin, V. N. Fluctuations of the number of neighboring pores and appearance of multiple nonergodic states of a nonwetting liquid confined in a disordered nanoporous medium. *Phys. Lett. A* **378**, 2888–2893 (2014).

101. Borman, V. D., Belogorlov, A. A., Zhuromskii, V. M. & Tronin, V. N. Anomalously slow relaxation of a nonwetting liquid in the disordered confinement of a nanoporous medium. *J. Exp. Theor. Phys.* **121**, 1027–1041 (2015).

102. Borman, V. D., Tronin, V. N. & Byrkin, V. A. Anomalously slow relaxation of the system of liquid clusters in a disordered nanoporous medium according to the self-organized criticality scenario. *Phys. Lett. A* **380**, 1615–1620 (2016).

103. Rouquerol, J. *et al.* The characterization of macroporous solids: An overview of the methodology. *Microporous Mesoporous Mater.* **154**, 2–6 (2012).

104. Andersson, L., Larsson, P. T., Wågberg, L. & Bergström, L. Evaluating pore space in macroporous ceramics with water-based porosimetry. *J. Am. Ceram. Soc.* **96**, 1916–1922 (2013).

105. Qiao, Y., Liu, L. & Chen, X. Pressurized liquid in nanopores: A modified Laplace-Young equation. *Nano Lett.* **9**, 984–988 (2009).

106. Han, A., Chen, X. & Qiao, Y. Effects of the addition of electrolyte on liquid infiltration in a hydrophobic nanoporous silica gel. *Langmuir* **24**, 7044–7047 (2008).

107. Han, A., Kong, X. & Qiao, Y. Pressure induced liquid infiltration in nanopores. *J. Appl. Phys.* **100**, 014308 (2006).

108. Qiao, Y., Cao, G. & Chen, X. Effects of gas molecules on nanofluidic behehaviors. *J. Am. Chem. Soc.* 2355 (2007).

109. Sun, Y., Li, P., Qiao, Y. & Li, Y. Time-dependent gas-liquid interaction in molecular-sized nanopores. *Sci. Rep.* **4**, 6547 (2014).

110. Duan, Z. & Sun, R. An improved model calculating CO_2 solubility in pure water and aqueous NaCl solutions from 273 to 533 K and from 0 to 2000 bar. *Chem. Geol.* **193**, 257–271 (2003).

111. Shi, X. & Mao, S. An improved model for CO2 solubility in aqueous electrolyte solution containing Na+, K+, Mg2+, Ca2+, Cl- and SO42- under conditions of CO2 capture and sequestration. *Chem. Geol.* **463**, 12–28 (2017).

112. Kong, X. & Qiao, Y. Thermal effects on pressure-induced infiltration of a nanoporous system. *Philos. Mag. Lett.* **85**, 331–337 (2005).

113. Zhang, Y. *et al.* Experimental study on thermal effect on infiltration mechanisms of glycerol into ZSM-5 zeolite under cyclic loadings. *J. Phys. D. Appl. Phys.* **49**, 025303 (2016).

114. Grosu, Y., Ievtushenko, O., Eroshenko, V., Nedelec, J. M. & Grolier, J. P. E. Water intrusion/extrusion in hydrophobized mesoporous silica gel in a wide temperature range: Capillarity, bubble nucleation and line tension effects. *Colloids Surfaces A Physicochem. Eng. Asp.* **441**, 549–555 (2014).

115. Rallabandi, P. S. & Ford, D. M. Permeation of small molecules through polymers confined in mesoporous media. *J. Memb. Sci.* **171**, 239–252 (2000).

116. Bhattacharyya, D. & Butterfield, A. D. A. *New insights into membrane science and technology: polymeric and biofunctional membranes*. (Elsevier, 2003).

117. Bazhenov, S. D. & Lyubimova, E. S. Gas–liquid membrane contactors for carbon dioxide capture from gaseous streams. *Pet. Chem.* **56**, 889–914 (2016).

118. Guo, Y., Langley, K. H. & Karasz, F. E. Nonanomalous diffusion in Vycor porous glass. *Phys. Rev. B* **50**, 3400 (1994).

119. Dupont, J., Fonseca, G. S., Umpierre, A. P., Fichtner, P. F. P. & Teixeira, S. R. Transition-metal nanoparticles in imidazolium ionic liquids: recycable catalysts for biphasic hydrogenation reactions. *J. Am. Chem. Soc.* **124**, 4228–4229 (2002).

120. Wuhrer, M., Koeleman, C. A. M., Hokke, C. H. & Deelder, A. M. Protein glycosylation analyzed by normal-phase nano-liquid chromatography- mass spectrometry of glycopeptides. *Anal. Chem.* **77**, 886–894 (2005).

121. Hu, D., Jiang, H., Meng, K., Xu, J. & Lu, W. The impact mitigation of a heterojunction nanotube--water system: behavior and mechanism. *Phys. Chem. Chem. Phys.* **18**, 7395–7403 (2016).

122. Group, T. F. Surface Tension of Aqueous Solutions of Electrolytes: Relationship with Ion Hydration, Oxygen Solubility, and Bubble Coalescence. **563**, 550–563 (1996).

123. Boström, M., Williams, D. R. M. & Ninham, B. W. Surface tension of electrolytes: Specific ion effects explained by dispersion forces. *Langmuir* **17**, 4475–4478 (2001).

124. Hubbard, A. T. *Encyclopedia of surface and colloid science*. **1**, (CRC press, 2002).

125. Tuckermann, R. Surface tension of aqueous solutions of water-soluble organic and inorganic compounds. *Atmos. Environ.* **41**, 6265–6275 (2007).

126. Xu, B., Qiao, Y., Zhou, Q. & Chen, X. Effect of electric field on liquid infiltration into hydrophobic nanopores. *Langmuir* **27**, 6349–6357 (2011).

127. Han, A., Lu, W., Kim, T., Chen, X. & Qiao, Y. Influence of anions on liquid infiltration and defiltration in a zeolite y. *Phys. Rev. E - Stat. Nonlinear, Soft Matter Phys.* **78**, 3–6 (2008).

128. Kim, T. *et al.* Effects of anion concentration on ion-transport pressure in nanopores. *Appl. Phys. Lett.* **94**, 4–6 (2009).

129. Long, F. A. & McDevit, W. F. Activity coefficients of nonelectrolyte solutes in aqueous salt solutions. *Chem. Rev.* **51**, 119–169 (1952).

130. Ruetschi, P. & Amlie, R. F. Solubility of hydrogen in potassium hydroxide and sulfuric acid. Salting-out and hydration. *J. Phys. Chem.* **70**, 718–723 (1966).

131. Hermann, C. The estimation of gas solubilities in salt solutions. *Chem. Eng. Sci.* **50**, 1673–1675 (1995).

132. Hu, Y., Huang, L., Zhao, S., Liu, H. & Gubbins, K. E. Effect of confinement in nano-porous materials on the solubility of a supercritical gas. *Mol. Phys.* **114**, 3294–3306 (2016).

133. Heiranian, M., Farimani, A. B. & Aluru, N. R. Water desalination with a single-layer MoS 2 nanopore. *Nat. Commun.* **6**, 8616 (2015).

134. Jackson, E. A. & Hillmyer, M. A. Nanoporous membranes derived from block copolymers: From drug delivery to water filtration. *ACS Nano* **4**, 3548–3553 (2010).

135. Sun, C. Y. *et al.* Chiral nanoporous metal-organic frameworks with high porosity as materials for drug delivery. *Adv. Mater.* **23**, 5629–5632 (2011).

136. Gultepe, E., Nagesha, D., Sridhar, S. & Amiji, M. Nanoporous inorganic membranes or coatings for sustained drug delivery in implantable devices. *Advanced Drug Delivery Reviews* **62**, 305–315 (2010).

137. Asao, N. *et al.* Nanostructured materials as catalysts: Nanoporous-gold-catalyzed oxidation of organosilanes with water. *Angew. Chemie - Int. Ed.* **49**, 10093–10095 (2010).

138. Ding, Y. & Chen, M. Nanoporous metals for catalytic and optical applications. *MRS Bull.* **34**, 569–576 (2009).

139. Vlassiouk, I., Takmakov, P. & Smirnov, S. Sensing DNA hybridization via ionic conductance through a nanoporous electrode. *Langmuir* **21**, 4776–4778 (2005).

140. Santos, A., Kumeria, T. & Losic, D. Nanoporous anodic aluminum oxide for chemical sensing and biosensors. *TrAC - Trends in Analytical Chemistry* **44**, 25–38 (2013).

141. Grosu, Y. *et al.* Mechanical, Thermal, and Electrical Energy Storage in a Single Working Body: Electrification and Thermal Effects upon Pressure-Induced Water Intrusion-Extrusion in Nanoporous Solids. *ACS Appl. Mater. Interfaces* **9**, 7044–7049 (2017).

142. Xu, L., Li, M. & Lu, W. Effect of Electrolytes on Gas Oversolubility and Liquid Outflow from Hydrophobic Nanochannels. *Langmuir* (2019). doi:10.1021/acs.langmuir.9b02867

143. Grosu, Y., Faik, A., Nedelec, J. M. & Grolier, J. P. Reversible Wetting in Nanopores for Thermal Expansivity Control: From Extreme Dilatation to Unprecedented Negative Thermal Expansion. *J. Phys. Chem. C* **121**, 11499–11507 (2017).

144. Han, A. & Qiao, Y. A volume-memory liquid. *Appl. Phys. Lett.* **91**, 89–92 (2007).

145. Han, M. & Espinosa-Marzal, R. M. Influence of Water on Structure, Dynamics, and Electrostatics of Hydrophilic and Hydrophobic Ionic Liquids in Charged and Hydrophilic Confinement between Mica Surfaces. *ACS Appl. Mater. Interfaces* **11**, 33465–33477 (2019).

146. Ryzhikov, A., Khay, I., Nouali, H., Daou, T. J. & Patarin, J. Drastic change of the intrusion-extrusion behavior of electrolyte solutions in pure silica *BEA-type zeolite. *Phys. Chem. Chem. Phys.* **16**, 17893–17899 (2014).

147. Li, M., Xu, L. & Lu, W. Nanopore Size Effect on Critical Infiltration Depth of Liquid Nanofoam as A Reusable Energy Absorber.

148. Battino, R., Rettich, T. R. & Tominaga, T. The Solubility of Nitrogen and Air in Liquids. *J. Phys. Chem. Ref. Data* **13**, 563–600 (1984).

149. Jaynes, D. B. & Rogowski, A. S. Applicability of Fick's Law to gas diffusion. *Soil Sci. Soc. Am. J.* **47**, 425–430 (1983).

150. Giacomello, A., Chinappi, M., Meloni, S. & Casciola, C. M. Geometry as a catalyst: How vapor cavities nucleate from defects. *Langmuir* **29**, 14873–14884 (2013).

151. Giacomello, A., Chinappi, M., Meloni, S. & Casciola, C. M. Metastable wetting on superhydrophobic surfaces: Continuum and atomistic views of the cassie-baxter-wenzel transition. *Phys. Rev. Lett.* **109**, 226102 (2012).

152. Enríquez, O. R. *et al.* Growing bubbles in a slightly supersaturated liquid solution. *Rev. Sci. Instrum.* **84**, 065111 (2013).

153. Hemmingsen, E. A. Cavitation in gas-supersaturated solutions. *J. Appl. Phys.* **46**, 213–218 (1975).

154. Mori, Y., Hijikata, K. & Nagatani, T. Effect of dissolved gas on bubble nucleation. *Int. J. Heat Mass Transf.* **19**, 1153–1159 (1976).

155. Phillips, R. K., Friess, B. R., Hicks, A. D., Bellerive, J. & Hoorfar, M. Ex-situ measurement of properties of gas diffusion layers of PEM fuel cells. *Energy Procedia* **29**, 486–495 (2012).

156. Nesbitt, N. T. *et al.* Liquid-Solid Boundaries Dominate Activity of CO2Reduction on Gas-Diffusion Electrodes. *ACS Catal.* 14093–14106 (2020). doi:10.1021/acscatal.0c03319

157. Gadikota, G., Dazas, B., Rother, G., Cheshire, M. C. & Bourg, I. C. Hydrophobic Solvation of Gases (CO2, CH4, H2, Noble Gases) in Clay Interlayer Nanopores. *J. Phys. Chem. C* **121**, 26539–26550 (2017).

158. Ovcharova, A. *et al.* Polysulfone porous hollow fiber membranes for ethylene-ethane separation in gas-liquid membrane contactor. *Sep. Purif. Technol.* **183**, 162–172 (2017).

159. Soubeyrand-Lenoir, E. *et al.* How water fosters a remarkable 5-fold increase in low-pressure CO 2 uptake within mesoporous MIL-100(Fe). *J. Am. Chem. Soc.* **134**, 10174–10181 (2012).

160. Li, M., Barbat, S., Baccouche, R., Belwafa, J. & Lu, W. Enhanced energy mitigation of thin-walled tube filled with liquid nanofoam under dynamic impact. *Compos. Part B Eng.* **193**, 108047 (2020).

161. Li, M., Xu, L. & Lu, W. Effect of Extra Gas Amount on Liquid Outflow from Hydrophobic Nanochannels: Enhanced Liquid-Gas Interaction and Bubble Nucleation. *Langmuir* **36**, 4682–4688 (2020).

162. Michalis, V. K., Moultos, O. A., Tsimpanogiannis, I. N. & Economou, I. G. Molecular dynamics simulations of the diffusion coefficients of light n-alkanes in water over a wide range of temperature and pressure. *Fluid Phase Equilib.* **407**, 236–242 (2015).

163. Abdel-Salam, A. & Chrysikopoulos, C. V. Analysis of a model for contaminant transport in fractured media in the presence of colloids. *J. Hydrol.* **165**, 261–281 (1995).